Journal of Nanomaterials

Self-Assembly of Semiconductor Metal Oxide Nanostructures

Guest Editors: Xiang Wu, Xijin Xu, Haibo Zeng, and Chuanfei Guo

Self-Assembly of Semiconductor Metal Oxide Nanostructures

Journal of Nanomaterials

Self-Assembly of Semiconductor Metal Oxide Nanostructures

Guest Editors: Xiang Wu, Xijin Xu, Haibo Zeng, and Chuanfei Guo

Editorial Board

Contents

Hindawi Publishing Corporation
Journal of Nanomaterials
Volume 2013, Article ID 459516, 2 pages
http://dx.doi.org/10.1155/2013/459516

Editorial

Self-Assembly of Semiconductor Metal Oxide Nanostructures

Xiang Wu,[1] Xijin Xu,[2] Haibo Zeng,[3] and Chuanfei Guo[4]

[1] *Key Laboratory for Photonic and Electronic Bandgap Materials, Ministry of Education and College of Chemistry and Chemical Engineering, Harbin Normal University, Harbin 150025, China*
[2] *School of Physics and Technology, University of Jinan, Shandong, Jinan 250022, China*
[3] *School of Materials Science and Engineering, Nanjing University of Science and Technology, Nanjing 210094, China*
[4] *Department of Physics, Boston College, Chestnut Hill, MA 02467, USA*

Correspondence should be addressed to Xiang Wu; wuxiang05@gmail.com

Received 12 June 2013; Accepted 12 June 2013

In recent years, one-dimensional (1D) semiconductor metal oxide nanostructures, such as nanowires, nanorods, and nanotubes, have been the intensive research focus for their potential applications in optical, electrical, optoelectronic, photocatalytic, and hydrophilic/hydrophobic fields. To improve the output efficiency of the nanodevices in various fields, assembling nanostructured building blocks into two-dimensional (2D) or three-dimensional (3D) hierarchical structures is prerequisite.

As guest editors, we are pleased to organize a special issue with a variety of topics within self-assembly of 1D semiconductor nanostructures, as well as the combination of synthesis and application aspects. This is the first special issue on self-assembly of 1D semiconductor nanostructures that brings together papers concerning recent developments in synthesis and self-assembly of nanocrystals. This special issue consists of a collection of two review articles, seven articles that are contributed from Japan, China, and Israel's scientists.

The review article by H. Zeng's group overviews the fabrication methods of ZnO-based transparent conductive thin films and emphasizes optimum processing parameter conditions and growth mechanism of the as-obtained film on flexible substrate. The review by C. Lai summarizes the synthesis and properties of one-dimensional TiO_2 nanomaterials (bare 1D TiO_2 nanomaterial and 1D hierarchical TiO_2) and their photovoltaic performance in dye-sensitized solar cells (DSSCs).

The article by H. Zhang et al. studies the effect of alumina dopant on transparency of tetragonal zirconia, and they found that low transparency of the resultant yttria stabilized tetragonal zirconia doped with alumina specimens does not suggest a beneficial effect of alumina dopant even when nanometric grains and high density have been achieved. Finally, they also proposed a possible formation mechanism. X. Wu and coworkers synthesize hierarchical ZnO nanostructures assembled from nanosheets through a facile hydrothermal route. Their results show that sulfur powder plays a critical role in the morphology of the products. Room temperature photoluminescence property of the hierarchical ZnO nanostructures shows an ultraviolet emission peak at 385 nm. Scientists from that the Hebrew University demonstrate two alternatives for self-assembled patterning within the nanoscale resolution of optically active semiconductor nanocrystals. The first is substrate selective and uses high-resolution surface patterning to achieve localized self-assembly. The 2nd method uses surface with poly(methyl methacrylate)-(PMMA-) resistant patterning adsorption of the nanocrystal with covalent bonds and lift-off. Wang's group reports synthesis of silica-coated TiO_2 nanotubes. They discuss the effects of gas-supported process on tubular morphology, crystallinity, and photocatalytic activity. It is found that the sample prepared at hydrothermal treatment and calcination shows perfect open-ended tubular morphology and increased crystallinity. And the photoactivity of the as-product is proved to be 5 times higher than that of TiO_2

nanoparticles. X. Wu's group showed large-scale synthesis of ZnS nanobelts by simply thermal evaporation of ZnS powder in the presence of Au catalysts at 1020°C. Room-temperature photoluminescence measurements showed that the as-synthesized ZnS nanostructures had a strong green emission bands at a wavelength of 427 nm; they attributed it to deep-level emissions induced by defects or impurities. Gao et al. synthesize mesostructured ZnO with excellent methanol sensing properties by a structure replication procedure through the incipient wetness technique. Their experimental results show that mesostructured ZnO material shows the higher sensitivity and stability in comparison with the non-porous ZnO prepared through conventional coprecipitation approach. Finally, X. Wu et al. report formation of flowerlike Ag_2O/ZnO heterostructure hybrids by a simple two-step procedure without any surfactants. The as-prepared heterostructure composite showed Ag_2O nanoparticles coated uniformly on the surface of ZnO microflowers. They propose a possible growth mechanism of the products based on the experimental results. PL measurements of the as-obtained product reveal a strong UV band-edge emission peak at 383 nm.

Acknowledgments

The guest editors would like to thank all of the above authors who contributed articles to this special issue for Journal of Nanomaterials. We feel that these contributions provide a cross-section to the current development and future research focuses of self-assembly of 1D semiconductor nanostructure. We also hope that this collection of articles will inspire researchers and stimulate new ideas in relative research field.

Xiang Wu
Xijin Xu
Haibo Zeng
Chuanfei Guo

Hindawi Publishing Corporation
Journal of Nanomaterials
Volume 2013, Article ID 762730, 11 pages
http://dx.doi.org/10.1155/2013/762730

Review Article

One-Dimensional TiO_2 Nanostructures as Photoanodes for Dye-Sensitized Solar Cells

Jie Qu[1] and Chao Lai[2]

[1] *Center for Low-Dimensional Materials, Micro-Nano Devices and System and Jiangsu Key Laboratory for Solar Cell Materials and Technology, Changzhou University, Changzhou 213164, China*
[2] *School of Chemistry and Chemical Engineering, Jiangsu Normal University, Xuzhou, Jiangsu 221116, China*

Correspondence should be addressed to Chao Lai; laichao@jsnu.edu.cn

Received 22 December 2012; Accepted 2 February 2013

Academic Editor: Xijin Xu

Titanium dioxide (TiO_2) is star materials due to its remarkable optical and electronic properties, resulting in various applications, especially in the fields of dye-sensitized solar cells (DSSCs). Photoanode is the most important part of the DSSCs, which help to adsorb dye molecules and transport the injected electrons. The size, structure, and morphology of TiO_2 photoanode have been found to show significant influence on the photovoltaic performance of DSSCs. In this paper, we briefly summarize the synthesis and properties of one-dimensional (1D) TiO_2 nanomaterials (bare 1D TiO_2 nanomaterial and 1D hierarchical TiO_2) and their photovoltaic performance in DSSCs.

1. Introduction

Titanium dioxide (TiO_2) is one of the most extensively studied oxides because of its remarkable optical and electronic properties. Due to its unique physical and chemical properties, TiO_2 has been extensively used for various applications, such as dye-sensitized solar cells (DSSCs), lithium ion batteries (LIBs), photocatalysis, water treatment, and gas sensors [1–21].

A typical DSSC consists of a dye-sensitized semiconductor electrode, redox electrolyte, and counter electrode [23, 24]. Once dye molecules absorb light, the excited dye injects electrons to the semiconductor. At the same time, the oxidized dye cation is reduced by the redox electrolyte, which competes with the recombination of injected electrons. Electrons are collected at the semiconductor electrode, pass through the external circuit, and then reenter the cell at the counter electrode to reduce the oxidized electrolyte [25]. A closed circuit is thereby established to continuously convert the solar light to electricity. Nanostructure-based DSSCs show advantages of low cost, high efficiency, and simple in preparation, which is promising as a renewable energy resource for sustainable development of the future [2, 23, 26, 27]. A breakthrough in DSSCs was achieved in 1991, O'Regan and Grätzel firstly introduced wide bandgap semiconductor nanocrystal (TiO_2 nanoparticle) into DSSCs as the transporting medium of photo-induced electrons, and conversion efficiency was reached to 7% [2]. Recently the efficiency of DSSCs has been increased to 12.3% [28].

Dye-sensitized semiconductor electrode is usually the efficiency determining component of DSSCs due to the competition between electron separation and recombination accompanying with many electron transfer processes [5, 29, 30]. In brief, semiconductor oxides receive the injected electrons from the excited state of sensitizer dye, and the electrons could be competitively trapped by oxidized dye cation, I_3^- anion in electrolyte, and surface state in TiO_2 (e.g., oxygen vacancy) that is known as recombination, before they are transported to an external circuit. The described electron transfer processes in the semiconductor electrode affect essentially conversion efficiency of DSSCs, which depends on the nature and morphology of nanocrystalline semiconductor oxides [31–34].

Wide bandgap semiconductor nanoparticles were the first material used as an efficient photoanode. Due to the small size of the nanoparticles, it can provide a large surface area and a relatively high porosity [2], possible to adsorb enough dye for efficient light harvesting and a relative high

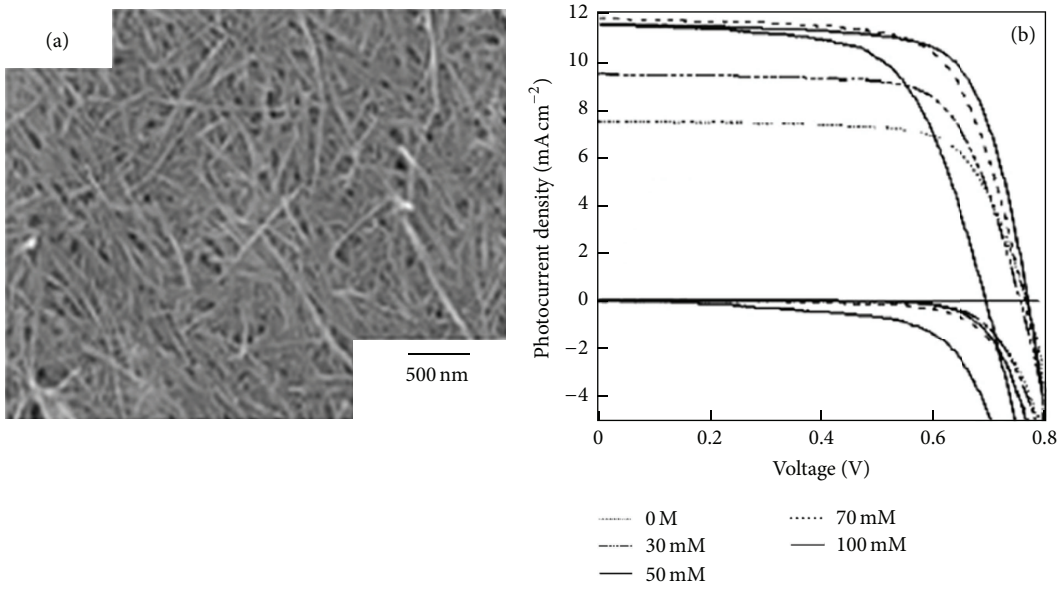

Figure 1: (a) SEM images of mesoporous electrodes sintered at 500°C made of TNTs paste B. (b) Photocurrent-voltage curves obtained from the cells with TNTs electrodes at various Li^+ concentrations [22].

conversion efficiency. However, TiO_2 nanoparticles used in DSSCs are usually as a random network of crystallographically misaligned crystallites, and lattice mismatches at the grain boundaries could influence electron scattering and act as electron trap [31, 34, 35]. This could limit electron transport and reduce electron lifetime. Further improvement of DSSC-based nanoparticle is hindered by the previous drawbacks. One-dimensional TiO_2 nanostructures [36–48] have a relatively small amount of grain boundaries and can act as single crystal, which is able to reduce the grain boundary effect and provide fast electron transport. It shows great potential in achieving high performance DSSCs. The recombination rate in TiO_2 nanotubes has been found to be 10 times slower than that in nanoparticles [37]. However, it is more difficult for the liquid electrolyte to penetrate into one-dimensional titania than into nanoparticles network, because the one-dimensional titania has usually relatively low surface area, large size, and inefficient intact surface compared with nanoparticles. This usually leads to a large interface charge-transfer resistance for one-dimensional nanostructured materials-based photoanode.

To resolve the drawbacks of the nanoparticles and 1D nanostructures, 1D hierarchically structured materials were designed by combining nanoparticles and nanorods or nanowires. They have been used to take advantage of both the large surface area of nanoparticles and efficient charge transport of 1D nanostructures [50]. The interpenetration of electrolyte in the 1D hierarchical structure could be improved, and the interfacial area could be increased which might leads to more electron separation and fast transport [31, 34, 35, 51–57]. Compared with the nanoparticles and 1D nanostructures, the photovoltaic properties of 1D hierarchical structure are superior. This indicate a potential approach to overcome the limitations of nanoparticles and one-dimensional nanostructures as photoanode materials, though the increase of the grain boundary effect is inevitable in a hybrid structure matrix due to the formation of grain boundaries between nanoparticles and nanorods or nanowires.

In this paper, we review the recent developments in using of one-dimensional (1D) nanostructures as photoanodes for efficient DSSCs. Various randomly oriented and vertically aligned 1D nanostructures, and their composites with nanoparticles used in DSSCs are discussed, for which the order is randomly oriented 1D nanotubes and nanorods, vertically aligned 1D nanotubes and nanorods, randomly oriented 1D hierarchical TiO_2 and vertically aligned 1D hierarchical TiO_2.

2. Applications in DSSC Photoanode

The photoanode shows significant effects on the photocurrent and photovoltage of a DSSC. As a key material in photoanode, fast electron transfer kinetics of TiO_2 are necessary to avoid photoelectron recombination, which usually depends strongly on the micromorphology and crystallographic structure of TiO_2. Therefore, it is very important to synthesize controllably titania nanomaterials with specific structures and big surface area with optimized electron transfer kinetics.

2.1. Randomly Oriented 1D TiO_2

2.1.1. Randomly Oriented 1D TiO_2 Nanotube. To overcome the electron transport limit of nanoparticles, TiO_2 nanotubes were the first reported 1D nanomaterial for use as a bifunctional photoanode material, which exhibiting both efficient generation of photon-generated electrons and good light-scattering property. Uchida et al. [58] have developed a facile one-step hydrothermal method to synthesize TiO_2 nanotube [59]. The nanotube is 100 nm long with an outer diameter of

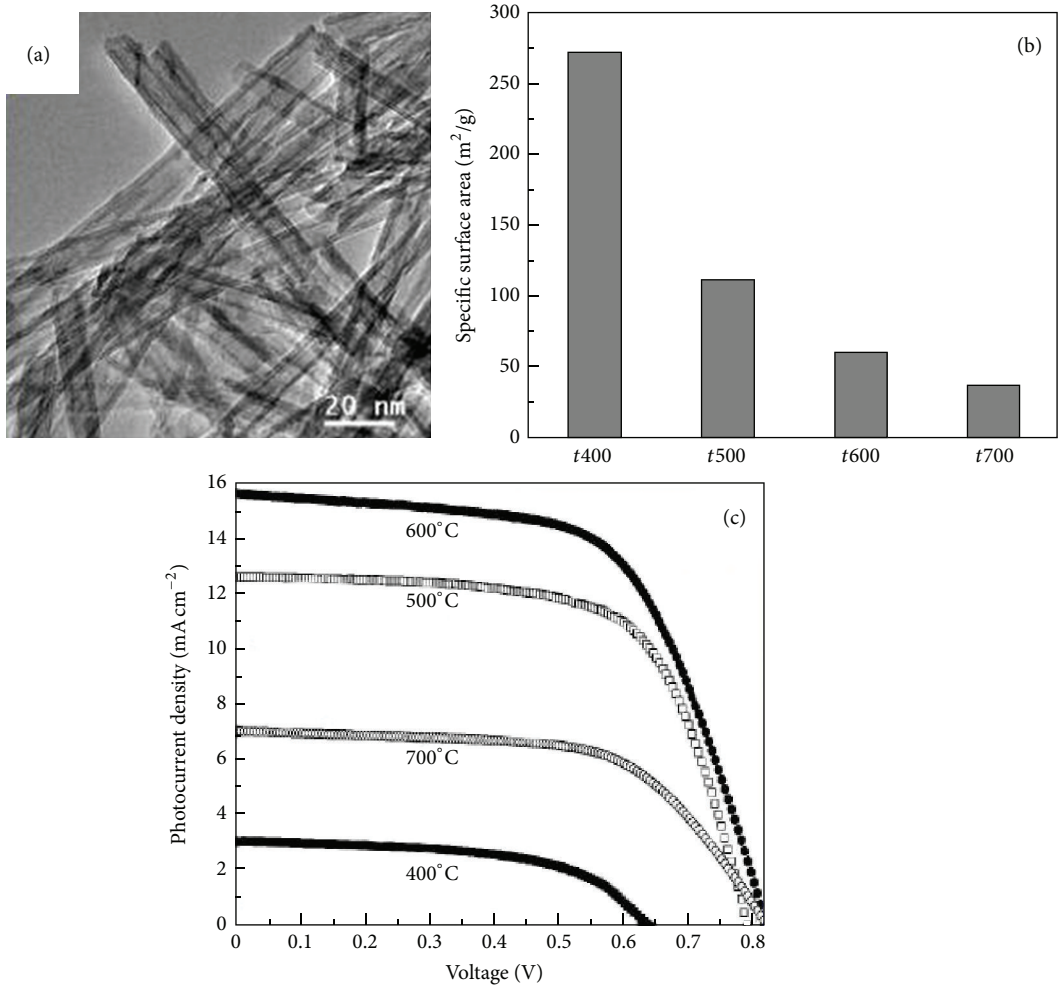

Figure 2: (a) TEM micrographs of titanate nanotubes calcined at 400°C. (b) Specific surface area of samples calcined at different temperatures. (c) *I-V* curves for titanate nanotubes calcined at different temperatures. Illumination intensity of 100 mW cm^{-2} with global AM 1.5 and an active area of 0.25 cm^2 were applied [16].

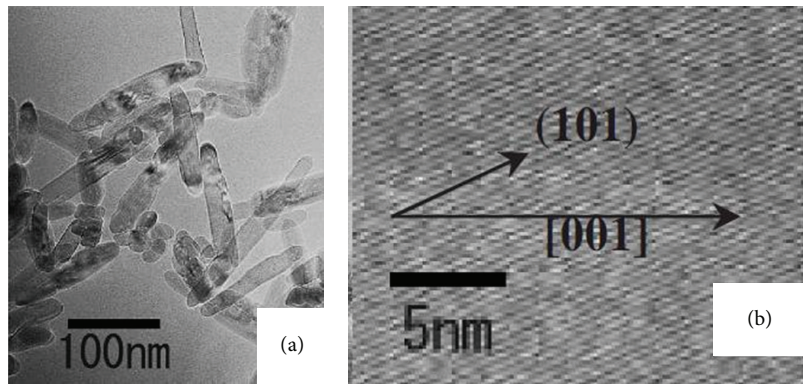

Figure 3: (a) TEM image of nanorods prepared with F127. (b) HRTEM image of (a) [49].

8 nm. The specific surface area can reach to 270 m^2/g. DSSC with such nanotube showed a 2.9% conversion efficiency, which was not better than that of nanoparticles. The main reason for the previous result may due to the aggregate of the TiO_2 nanotube, which could reduce electricity contact and increase impedance between TiO_2 nanotube and conductive glass. And the nanotube wall here could also block the diffusion of the I^-/I_3^-.

To synthesize TiO_2 nanotube with high dispersion and crystallization could improve the photoelectrochemical

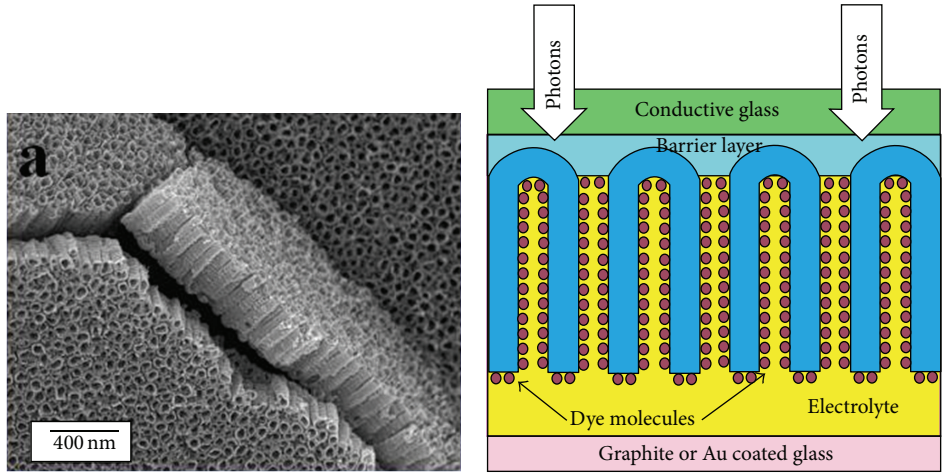

(a) (b)

Figure 4: (a) Lateral view FESEM images of titanium nanotubes grown from a 500 nm thick Ti thin film (sputtered onto SnO_2:F coated glass at 500°C) anodized using a 0.5% HF electrolyte concentration at a potential of 12 V. (b) Integration of transparent nanotube array architecture into dye solar cell structure [38].

Table 1: Detailed IMPS/IMVS parameters of the DSSC with titanate nanotubes calcined at different temperatures [16].

Calcination temperature	τ_d (ms)[a]	τ_n (ms)[a]	D_n (cm^2/s)[a]	L_n (μm)[a]
400°C	1.83	14.2	3.5×10^{-4}	22.3
500°C	1.18	53	5.4×10^{-4}	53.6
600°C	0.94	106	6.8×10^{-4}	85
700°C	1.47	17.7	4.4×10^{-4}	27.8

properties. Adachi et al. [60] and Ohsaki et al. [22] have reported such TiO_2 nanotubes (TNTs) with large aspect ratio and large specific surface area. The conversion efficiency could reach to 6.4% (Figure 1). After treating with the $TiCl_4$, the conversion efficiency could increase to 7.1%. Single crystal of TiO_2 facilitates the fast transport of electron. And large aspect ratio of TiO_2 nanotubes could help to reduce the grain boundary effect. The research also indicated that the increased electron density and electron lifetime in the photoanode could be beneficial for the improved photoelectrochemical properties.

Our group [16] also reported the protonated TiO_2 nanotube prepared from one-step hydrothermal method with anatase TiO_2 and 10 M NaOH solution as the starting materials [15, 61]. After being calcined at 400°C, single crystal of TiO_2(B) nanotube was obtained (Figure 2). Although nanotubes have the advantage in morphology and surface area for enhancing photoelectrochemical performance, TiO_2(B) nanotubes in this work showed relatively poor photovoltaic properties with the η value of only 1.05%. The poor performance here was mainly related to the serious recombination in numerous surface defects and a relatively open tunnel structure of TiO_2(B) [15]. Higher temperature calcination would reduce the surface defects, but the tube morphology could not exist.

2.1.2. Randomly Oriented 1D TiO_2 Nanorod. One-dimensional TiO_2 nanorods have a relatively small amount of grain boundaries and can act as single crystal, which is able to reduce the grain boundary effect and provide fast electron transport [51–53]. And the rod could keep the rod morphology with higher temperature calcination. Many researches were focused on TiO_2 nanorods.

Jiu et al. [49, 62] have reported single crystalline anatase TiO_2 nanorods synthesized by surfactant-assisted hydrothermal method. Short rods with the diameter 20–30 nm and length 100–150 nm have been obtained (Figure 3). The clear lattice strips indicated that the nanorods with high crystallinity and fewer defects have been obtained, which is beneficial for the transfer of electrons in the rods. A high light-to-electricity conversion yield of 7.06% was achieved by applying the TiO_2 nanorods as thin film of dye-sensitized solar cells. The nanorod shows the same advantages as nanotubes: the fast electron transport, the reduced recombination, and the long lifetime.

We also fabricated such small size nanorods with a special method different from the tradition. The nanorods were obtained by calcination of protonated TiO_2 nanotube at 600°C for 2 h [16]. It is much thicker and shorter with a diameter of 15–30 nm and a length of about 100 nm. The interference fringe spacing of the nanorods is about 0.35 nm, corresponding to the interplanar distance of the (101) plane in the anatase phase. And the conversion efficiency could reach to 7.71%. IMPS and IMVS were used to investigate further the electron transport and recombination processes, as shown in Table 1. Compared with nanotube calcined at 400°C, nanorods calcined at 600°C show a longer lifetime, which is over 10-fold longer than that for TiO_2(B) nanotube and a shorter electron transport time only half of the TiO_2(B) nanotube. This indicates that anatase nanorods with a good crystallinity are beneficial to a faster electron transport and a longer electron lifetime. In fact, it is considered that the

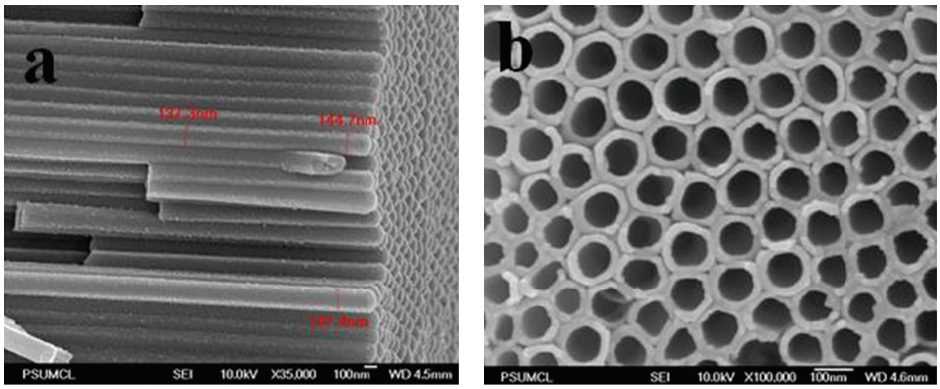

(a) (b)

Figure 5: Illustrative FESEM cross-sectional (a) and top images (b) of a nanotube-array sample grown at 60 V in an ethylene glycol electrolyte containing 0.25 wt% NH_4F [63].

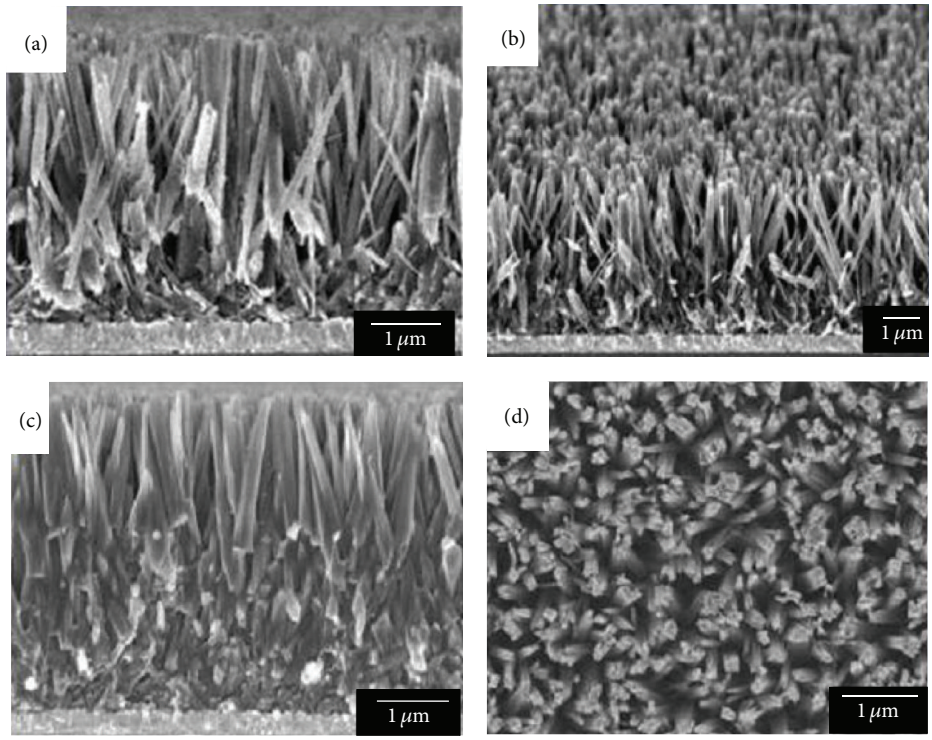

Figure 6: FESEM images of oriented rutile TiO_2 nanorod films grown from a two-step hydrothermal reaction; (a, b) and (c, d) with and without addition of saturated aqueous NaCl solution [44].

good crystallinity and the cylindrical geometry could allow the nanorods to support radial electric fields, which could keep the electrons away from the nanorods surface, thereby reducing surface electron densities and recombination.

2.2. Vertically Aligned 1D TiO_2. Randomly oriented 1D TiO_2 nanomaterial undoubtedly plays as the "electron speedways;" however, these nanotubes and nanorods are disordered and random. It has not realized the direct electron transport. So, it is significant to design and study the vertically aligned 1D TiO_2 nanomaterials would be much more significative.

2.2.1. Vertically Aligned 1D TiO_2 Nanotube. Vertically aligned TiO_2 nanotubes provide a vertical pathway for electron transport along the tube and thus minimize electron loss during diffusion process, and the vertically ordered tubular structure will facilitate the filling of new sensitizer or electrolyte for a further increase in efficiency. As such, self-aligned TiO_2 nanotube arrays have been widely studied for applications as photoanodes in DSSCs [65–74].

Mor et al. [38] have reported a highly ordered 360 nm long TiO_2 nanotube arrays, made by anodization of thick-film titanium foil (Figure 4). Afer treating with $TiCl_4$ and

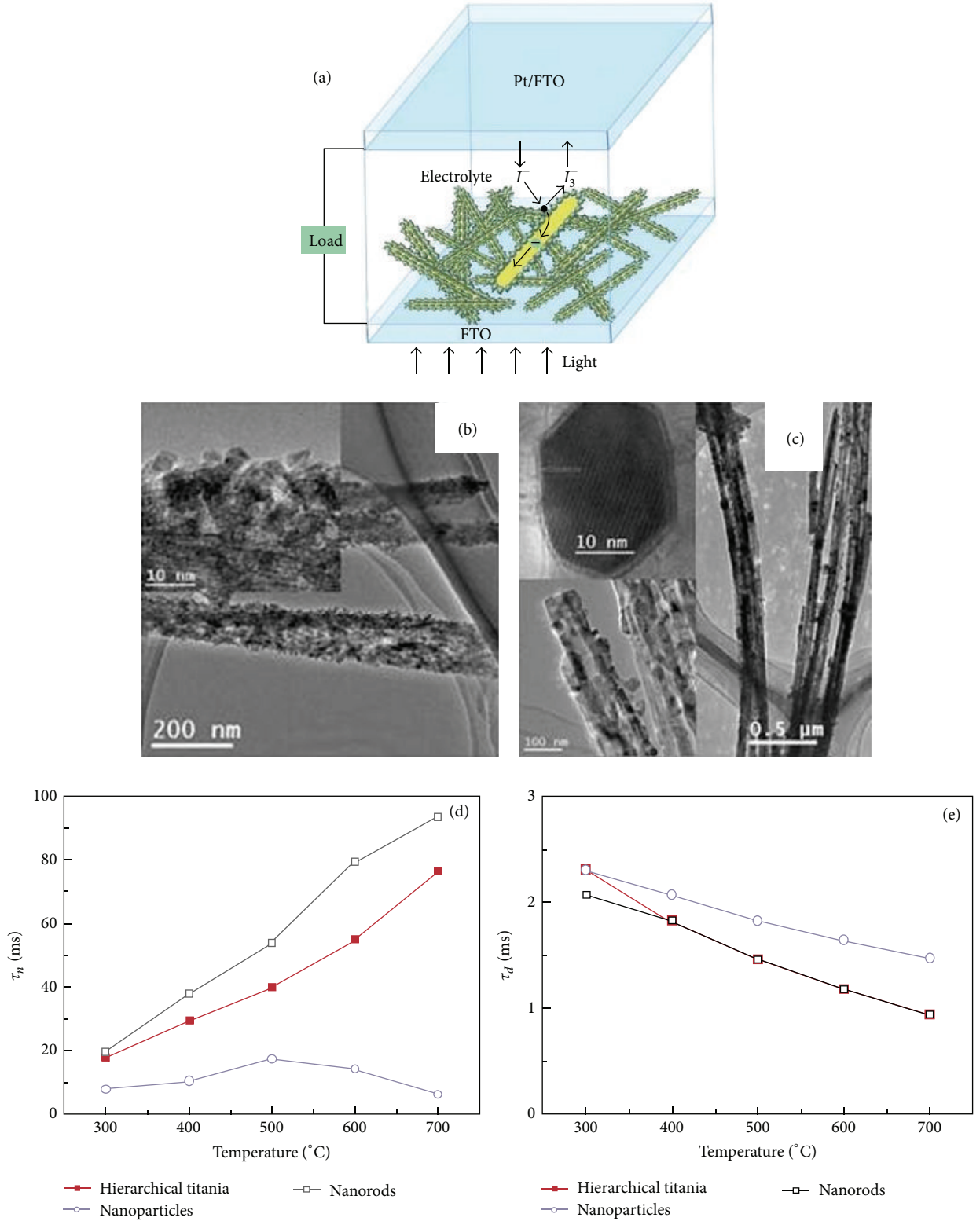

FIGURE 7: (a) Schematic diagram of the dye-sensitized solar cell with the one-dimensional hierarchical titania as photoanode on FTO, showing the processes involved in current generation. (b, c) TEM images of the one-dimensional titania with hierarchical structures after calcination at 300°C (b) and 700°C (c). (d, e) The electron lifetime (τ_n) (d) and electron transport time (τ_d) (e) for DSSCs of titania with hierarchical structures, nanorods, and nanoparticles [50].

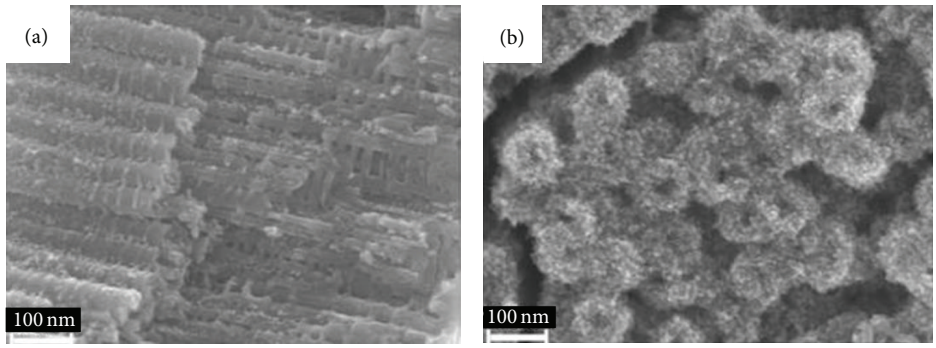

Figure 8: (a) SEM images of one-cycle infiltration: inside view of the split NTs. (b) NT and NP mixed structure after two-cycle infiltration [64].

calcining at 450°C, a highly ordered photoanode was obtained. The DSSC exhibited a J_{sc} of 7.87 mA/cm^2, a V_{oc} of 0.75 V, and an overall conversion efficiency of 2.9%. This result was no better than nanoparticles. A low surface area with a length of only 360 nm could be responsible for the result of insufficient dye-loading and low light-harvesting efficiency. However, highly ordered arrays showed a long lifetime and excellent electron transport path compared to nanoparticles. To resolve the problem of the low surface area, many efforts were done. Nanotubes with lengths up to 100 μm have been produced to increase the surface area for dye-loading [63, 75]. Shankar et al. [63] even obtained ultralong TiO_2 nanotubes with length over 200 μm (Figure 5), which delivered significantly improved DSSC efficiency of 6.89%. However, synthesis of these ultralong nanotubes costs much time (more than 10 h) and electricity for anodization process, and the reported efficiencies of TiO_2-nanotube-array-based DSSCs are still lower than DSSCs based on mesoporous TiO_2 films due to the relative low internal surface area for dyeloading of nanotube arrays [44, 76, 77].

2.2.2. Vertically Aligned 1D TiO_2 Nanorod. Different from 1D nanotube array, DSSCs based on 1D TiO_2 nanorods array remain a challenge [43, 78–86], which is mainly owing to the low dye-loading ability resulting from the insufficient specific surface area. Liu and Aydil [44] reported a facile, hydrothermal method for the first time to grow oriented, single-crystalline rutile TiO_2 nanorod films on transparent conductive fluorine-doped tin oxide (FTO) substrates (Figure 6). The growth parameters, such as growth time, growth temperature, initial reactant concentration, acidity, and types additives, could effectively influence the diameter, length, and density of the nanorods. A small lattice mismatch between the FTO substrate and rutile TiO_2 is key in driving the nucleation and growth of the rutile TiO_2 nanorods on FTO. 4 μm long TiO_2 nanorod films were obtained through the previous method. Afer treating with $TiCl_4$, a light-to-electricity conversion efficiency of 3% was achieved.

Many efforts have done to modify the oriented rutile TiO_2 nanorod to improve the photoelectrochemistry properties. Lv et al. [87] have reported a densely aligned TiO_2 nanorod arrays (NRAs) with high surface area. Theses densely aligned TiO_2 NRAs with tunable thickness were grown directly on transparent conductive fluorine-doped tin oxide (FTO) substrates by hydrothermal method. Dilute hydrochloric acid was used as chemical etching liquid to further increase the specific surface area of the TiO_2 NRAs. TiO_2 nanorods were splited into secondary nanorods with a reduced diameter during the etching treatment. And the inner surface area of the TiO_2 NRAs was markedly enlarged. Finally, a conversion efficiency of 5.94% was achieved by using such NRAs. It is so far the best reported results for the 1D rutile TiO_2 NRA films.

2.3. 1D Hierarchical TiO_2 Nanomaterial. TiO_2 nanoparticles used in DSSCs have its limitations, such as influencing the electron scattering and acting as an electron trap. 1D nanostructured TiO_2 could reduce the grain boundary effect and provide fast electron transport. However, it is more difficult for the liquid electrolyte to penetrate into one-dimensional titania than into nanoparticles network. And the small surface area would block the improving of the photoelectrochemistry properties. In general, fast reaction kinetics (fast electron transport, long electron lifetime, and less recombination) together with large specific surface area are the essential properties of the superior photoanode materials with excellent photoelectrochemical properties.

2.3.1. Randomly Oriented 1D Hierarchical TiO_2. To achieve highly efficient DSSCs, one-dimensional hierarchical composites were designed as show in Figure 7 [50], which combine the high electron transport from 1D nanostructures and large surface area to attach enough dyes from nanoparticles. A proposed electron transfer model is shown in the following; the injected electrons in the nanoparticles standing on nanorods are subject to transfer into the nanorods and then are rapidly transported to FTO substrate due to the single-crystal feature of the nanorods. The results indicate that one-dimensional hierarchical titania cannot only provide a matrix similar to the hybrid structure matrix but also avoid forming a large amount of grain boundaries with optimized fast reaction kinetics: low charge-transfer resistance, fast electron transport, and long electron lifetime. And the existed nanoparticles greatly improve the surface area of the nanorods. The conversion efficiency of one-dimensional

hierarchical titania can reach to 4.46%, which is about 5 times higher than that of their corresponding nanorods.

2.3.2. Vertically Aligned 1D hierarchical TiO_2. Pan et al. [64] have reported vertically aligned 1D hierarchical TiO_2. 10 nm size of TiO_2 NPs were uniformly coated on the side walls of NTs through infiltration with $TiCl_4$ solution and hydrothermal synthesis (Figure 8). Compared with the bare NT structure, dye-loading of mixed NT and NP structure was two times doubled. The larger surface area resulted in more recombination which slightly reduced the electron lifetime. However, the diffusion length was still longer than the tube length used. This means most electrons are collected.

3. Summary

In this paper, we have summarized the using of 1D TiO_2 nanostructures as electrode materials for DSSC photoanode.

Randomly oriented 1D TiO_2 (nanotubes and nanorods) with cylindrical geometry could support radial electric fields that could keep the electrons away from the nanorods surface, thereby reducing surface electron densities and recombination. And large aspect ratio of TiO_2 would help to reduce the grain boundary effect. The electron lifetime would also increase. All these advantages could be beneficial for the improved photoelectrochemical properties. However, randomly oriented 1D TiO_2 nanomaterial are disordered and random. It has not realized the direct electron transport. Vertically aligned TiO_2 nanotubes provide a vertical pathway for electron transport along the tube and thus minimize electron loss during diffusion process, and the vertically ordered tubular structure will facilitate the filling of new sensitizer and electrolyte for a further increase in efficiency. However, the small surface area made the photoelectrochemistry properties worse than the randomly oriented 1D TiO_2 nanomaterial. In general, fast reaction kinetics (fast electron transport, long electron lifetime, and less recombination) together with large specific surface area are the essential properties of the superior photoanode materials with excellent photoelectrochemical properties. To achieve highly efficient DSSCs, 1D hierarchical TiO_2 were designed. Both randomly oriented and vertically aligned 1D nanostructures have been used as the photoanode materials. Detailed study showed that this 1D hierarchical TiO_2 could combine the high electron transport from 1D nanostructures and large surface area to attach enough dyes from nanoparticles. Furthermore, the bigger pores inside the hierarchically structured films are also beneficial for the permeation and diffusion of electrolyte in the photoanode, forming good ohmic contact. The results provide a potential approach to obtain highly effective solar conversion materials.

Acknowledgments

This work has been supported by the Chinese National Science Funds (no. 51202094); the Priority Academic Program Development of Jiangsu Higher Education Institutions; the Natural Science Foundation (no. 12KJB150010 and no. 12KJB430001) of Jiangsu Education Committee of China.

References

[1] A. Fujishima and K. Honda, "Electrochemical photolysis of water at a semiconductor electrode," *Nature*, vol. 238, no. 5358, pp. 37–38, 1972.

[2] B. O'Regan and M. Grätzel, "A low-cost, high-efficiency solar cell based on dye-sensitized colloidal TiO_2 films," *Nature*, vol. 353, pp. 737–740, 1991.

[3] M. R. Hoffmann, S. T. Martin, W. Choi, and D. W. Bahnemann, "Environmental applications of semiconductor photocatalysis," *Chemical Reviews*, vol. 95, no. 1, pp. 69–96, 1995.

[4] R. Wang, K. Hashimoto, A. Fujishima et al., "Light-induced amphiphilic surfaces," *Nature*, vol. 388, no. 6641, pp. 431–432, 1997.

[5] M. Grätzel, "Photoelectrochemical cells," *Nature*, vol. 414, no. 6861, pp. 338–344, 2001.

[6] S. U. M. Khan, M. Al-Shahry, and W. B. Ingler, "Efficient photochemical water splitting by a chemically modified n-TiO_2," *Science*, vol. 297, no. 5590, pp. 2243–2245, 2002.

[7] P. V. Kamat, "Meeting the clean energy demand: nanostructure architectures for solar energy conversion," *Journal of Physical Chemistry C*, vol. 111, no. 7, pp. 2834–2860, 2007.

[8] E. Maciak and Z. Opilski, "Transition metal oxides covered Pd film for optical H_2 gas detection," *Thin Solid Films*, vol. 515, no. 23, pp. 8351–8355, 2007.

[9] M. G. Manera, J. Spadavecchia, D. Buso et al., "Optical gas sensing of TiO_2 and TiO_2/Au nanocomposite thin films," *Sensors and Actuators B*, vol. 132, no. 1, pp. 107–115, 2008.

[10] F. Campus, P. Bonhôte, M. Grätzel, S. Heinen, and L. Walder, "Electrochromic devices based on surface-modified nanocrystalline TiO_2 thin-film electrodes," *Solar Energy Materials and Solar Cells*, vol. 56, no. 3-4, pp. 281–297, 1999.

[11] D. P. Partlow and T. W. O'Keeffe, "Thirty-seven layer optical filter from polymerized sol-gel solutions," *Applied Optics*, vol. 29, no. 10, pp. 1526–1529, 1990.

[12] A. Brudnik, H. Czternastek, K. Zakrzewska, and M. Jachimowski, "Plasma-emission-controlled d.c. magnetron sputtering of TiO_{2-x} thin films," *Thin Solid Films*, vol. 199, no. 1, pp. 45–58, 1991.

[13] L. Yang, S. S. Saavedra, N. R. Armstrong, and J. Hayes, "Fabrication and characterization of low-loss, sol-gel planar waveguides," *Analytical Chemistry*, vol. 66, no. 8, pp. 1254–1263, 1994.

[14] L. Xiao-e, A. N. M. Green, S. A. Haque, A. Mills, and J. R. Durrant, "Light-driven oxygen scavenging by titania/polymer nanocomposite films," *Journal of Photochemistry and Photobiology A*, vol. 162, no. 2-3, pp. 253–259, 2004.

[15] H. Zhang, G. R. Li, L. P. An, T. Y. Yan, X. P. Gao, and H. Y. Zhu, "Electrochemical lithium storage of titanate and titania nanotubes and nanorods," *Journal of Physical Chemistry C*, vol. 111, no. 16, pp. 6143–6148, 2007.

[16] J. Qu, Q. D. Wu, Y. R. Ren, Z. Su, C. Lai, and J. N. Ding, "Enhanced high-rate performance of double-walled TiO_2-B nanotubes as anodes in lithium-ion batteries," *Chemistry*, vol. 7, no. 11, pp. 2516–2518, 2012.

[17] P. G. Bruce, B. Scrosati, and J. M. Tarascon, "Nanomaterials for rechargeable lithium batteries," *Angewandte Chemie—International Edition*, vol. 47, no. 16, pp. 2930–2946, 2008.

[18] A. R. Armstrong, G. Armstrong, J. Canales, and P. G. Bruce, "TiO_2-B nanowires," *Angewandte Chemie*, vol. 116, no. 17, pp. 2336–2338, 2004.

[19] G. Armstrong, A. R. Armstrong, J. Canales, and P. G. Bruce, "Nanotubes with the TiO_2-B structure," *Chemical Communications*, no. 19, pp. 2454–2456, 2005.

[20] C. Lai, H. Z. Zhang, G. R. Li, and X. P. Gao, "Mesoporous polyaniline/TiO_2 microspheres with core-shell structure as anode materials for lithium ion battery," *Journal of Power Sources*, vol. 196, no. 10, pp. 4735–4740, 2011.

[21] C. Lai, G. R. Li, Y. Y. Dou, and X. P. Gao, "Mesoporous polyaniline or polypyrrole/anatase TiO_2 nanocomposite as anode materials for lithium-ion batteries," *Electrochimica Acta*, vol. 55, no. 15, pp. 4567–4572, 2010.

[22] Y. Ohsaki, N. Masaki, S. Yanagida et al., "Dye-sensitized TiO_2 nanotube solar cells: fabrication and electronic characterization," *Physical Chemistry Chemical Physics*, vol. 7, no. 24, pp. 4157–4163, 2005.

[23] A. Hagfeldt and M. Grätzel, "Molecular photovoltaics," *Accounts of Chemistry Research*, vol. 3, pp. 269–277, 2000.

[24] J. Bisquert, D. Cahen, G. Hodes, S. Rühle, and A. Zaban, "Physical chemical principles of photovoltaic conversion with nanoparticulate, mesoporous dye-sensitized solar cells," *Journal of Physical Chemistry B*, vol. 108, no. 24, pp. 8106–8118, 2004.

[25] Y. Tachibana, J. E. Moser, M. Grätzel, D. R. Klug, and J. R. Durrant, "Subpicosecond interfacial charge separation in dye-sensitized nanocrystalline titanium dioxide films," *Journal of Physical Chemistry*, vol. 100, no. 51, pp. 20056–20062, 1996.

[26] M. K. Nazeeruddin, A. Kay, I. Rodicio et al., "Conversion of light to electricity by cis-X2bis(2,2′-bipyridyl-4,4′-dicarboxylate)ruthenium(II) charge-transfer sensitizers (X = Cl^-, Br^-, I^-, CN^-, and SCN^-) on nanocrystalline TiO_2 electrodes," *Journal of the American Chemical Society*, vol. 115, no. 14, pp. 6382–6390, 1993.

[27] A. Hagfeldt and M. Grätzel, "Light-induced redox reactions in nanocrystalline systems," *Chemical Reviews*, vol. 95, no. 1, pp. 49–68, 1995.

[28] A. Yella, H. W. Lee, H. N. Tsao et al., "Porphyrin-sensitized solar cells with cobalt (II/III)-based redox electrolyte exceed 12 percent efficiency," *Science*, vol. 334, no. 6056, pp. 629–634, 2011.

[29] S. A. Haque, E. Palomares, B. M. Cho et al., "Charge separation versus recombination in dye-sensitized nanocrystalline solar cells: the minimization of kinetic redundancy," *Journal of the American Chemical Society*, vol. 127, no. 10, pp. 3456–3462, 2005.

[30] K. Pan, Y. Dong, C. Tian et al., "TiO_2-B narrow nanobelt/TiO_2 nanoparticle composite photoelectrode for dye-sensitized solar cells," *Electrochimica Acta*, vol. 54, no. 28, pp. 7350–7356, 2009.

[31] T. Berger, T. Lana-Villarreal, D. Monllor-Satoca, and R. Gómez, "An electrochemical study on the nature of trap states in nanocrystalline rutile thin films," *Journal of Physical Chemistry C*, vol. 111, no. 27, pp. 9936–9942, 2007.

[32] D. H. Chen, F. Z. Huang, Y. B. Cheng, and R. A. Caruso, "Mesoporous anatase TiO_2 beads with high surface areas and controllable pore sizes: a superior candidate for high-performance dye-sensitized solar cells," *Advanced Materials*, vol. 21, no. 21, pp. 2206–2210, 2009.

[33] J. F. Qian, P. Liu, Y. Xiao et al., "TiO_2-coated multilayered SnO_2 hollow microspheres for dye-sensitized solar cells," *Advanced Materials*, vol. 21, no. 36, pp. 3617–3667, 2009.

[34] M. J. Bierman and S. Jin, "Potential applications of hierarchical branching nanowires in solar energy conversion," *Energy and Environmental Science*, vol. 2, no. 10, pp. 1050–1059, 2009.

[35] L. Hu, S. Dai, J. Weng et al., "Microstructure design of nanoporous TiO_2 photoelectrodes for dye-sensitized solar cell modules," *Journal of Physical Chemistry B*, vol. 111, no. 2, pp. 358–362, 2007.

[36] M. Law, L. E. Greene, J. C. Johnson, R. Saykally, and P. Yang, "Nanowire dye-sensitized solar cells," *Nature Materials*, vol. 4, no. 6, pp. 455–459, 2005.

[37] K. Zhu, N. R. Neale, A. Miedaner, and A. J. Frank, "Enhanced charge-collection efficiencies and light scattering in dye-sensitized solar cells using oriented TiO_2 nanotubes arrays," *Nano Letters*, vol. 7, no. 1, pp. 69–74, 2007.

[38] G. K. Mor, K. Shankar, M. Paulose, O. K. Varghese, and C. A. Grimes, "Use of highly-ordered TiO_2 nanotube arrays in dye-sensitized solar cells," *Nano Letters*, vol. 6, no. 2, pp. 215–218, 2006.

[39] M. Y. Song, D. K. Kim, K. J. Ihn, S. M. Jo, and D. Y. Kim, "Electrospun TiO_2 electrodes for dye-sensitized solar cells," *Nanotechnology*, vol. 15, no. 12, pp. 1861–1865, 2004.

[40] W. Zhang, R. Zhu, L. Ke, X. Liu, B. Liu, and S. Ramakrishna, "Anatase mesoporous TiO_2 nanofibers with high surface area for solid-state dye-sensitized solar cells," *Small*, vol. 6, no. 19, pp. 2176–2182, 2010.

[41] Q. L. Huang, G. Zhou, L. Fang, L. Hu, and Z. S. Wang, "TiO_2 nanorod arrays grown from a mixed acid medium for efficient dye-sensitized solar cells," *Energy and Environmental Science*, vol. 4, no. 6, pp. 2145–2151, 2011.

[42] M. Adachi, Y. Murata, J. Takao, J. Jiu, M. Sakamoto, and F. Wang, "Highly efficient dye-sensitized solar cells with a titania thin-film electrode composed of a network structure of single-crystal-like TiO_2 nanowires made by the "oriented attachment" mechanism," *Journal of the American Chemical Society*, vol. 126, no. 45, pp. 14943–14949, 2004.

[43] X. Feng, K. Shankar, O. K. Varghese, M. Paulose, T. J. Latempa, and C. A. Grimes, "Vertically aligned single crystal TiO_2 nanowire arrays grown directly on transparent conducting oxide coated glass: synthesis details and applications," *Nano Letters*, vol. 8, no. 11, pp. 3781–3786, 2008.

[44] B. Liu and E. S. Aydil, "Growth of oriented single-crystalline rutile TiO_2 nanorods on transparent conducting substrates for dye-sensitized solar cells," *Journal of the American Chemical Society*, vol. 131, no. 11, pp. 3985–3990, 2009.

[45] A. Vomiero, V. Galstyan, A. Braga et al., "Flexible dye sensitized solar cells using TiO_2 nanotubes," *Energy and Environmental Science*, vol. 4, no. 9, pp. 3408–3413, 2011.

[46] L. L. Li, Y. J. Chen, H. P. Wu, N. S. Wang, and E. W. G. Diau, "Detachment and transfer of ordered TiO_2 nanotube arrays for front-illuminated dye-sensitized solar cells," *Energy and Environmental Science*, vol. 4, no. 9, pp. 3420–3425, 2011.

[47] L. D. Sun, S. Zhang, X. Wang, X. W. Sun, D. Y. Ong, and A. K. K. Kyaw, "A novel parallel configuration of dye-sensitized solar cells with double-sided anodic nanotube arrays," *Energy and Environmental Science*, vol. 4, no. 6, pp. 2240–2248, 2011.

[48] J. R. Jennings, A. Ghicov, L. M. Peter, P. Schmuki, and A. B. Walker, "Dye-sensitized solar cells based on oriented TiO_2 nanotube arrays: transport, trapping, and transfer of electrons," *Journal of the American Chemical Society*, vol. 130, no. 40, pp. 13364–13372, 2008.

[49] J. Jiu, F. Wang, S. Isoda, and M. Adachi, "Highly efficient dye-sensitized solar cells based on single crystalline TiO_2 nanorod film," *Chemistry Letters*, vol. 34, no. 11, pp. 1506–1507, 2005.

[50] J. Qu, G. R. Li, and X. P. Gao, "One-dimensional hierarchical titania for fast reaction kinetics of photoanode materials of dye-sensitized solar cells," *Energy and Environmental Science*, vol. 3, no. 12, pp. 2003–2009, 2010.

[51] E. Enache-Pommer, J. E. Boercker, and E. S. Aydil, "Electron transport and recombination in polycrystalline TiO_2 nanowire dye-sensitized solar cells," *Applied Physics Letters*, vol. 91, no. 12, Article ID 123116, 3 pages, 2007.

[52] M. Kläui, H. Ehrke, U. Rüdiger et al., "Direct observation of domain-wall pinning at nanoscale constrictions," *Applied Physics Letters*, vol. 87, no. 10, Article ID 102509, 3 pages, 2005.

[53] S. H. Kang, S. H. Choi, M. S. Kang et al., "Nanorod-based dye-sensitized solar cells with improved charge collection efficiency," *Advanced Materials*, vol. 20, no. 1, pp. 54–58, 2008.

[54] B. Tan and Y. Wu, "Dye-sensitized solar cells based on anatase TiO_2 nanoparticle/nanowire composites," *Journal of Physical Chemistry B*, vol. 110, no. 32, pp. 15932–15938, 2006.

[55] J. J. Wu, G. R. Chen, C. C. Lu, W. T. Wu, and J. S. Chen, "Performance and electron transport properties of TiO_2 nanocomposite dye-sensitized solar cells," *Nanotechnology*, vol. 19, no. 10, Article ID 105702, 2008.

[56] M. D. Hernández-Alonso, F. Fresno, S. Suárez, and J. M. Coronado, "Development of alternative photocatalysts to TiO_2: challenges and opportunities," *Energy and Environmental Science*, vol. 2, no. 12, pp. 1231–1257, 2009.

[57] S. Gubbala, V. Chakrapani, V. Kumar, and M. K. Sunkara, "Band-edge engineered hybrid structures for dye-sensitized solar cells based on SnO_2 nanowires," *Advanced Functional Materials*, vol. 18, no. 16, pp. 2411–2418, 2008.

[58] S. Uchida, R. Chiba, M. Tomiha, N. Masaki, and M. Shirai, "Application of titania nanotubes to a dye-sensitized solar cell," *Electrochemistry*, vol. 70, no. 6, pp. 418–420, 2002.

[59] T. Kasuga, M. Hiramatsu, A. Hoson, T. Sekino, and K. Niihara, "Formation of titanium oxide nanotube," *Langmuir*, vol. 14, no. 12, pp. 3160–3163, 1998.

[60] M. Adachi, Y. Murata, I. Okada, and S. Yoshikawa, "Formation of titania nanotubes and applications for dye-sensitized solar cells," *Journal of the Electrochemical Society*, vol. 150, no. 8, pp. G488–G493, 2003.

[61] Y. Lan, X. P. Gao, H. Y. Zhu et al., "Titanate nanotubes and nanorods prepared from rutile powder," *Advanced Functional Materials*, vol. 15, no. 8, pp. 1310–1318, 2005.

[62] J. Jiu, S. Isoda, M. Adachi, and F. Wang, "Dye-sensitized solar cells based on a single-crystalline TiO_2 nanorod film," *Journal of Physical Chemistry B*, vol. 110, no. 5, pp. 2087–2092, 2006.

[63] K. Shankar, G. K. Mor, H. E. Prakasam et al., "Highly-ordered TiO_2 nanotube arrays up to 220 μm in length: use in water photoelectrolysis and dye-sensitized solar cells," *Nanotechnology*, vol. 18, no. 6, Article ID 065707, 2007.

[64] X. Pan, C. H. Chen, K. Zhu, and Z. Y. Fan, "TiO_2 nanotubes infiltrated with nanoparticles for dye sensitized solar cells," *Nanotechnology*, vol. 22, Article ID 235402, 2011.

[65] O. K. Varghese, M. Paulose, and C. A. Grimes, "Long vertically aligned titania nanotubes on transparent conducting oxide for highly efficient solar cells," *Nature Nanotechnology*, vol. 4, no. 9, pp. 592–597, 2009.

[66] M. D. Ye, X. K. Xin, C. J. Lin, and Z. Q. Lin, "High efficiency dye-sensitized solar cells based on hierarchically structured nanotubes," *Nano Letters*, vol. 11, no. 8, pp. 3214–3220, 2011.

[67] M. Paulose, K. Shankar, O. K. Varghese, G. K. Mor, B. Hardin, and C. A. Grimes, "Backside illuminated dye-sensitized solar cells based on titania nanotube array electrodes," *Nanotechnology*, vol. 17, no. 5, pp. 1446–1448, 2006.

[68] J. M. Macák, H. Tsuchiya, A. Ghicov, and P. Schmuki, "Dye-sensitized anodic TiO_2 nanotubes," *Electrochemistry Communications*, vol. 7, no. 11, pp. 1133–1137, 2005.

[69] S. H. Kang, J. W. Lim, H. S. Kim, J. Y. Kim, Y. H. Chung, and Y. E. Sung, "Photo and electrochemical characteristics dependent on the phase ratio of nanocolumnar structured TiO_2 films by RF magnetron sputtering technique," *Chemistry of Materials*, vol. 21, no. 13, pp. 2777–2788, 2009.

[70] G. K. Mor, K. Shankar, M. Paulose, O. K. Varghese, and C. A. Grimes, "Enhanced photocleavage of water using titania nanotube arrays," *Nano Letters*, vol. 5, no. 1, pp. 191–195, 2005.

[71] M. Paulose, K. Shankar, S. Yoriya et al., "Anodic growth of highly ordered TiO_2 nanotube arrays to 134 μm in length," *Journal of Physical Chemistry B*, vol. 110, no. 33, pp. 16179–16184, 2006.

[72] J. H. Park, T. W. Lee, and M. G. Kang, "Growth, detachment and transfer of highly-ordered TiO_2 nanotube arrays: use in dye-sensitized solar cells," *Chemical Communications*, no. 25, pp. 2867–2869, 2008.

[73] S. P. Albu, A. Ghicov, J. M. Macak, R. Hahn, and P. Schmuki, "Self-organized, free-standing TiO_2 nanotube membrane for flow-through photocatalytic applications," *Nano Letters*, vol. 7, no. 5, pp. 1286–1289, 2007.

[74] J. Wang and Z. Q. Lin, "Freestanding TiO_2 nanotube arrays with ultrahigh aspect ratio via electrochemical anodization," *Chemistry of Materials*, vol. 20, no. 4, pp. 1257–1261, 2008.

[75] M. Paulose, K. Shankar, S. Yoriya et al., "Anodic growth of highly ordered TiO_2 nanotube arrays to 134 μm in length (Journal of Physical Chemistry B (2006) 110B)," *Journal of Physical Chemistry B*, vol. 112, no. 47, p. 15261, 2008.

[76] J. B. Baxter and E. S. Aydil, "Nanowire-based dye-sensitized solar cells," *Applied Physics Letters*, vol. 86, no. 5, Article ID 053114, 3 pages, 2005.

[77] C. Xu, P. H. Shin, L. Cao, J. Wu, and D. Gao, "Ordered TiO_2 nanotube arrays on transparent conductive oxide for dye-sensitized solar cells," *Chemistry of Materials*, vol. 22, no. 1, pp. 143–148, 2010.

[78] Q. Huang, G. Zhou, L. Fang, L. Hu, and Z. S. Wang, "TiO_2 nanorod arrays grown from a mixed acid medium for efficient dye-sensitized solar cells," *Energy and Environmental Science*, vol. 4, no. 6, pp. 2145–2151, 2011.

[79] T. Krishnamoorthy, V. Thavasi, G. M. Subodh, and S. Ramakrishna, "A first report on the fabrication of vertically aligned anatase TiO_2 nanowires by electrospinning: preferred architecture for nanostructured solar cells," *Energy and Environmental Science*, vol. 4, no. 8, pp. 2807–2812, 2011.

[80] S. Fujihara, E. Hosono, K. Kakiuchi, and H. Imai, "Growth of submicrometer-scale rectangular parallelepiped rutile TiO_2 films in aqueous $TiCl_3$ solutions under hydrothermal conditions," *Journal of the American Chemical Society*, vol. 126, no. 25, pp. 7790–7791, 2004.

[81] J. J. Wu and C. C. Yu, "Aligned TiO_2 nanorods and nanowalls," *Journal of Physical Chemistry B*, vol. 108, no. 11, pp. 3377–3379, 2004.

[82] Q. Zhou, X. F. Yang, S. Q. Zhang et al., "Rutile nanowire arrays: tunable surface densities, wettability and photochemistry," *Journal of Materials Chemistry*, vol. 21, no. 39, pp. 15806–15812, 2011.

[83] Y. Liu, H. Wang, Y. Wang, H. Xu, M. Li, and H. Shen, "Substrate-free, large-scale, free-standing and two-side oriented single crystal TiO_2 nanorod array films with photocatalytic

properties," *Chemical Communications*, vol. 47, no. 13, pp. 3790–3792, 2011.

[84] G. Wang, H. Wang, Y. Ling et al., "Hydrogen-treated TiO_2 nanowire arrays for photoelectrochemical water splitting," *Nano Letters*, vol. 11, no. 7, pp. 3026–3033, 2011.

[85] X. Feng, J. Zhai, and L. Jiang, "The fabrication and switchable superhydrophobicity of TiO_2 nanorod films," *Angewandte Chemie—International Edition*, vol. 44, no. 32, pp. 5115–5118, 2005.

[86] E. Barea, X. Q. Xu, V. Gonzalez-Pedro, T. Ripolles-Sanchis, F. Fabregat-Santiago, and J. Bisquert, "Origin of efficiency enhancement in Nb_2O_5 coated titanium dioxide nanorod based dye sensitized solar cells," *Energy and Environmental Science*, vol. 4, no. 9, pp. 3414–3419, 2011.

[87] M. Q. Lv, D. J. Zheng, M. D. Ye et al., "Densely aligned rutile TiO_2 nanorod arrays with high surface area for efficient dye-sensitized solar cells," *Nanoscale*, vol. 4, no. 19, pp. 5872–5879, 2012.

Hindawi Publishing Corporation
Journal of Nanomaterials
Volume 2013, Article ID 684797, 5 pages
http://dx.doi.org/10.1155/2013/684797

Research Article

Hybrid Ag_2O/ZnO Heterostructures

Jing Wang,[1] Yang Liu,[1] Yang Jiao,[1] Fengyu Qu,[1] Qingzhi Pan,[2] and Xiang Wu[1]

[1] *Key Laboratory for Photonic and Electronic Bandgap Materials of Ministry of Education and College of Chemistry and Chemical Engineering, Harbin Normal University, Harbin 150025, China*
[2] *State Key Laboratory for Inorganic Synthesis and Preparative Chemistry, Jilin University, Changchun 130023, China*

Correspondence should be addressed to Xiang Wu; wuxiang05@gmail.com

Received 15 January 2013; Accepted 22 January 2013

Academic Editor: Chuanfei Guo

The well-aligned Ag_2O/ZnO microflowers heterostructure was synthesized by a straightforward two-step procedure. The diameters of the as-synthesized products were as much as 1.5 μm. The as-grown Ag_2O/ZnO heterostructure was investigated by X-ray powder diffraction (XRD), scanning electron microscope (SEM), transmission electron microscope (TEM), and photoluminescence (PL) spectroscopy analysis. A possible growth mechanism for flowerlike Ag_2O/ZnO heterostructure was proposed based on the experimental results. Compared with pure ZnO microflowers, PL spectrum of the composite with only one strong peak at 383 nm showed good intrinsic emission.

1. Introduction

In recent years, nanostructured materials have been a wide research focus due to their versatile morphologies and excellent physical and chemical properties superior to the corresponding bulk counterparts [1–5]. Therefore, nanostructured materials have been used widely in gas sensors [6–8], photocatalysts [9–13], solar cells [13–15], and luminescent materials [16, 17]. However, in view of applications, it is restricted because single materials seldom meet actual demands. Thus, the challenge is to find some nanocomposites consisting of two or more semiconductors, which is considered a great choice to improve outstanding performance [18–21]. Zhou et al. reported Ag_2O/TiO_2 nanobelts heterostructure with better ultraviolet and visible photocatalytic activity than single TiO_2 materials [22]. Khanchandani and his coworkers demonstrated that type II ZnO/CdS core/shell nanorod arrays show enhanced simulated solar light absorption and high transfer efficiency of photogenerated electrons [23]. Li's group synthesized Ag-doped ZnO nanowires with excellent electical and optical properties [24].

ZnO, as a very important wide bandgap semiconductor material with large exciton binding energy of 60 meV at room temperature, has been a research focus in recent years for its three prominent characteristics: semiconductor, piezoelectricity, and biocompatibility. Therefore, it has been used in various fields such as optics, gas sensors, piezoelectronics, and self-clean energy [25, 26]. As mentioned above, since nanocomposites represent better properties, herein, we report the synthesis Ag_2O/ZnO nanohybrid with a feasible two-step method. A possible growth mechanism of the as-prepared Ag_2O/ZnO nanohybrid is proposed. The as-synthesized flowerlike Ag_2O-ZnO nanohybrid possesses an average diameter of 1.5 μm with uniformly distributed Ag_2O nanoparticles on ZnO microflowers. Room temperature photoluminescence properties of the as-prepared ZnO microflowers and Ag_2O/ZnO nanohybrid products were investigated. The spectrum presents only an ultraviolet emission peak at 383 nm for Ag_2O/ZnO nanohybrid, revealing an excellent optical quality.

2. Experiment Details

All the reagents in this experiment are analytically pure and used without further purification. A typical experiment procedure is described as follows.

2.1. Synthesis of ZnO Microflowers. In a typical procedure, 3 mmol $Zn(NO_3)_2$ was dissolved into 10 mL deionized water, and 12 mmol NaOH was dissolved into 20 mL deionized water in a 50 mL glass beaker with constantly stirring until

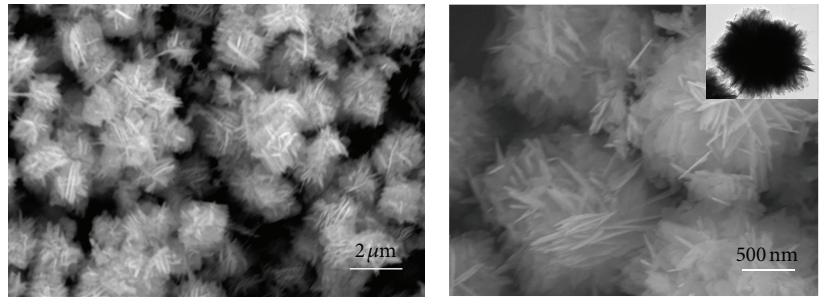

Figure 1: SEM images of ZnO microflowers: (a) low magnification SEM image, (b) high magnification SEM image. The inset is TEM image.

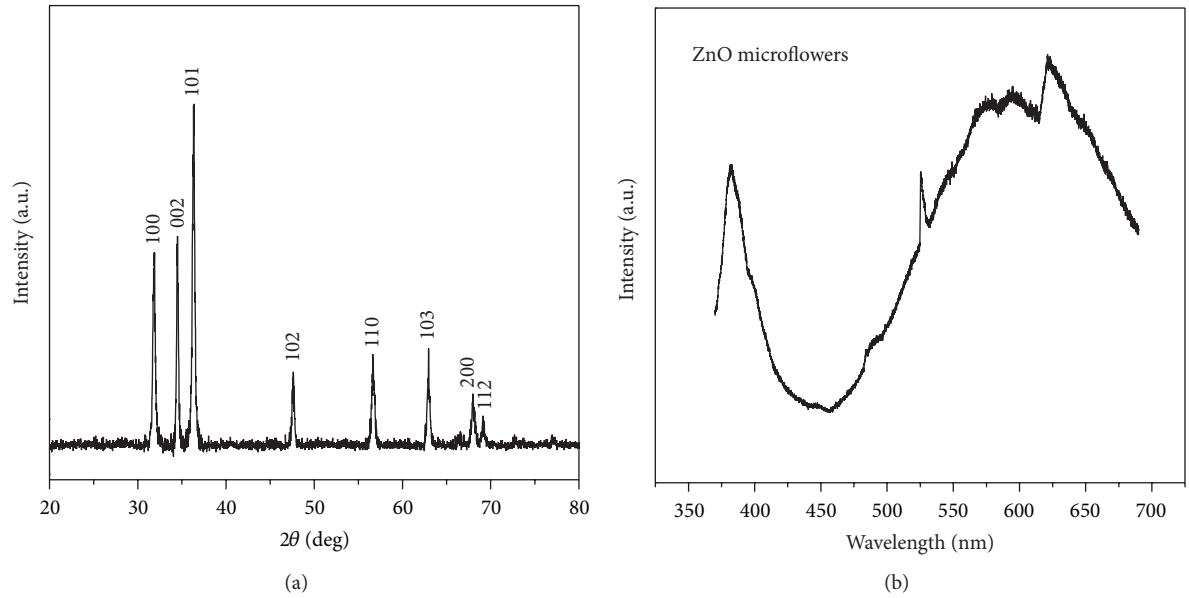

Figure 2: (a) XRD patterns of the as-synthesized ZnO microflowers. (b) Room-temperature photoluminescence spectrum of the as-synthesised ZnO microflowers.

the solution becomes transparent, respectively. Then, NaOH solution was added dropwise into the above solution under ceaselessly magnetic stirring for 1 h. The mixed solution was then put into a sealed Teflon-lined autoclave, followed by hydrothermal reaction at 90°C for 1.5 h. After that, the autoclave was naturally cooled to room temperature. The precursor precipitation was taken out and washed several times with deionized water and ethanol and dried at 60°C for 12 h in air.

2.2. Synthesis of Ag_2O/ZnO Heterostructures. In a typical experiment, 0.2 g $Ag(NO)_3$ and 0.48 g NaOH were dissolved into 20 mL deionized water in 100 mL glass beaker with constantly stirring until the solution becomes transparent, respectively. Then NaOH solution was added dropwise into the $Ag(NO)_3$ solution under ceaselessly magnetic stirring for 30 min. 0.20 g of ZnO was added to the suspension. The obtained mixture solution was illuminated with 250W metal-halide lamp for 1 h under magnetic agitation. After illumination, the products were thoroughly washed with water and ethanol and then dried at 60°C for 12 h in air.

The obtained product was characterized by scanning electron microscope (SEM, Hitachi-4800), transmission electron microscope (TEM, JEOL-2010), and X-ray powder diffraction (XRD, Rigaku Dmax-2600/PC, CuKα radiation, λ = 0.1542 nm, 40 KV, 100 mA). Optical property of the as-synthesised ZnO nanoflowers was investigated by photoluminescence spectroscopy (PL SPEX FL-2T2).

3. Results and Discussion

The morphology and microstructural details of the as-prepared ZnO microflowers were investigated by SEM and TEM observation. Figure 1(a) shows a low magnification SEM image of the as-obtained product. It may clearly be found that the as-obtained product possesses many flowerlike structures. Further, high magnification SEM image reveals that individual microflower is assembled from numerous

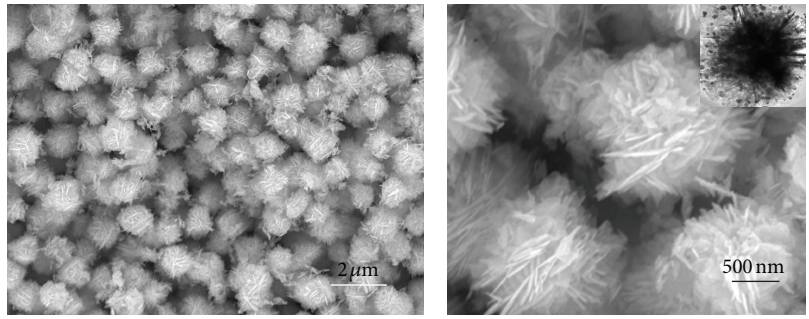

Figure 3: SEM images of Ag_2O/ZnO heterostructure: (a) low magnification SEM image, (b) high magnification SEM image. The inset is TEM image.

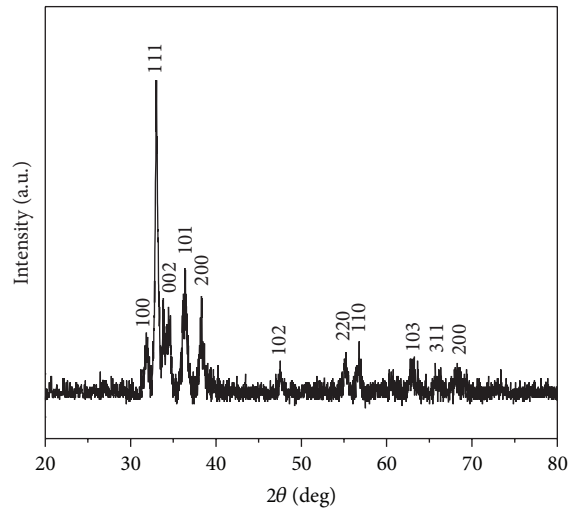

Figure 4: XRD patterns of the as-synthesized Ag_2O/ZnO heterostructure.

nanosheets, and the diameter of the product is about 1.5 μm as shown in Figure 1(b). The inset is TEM images, which further conform that the as-prepared products are flowerlike structures by some nanosheets assembled. The typical XRD pattern of the prepared ZnO sample is presented in Figure 2(a). All the diffraction peaks can be perfectly indexed to hexagonal wurtzite-type ZnO (JCPDS no. 36-1451). No peaks of other impurities are detected in this case. The strong and sharp peaks indicate that the as-prepared product is highly crystalline.

To investigate optical properties of the nanostructures, photoluminescence (PL) spectra were measured with an excitation wavelength of 325 nm at room temperature, as presented in Figure 2(b). The PL spectra of the flowerlike ZnO nanostructures prepared were dominated by a sharp emission band with a λ_{max} at 380 nm along with a broad, strong band in the higher wavelength region of 500–660 nm. The UV peak could be generally attributed to the near-band-edge emission (NBE), and the visible band (known as deep level emission, DLE) is usually caused by impurities and structural defects [27]. The strong, broad emission band in the higher wavelength region is termed a deep-level or trap-state emission band, which might be the superposition of green emission around 520 nm and a near-yellow emission around 640 nm as reported elsewhere [28, 29]. This trap-state emission is usually associated with various types of defects resulting from various oxygen vacancies in the valence band of ZnO nanostructures [30, 31]. Figure 3 shows SEM image of the as-obtained Ag_2O/ZnO nanohybrid product. In contrast, ZnO microflowers with coated Ag_2O exhibited a rough surface where a number of Ag_2O particles were absorbed on the surface of ZnO microflowers. The inset shows the corresponding TEM image, which demonstrates clearly some Ag_2O nanoparticles coated on the surface of ZnO microflowers. XRD patterns of Ag_2O/ZnO heterostructure are shown in Figure 4. The hexagonal ZnO and Ag_2O phases coexist in the Ag_2O/ZnO heterostructure crystals, and the XRD patterns match their JCPDS files nos. 36-1451 and 41-1104, respectively. No peaks of other phases were detected, indicating high purity of the as-synthesized product.

On the basis of the above observations, a possible growth mechanism of the Ag_2O/ZnO heterostructure is proposed in Figure 5. First, OH^- reacts with Zn^{2+} to form $Zn(OH)_2$, then $Zn(OH)_4^{2-}$ ions. Synthesis of ZnO micro/nanostructures from aqueous solution containing $Zn(OH)_4^{2-}$ ions has been reported. As reaction time proceeds, $Zn(OH)_4^{2-}$ ions dehydrate and form ZnO nuclei under hydrothermal conditions. These particles have a tendency to aggregate due to large surface energy. Surface energy is substantially reduced when the neighboring nanosheets are grown. With the crystal growth continuing, each nanoparticle in the aggregates or nanosheet has its own orientation and acts as a nucleus for further growth. These growth processes are not only related to the anisotropic ZnO crystal structure, but also the involved reaction conditions [32]. The growth habit can control the ZnO crystals to grow into nanosheets. At the same time, conventional nucleation on the nanosheet occurs for the high concentration of $Zn(OH)_4^{2-}$ transforming to ZnO. Then, flowerlike ZnO hierarchical structures are formed by two-step nucleation and growth process [33, 34]. Some Ag_2O particle seeds are then partially deposited on the surface of ZnO microflowers to form nucleation sites for subsequent growth of Ag_2O particles. During early stages of the reaction,

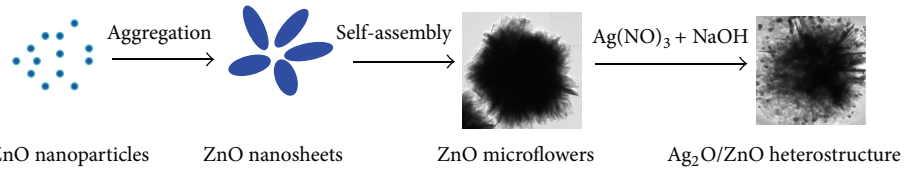

Figure 5: Schematic illustration of the possible formation mechanism of the as-synthesized Ag_2O/ZnO heterostructure.

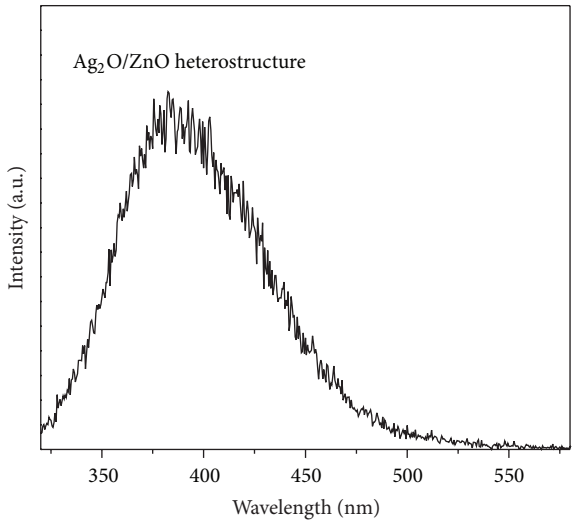

Figure 6: Room-temperature photoluminescence spectrum of the as-synthesised Ag_2O/ZnO heterostructure.

Ag_2O crystal nuclei are formed on the ZnO lateral surface by the reduction reaction of $Ag(NO)_3$. With increasing reaction time, initial particle seeds continuously aggregate and crystallize, leading to increasing diameters of the Ag_2O nanoparticles. At last, a dense and complex Ag_2O/ZnO microflowerlike heterostructure is formed.

Finally, room-temperature photoluminescence property of the as-synthesised Ag_2O/ZnO heterostructure was also investigated. Figure 6 shows a PL spectrum of the obtained Ag_2O/ZnO heterostructure. Only a single wide emission peak centered at 383 nm was observed, which may be attributed to the recombination of free excitons through an exciton-exciton collision process [27]. No other peaks were found, illustrating that the as-synthesized Ag_2O/ZnO heterostructure have a better crystal quality and stoichiometry compared with single ZnO microflowers materials.

4. Conclusions

In summary, flowerlike Ag_2O/ZnO heterostructure hybrids have been successfully synthesized by a simple two-step procedure without any surfactants. The as-prepared heterostructure composite showed Ag_2O nanoparticles coated uniformly on the surface of ZnO microflowers. The possible growth mechanism of the products is proposed based on these experimental results. PL measurements reveal a strong UV band-edge emission peak at 383 nm. Comparing with pure ZnO microflowers, the composite exhibited greatly optical properties.

Acknowledgments

This work was supported by the Foundation for Key Project of Ministry of Education, China (no. 211046), Open Fund of State Key Laboratory of Inorganic Synthesis and Preparative Chemistry, Jilin University (no. 2012-22), Program for New Century Excellent Talents in Heilongjiang Provincial University (1252-NCET-018), and Program for Scientific and Technological Innovation Team Construction in Universities of Heilongjiang (no. 2011TD010).

References

[1] C. Burda, X. Chen, R. Narayanan, and M. A. El-Sayed, "Chemistry and properties of nanocrystals of different shapes," *Chemical Reviews*, vol. 105, no. 4, pp. 1025–1102, 2005.

[2] F. Cheng, J. Zhao, W. Song et al., "Facile controlled synthesis of MnO_2 nanostructures of novel shapes and their application in batteries," *Inorganic Chemistry*, vol. 45, no. 5, pp. 2038–2044, 2006.

[3] Q. Wan, Q. H. Li, Y. J. Chen et al., "Fabrication and ethanol sensing characteristics of ZnO nanowire gas sensors," *Applied Physics Letters*, vol. 84, no. 18, pp. 3654–3656, 2004.

[4] H. B. Chen, X. Wu, L. H. Gong, C. Ye, F. Y. Qu, and G. Z. Shen, "Hydrothermally-grown ZnO micro/nanotube arrays and their properties," *Nanoscale Research Letters*, vol. 5, pp. 570–575, 2010.

[5] Z. L. Zhang, J. Wang, Z. Yu, F. Y. Qu, and X. Wu, "Assembling SnO nanosheets into microhydrang-eas: gas Phase synthesis and their optical property," *Nano-Micro Letters*, vol. 4, pp. 215–219, 2012.

[6] Y. J. Chen, C. L. Zhu, and G. Xiao, "Ethanol sensing characteristics of ambient temperature sonochemically synthesized ZnO nanotubes," *Sensors and Actuators B*, vol. 129, no. 2, pp. 639–642, 2008.

[7] C. M. Chang, M. H. Hon, and I. C. Leu, "Preparation of ZnO nanorod arrays with tailored defect-related characterisitcs and their effect on the ethanol gas sensing performance," *Sensors and Actuators B*, vol. 151, no. 1, pp. 15–20, 2010.

[8] A. Gurlo, "Nanosensors: towards morphological control of gas sensing activity. SnO_2, In_2O_3, ZnO and WO_3 case studies," *Nanoscale*, vol. 3, no. 1, pp. 154–165, 2011.

[9] B. X. Jia, W. N. Jia, Y. L. Ma, X. Wu, and F. Y. Qu, "SnO_2 core-shell microspheres with excellent photocatalytic properties," *Science of Advanced Materials*, vol. 4, no. 1, pp. 702–707, 2012.

[10] D. G. Chen, F. Huang, G. Q. Ren et al., "ZnS nano-architectures: photocatalysis, deactivation and regeneration," *Nanoscale*, vol. 2, no. 10, pp. 2062–2064, 2010.

[11] B. Liu, Z. R. Wang, Y. Dong et al., "ZnO-nanoparticle-assembled cloth for flexible photodetectors and recyclable photocatalysts," *Journal of Materials Chemistry*, vol. 22, no. 18, pp. 9379–9384, 2012.

[12] Y. T. Han, X. Wu, Y. L. Ma, L. Gong, F. Qu, and H. Fan, "Porous SnO_2 nanowire bundles for photocatalyst and Li ion battery applications," *CrystEngComm*, vol. 13, no. 10, pp. 3506–3510, 2011.

[13] Q. Zhang, T. P. Chou, B. Russo, S. A. Jenekhe, and G. Cao, "Aggregation of ZnO nanocrystallites for high conversion efficiency in dye-sensitized solar cells," *Angewandte Chemie*, vol. 47, no. 13, pp. 2402–2406, 2008.

[14] J. B. Baxter and E. S. Aydil, "Dye-sensitized solar cells based on semiconductor morphologies with ZnO nanowires," *Solar Energy Materials and Solar Cells*, vol. 90, no. 5, pp. 607–622, 2006.

[15] Q. Zhang, T. P. Chou, B. Russo, S. A. Jenekhe, and G. Cao, "Aggregation of ZnO nanocrystallites for high conversion efficiency in dye-sensitized solar cells," *Angewandte Chemie*, vol. 47, no. 13, pp. 2402–2406, 2008.

[16] D. J. Gargas, M. E. Toimil-Molares, and P. Yang, "Imaging single ZnO vertical nanowire laser cavities using UV-laser scanning confocal microscopy," *Journal of the American Chemical Society*, vol. 131, no. 6, pp. 2125–2127, 2009.

[17] Y. Lei, X. Wu, and F. Y. Qu, "Assembling ZnO nanorods into microflowers through a facile solution strategy: morphology control and cathodoluminescence properties," *Nano-Micro Letters*, vol. 4, no. 1, pp. 45–51, 2012.

[18] C. H. Wang, C. L. Shao, X. T. Zhang, and Y. C. Liu, "SnO_2 nanostructures-TiO_2 nanofibers heterostructures:controlled fabrication and high photocatalytic properties," *Inorganic Chemistry*, vol. 48, no. 15, pp. 7261–7268, 2009.

[19] P. Wang, B. Huang, X. Zhang et al., "Highly efficient visible-light plasmonic photocatalyst Ag@AgBr," *Chemistry A*, vol. 15, no. 8, pp. 1821–1824, 2009.

[20] L. R. Zheng, Y. H. Zheng, C. Q. Chen et al., "Network structured SnO_2/ZnO heterojunction nanocatalyst with high photocatalytic activity," *Inorganic Chemistry*, vol. 48, no. 5, pp. 1819–1825, 2009.

[21] G. Xi, B. Yue, J. Cao, and J. Ye, "Fe_3O_4/WO_3 Hierarchical core-shell structure: high-performance and recyclable visible-light photocatalysis," *Chemistry A*, vol. 17, no. 18, pp. 5145–5154, 2011.

[22] W. Zhou, H. Liu, J. Wang, D. Liu, G. Du, and J. Cui, "Ag_2O/TiO_2 nanobelts heterostructure with enhanced ultraviolet and visible photocatalytic activity," *ACS Applied Materials and Interfaces*, vol. 2, no. 8, pp. 2385–2392, 2010.

[23] S. Khanchandani, S. Kundu, A. Patra, and A. K. Ganguli, "Shell thickness dependent photocatalytic properties of ZnO/CdS core-shell nanorods," *Journal of Physical Chemistry C*, vol. 116, no. 44, pp. 23653–23662, 2012.

[24] Y. Li, X. Zhao, and W. Fan, "Structural, electronic, and optical properties of Ag-doped ZnO nanowires: first principles study," *Journal of Physical Chemistry C*, vol. 115, no. 9, pp. 3552–3557, 2011.

[25] L. Gong, X. Wu, C. Ye, F. Qu, and M. An, "Aqueous phase approach to ZnO microspindles at low temperature," *Journal of Alloys and Compounds*, vol. 501, no. 2, pp. 375–379, 2010.

[26] B. Liu, Z. R. Wang, Y. Dong et al., "ZnO-nanoparticle-assembled cloth for flexible photodetectors and recyclable photocatalysts," *Journal of Materials Chemistry*, vol. 22, no. 18, pp. 9379–9384, 2012.

[27] E. M. Wong and P. C. Searson, "Electrophoretic deposition of ZnO quantum particle thin films," *Applied Physics Letters*, vol. 74, no. 20, pp. 2939–2942, 1999.

[28] A. B. Djurisic and Y. H. Leung, "Optical properties of ZnO nanostructures," *Small*, vol. 2, no. 8-9, pp. 944–961, 2006.

[29] A. B. Djurisic, W. C. H. Choy, V. A. L. Roy et al., "Photoluminescence and electron paramagnetic resonance of ZnO tetrapod structures," *Advanced Functional Materials*, vol. 14, no. 9, pp. 856–864, 2004.

[30] R. Dingle, "Luminescent transitions associated with divalent copper impurities and the green emission from semiconducting zinc oxide," *Physical Review Letters*, vol. 23, no. 11, pp. 579–581, 1969.

[31] U. Ozgur, I. A. Ya, C. Liu et al., "Comprehensive review of ZnO materials and devices," *Journal of Applied Physics*, vol. 98, pp. 0413011–041301103, 2005.

[32] J. B. Lian, Z. M. Ding, F. L. Kwong, and D. H.L. Ng, "Template-free hydrothermal synthesis of hexagonal ZnO micro-cups and micro-rings assembled by nanoparticles," *CrystEngComm* , vol. 13, no. 15, pp. 4820–4822, 2011.

[33] S. W. Cao and Y. J. Zhu, "Surfactant-free preparation and drug release property of magnetic hollow core-shell hierarchical nanostructures," *Journal of Physical Chemistry C*, vol. 112, no. 32, pp. 12149–12156, 2008.

[34] J. R. Huang, Y. J. Wu, C. P. Gu et al., "Large-scale synthesis of flowerlike ZnO nanostructure by a simple chemical solution route and its gas-sensing property," *Sensors and Actuators B*, vol. 146, no. 1, pp. 206–212, 2010.

Hindawi Publishing Corporation
Journal of Nanomaterials
Volume 2013, Article ID 196521, 9 pages
http://dx.doi.org/10.1155/2013/196521

Review Article

ZnO-Based Transparent Conductive Thin Films: Doping, Performance, and Processing

Yanli Liu, Yufang Li, and Haibo Zeng

College of Material Science and Technology, Nanjing University of Aeronautics and Astronautics, Nanjing 210016, China

Correspondence should be addressed to Haibo Zeng; zeng.haibo.nano@gmail.com

Received 21 December 2012; Accepted 2 February 2013

Academic Editor: Xijin Xu

ZnO-based transparent conductive thin films have attracted much attention as a promising substitute material to the currently used indium-tin-oxide thin films in transparent electrode applications. However, the detailed function of the dopants, acting on the electrical and optical properties of ZnO-based transparent conductive thin films, is not clear yet, which has limited the development and practical applications of ZnO transparent conductive thin films. Growth conditions such as substrate type, growth temperature, and ambient atmosphere all play important roles in structural, electrical, and optical properties of films. This paper takes a panoramic view on properties of ZnO thin films and reviews the very recent works on new, efficient, low-temperature, and high-speed deposition technologies. In addition, we highlighted the methods of producing ZnO-based transparent conductive film on flexible substrate, one of the most promising and rapidly emerging research areas. As optimum-processing-parameter conditions are being obtained and their influencing mechanism is becoming clear, we can see that there will be a promising future for ZnO-based transparent conductive films.

1. Introduction

Transparent conductive oxides (TCOs), capable of transporting electrical charge and transmitting visible photon, are necessary for use as transparent electrodes in flat panel displays such as liquid crystal displays (LCDs), plasma display panels, electronic paper displays, light-emitting-diodes (LEDs) [1], and touch panels [2, 3]. A carrier concentration on the order of 10^{20} cm^{-3} or higher and a band-gap energy above 3 eV are usually required for high conductivity and transmittance [4]. Various TCO thin films consisting of impurity-doped SnO_2 (SnO_2:Sb and SnO_2:F), In_2O_3 (In_2O_3:Sn, or ITO), and ZnO (ZnO:Al and ZnO:Ga) films have been researched so far in this field [5, 6]. Among them, tin-doped indium-oxide (ITO) is the one in practical use [7, 8]. However, with the market of ITO expanding, a stable supply may be difficult to ensure because of the high cost and scarcity of indium [9, 10].

Fortunately, ZnO thin films are a promising alternative to the commonly used ITO, which are low cost, nontoxic, highly durable against hydrogen plasma compared to ITO [11]. Besides, it has a more proper work function for the transparent contact cathode electrodes of transparent OLEDs [12]. Nevertheless, many problems associated with substituting ZnO-based TCO films for ITO still exist. Figure 1 visually describes structural, optical, electrical properties of zinc oxide. In LCD applications, stability in various environments has to be improved when films become thinner. [13]. In OLEDs applications, preparation technology of low-temperature and plasma damage-free films on flexible substrate have to be optimized.

For the design and realization of ZnO-based devices, one of the most significant issues is doping, which necessarily involves the heavy doping with trivalent elements from the group III (Al, Ga, In). Minami summed up the resistivity of impurity-doped binary compound TCO films reported among thirty years and found that the obtained minimum resistivity of impurity-doped ZnO films is still decreasing, while SnO_2 and In_2O_3 films have essentially remained unchanged [4]. Such trend indicates the possible significant promotion of ZnO-based TCO films.

ZnO films have been prepared through various kinds of methods [14, 15] and each of them has its own advantages and drawbacks. In this paper, sputtering, chemical vapor deposition (CVD), and pulsed laser deposition (PLD) are

Table 1: Properties of ZnO films with different dopants prepared by PLD.

Dopants	Optimum content in target (%)	Thickness (nm)	Resistivity (Ω·cm)	Transmittance (%)	Reference
Al	2	500	4.5×10^{-4}	88%	[35]
Ga	5	200	8.12×10^{-4}	>90%	[22]
In	40	>1000	4.02×10^{-4}	>85%	[36]
F	2	200	4.83×10^{-4}	>90%	[25]
Si	2	~150	6.2×10^{-4}	~80%	[37]

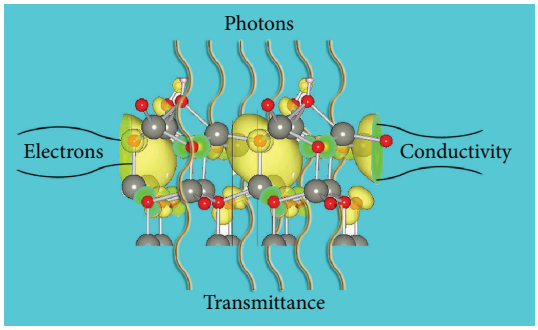

Figure 1: A picture visually describing structural, optical, electrical properties of zinc oxide. Revised from [38]. Copyright 2012, American Chemistry Society.

described in details, since ZnO-based TCO films based on these methods can get the highest quality. The first two methods allowing large area deposition make them the most advanced and efficient deposition techniques for ZnO film. Even if the films are prepared by the same method, thickness, substrate, growth temperature, dopant, and their content will play a crucial role in structural, electrical, and optical properties of films. Therefore, whether we can optimize the fabrication of high-quality doped zinc oxide thin films at low cost determines the future of ZnO-based TCO films. The structural, optical, electrical properties of doped ZnO are summarized with particular emphasis on influence of doping on the properties of ZnO thin films, which are responsible for the properties of films. In addition, recent progress on film preparation is introduced.

2. Different Dopant Elements

Several elements are doped in ZnO films, such as B [16, 17], Al, Ga, In (from group III elements) [18], F (from group VII element) [19], and so forth. Among them the most studied are Al-doped ZnO and Ga-doped ZnO. In Section 2, we focus on recent research on Al, Ga doping, and codoping. The position of the dopant atoms and solubility limit can be related to the film preparation methods. For example, in the spray pyrolysis technique, In and Ga is more efficient than Al since the Al atoms are preferably at interstitial sites of the ZnO lattice and decrease the mobility [20].

Some reported electrical and optical properties of ZnO films with different dopants prepared by PLD are summarized in Table 1. Each dopant was at its appropriate content and all films were fabricated under optimum-processing-parameter conditions to achieve lower resistivity and higher transmittance.

2.1. Group III Elements Doping. The ionic radius of Al^{3+} is 0.54 Å, which is smaller than that of Zn^{2+} (0.74 Å). So the Al^{3+} can occupy the place of Zn^{2+} in lattice easily, leading to a reduction of the lattice parameter. In comparison with Al^{3+}, Ga^{3+} has similar ionic radius to Zn^{2+} ions, which minimizes the ZnO lattice deformations even at higher doping concentrations [18, 21]. This may explain the reason why the best electrical properties of ZnO-based films are observed in Ga-doped ZnO thin films [22].

The conductive property of ZnO thin films is primarily dominated by electrons generated by oxygen vacancies and charge donation. Geng and his coworkers [23] investigated the effect of Al concentration on the electrical properties of ZnO:Al thin films grown on Si(100) substrate by atomic layer deposition. The crystallinity of the film degenerated while resistivity was found to decrease with increasing Al doping concentration (9.36×10^{-4} Ω·cm at maximal doping concentration 2.7 at.%).

Al is incorporated beyond the thermodynamic solubility limit, even within the limit, the relationship between Al content and resistivity is not monotonous [24]. The resistivity of the AZO film decreased with an increase of the Al content up to 7 at.% and then increased at a high Al content of 8 at.% (Figure 2). At high Al concentration, Al exists in the form of Al_2O_3, resulting in deleterious effects to the electrical properties of the films. According to many other reports, the relationship between conduction characteristics and concentration of other elements doping is similar to that of Al doping.

Fluorine is another dopant to improve the conductivity of the films [19]. Unlike aluminum and other elements in group III, effect of fluorine in ZnO is less discussed. Fluorine incorporates into the lattice by substituting oxygen atoms due to the comparability of ionic radius (F-: 1.17 Å, O^{2-}: 1.22 Å). Actually, ZnO:F films have good combination properties. Cao et al. [25] prepared FZO films via pulsed laser deposition, getting a resistivity of 4.8×10^{-4} Ω·cm, carrier concentration of 5.43×10^{20} cm^{-3}, and Hall mobility of 23.8 $cm^2V^{-1}s^{-1}$, respectively. The average optical transmittance in the entire visible wavelength region was higher than 90%.

2.2. Codoping. Difference of radii between doping ions and Zn^{2+} ions or O^{2-} ions will result in variation of lattice constant and degeneration of crystallinity in zinc oxide.

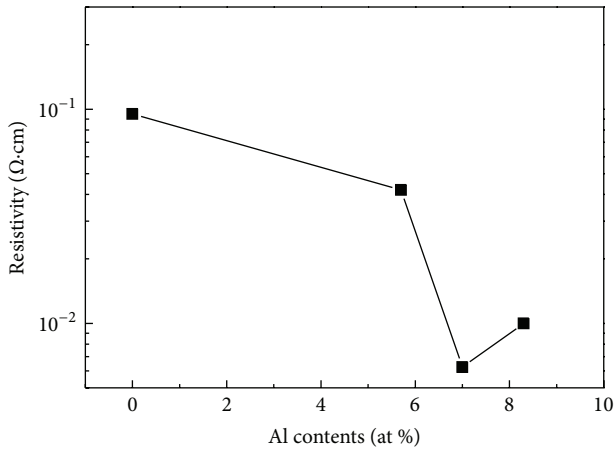

Figure 2: Resistivity as a function of Al contents from 0 to 8.4 at.% achieved by Hall measurement at room temperature [24]. Copyright 2011, The Electrochemical Society.

This issue could be partially resolved by codoping, which has led to an upsurge study in recent years [26–28]. High quality of films deposited by Shin et al. has confirmed the advantages of codoping [29]. As Ga concentration increased from 0.5 to 2 at%, the peak intensity of the (0002) plane and carrier concentration for Mg and Ga codoped ZnO thin films (MGZO) increase compared with that of pure ZnO and Mg-doped ZnO thin films, as shown in Figure 3 [29], implying the substitution of Ga^{3+} ions with Zn^{2+} ions (ionic radius of Ga^{3+}, Mg^{2+}, and Zn^{2+} is 0.062 nm, 0.057 nm, and 0.060 nm, resp.). What is more, the MGZO structure was stabilized greatly in this method. The low electrical resistivity and wide band gap energy of MGZO thin films can be ascribed to the dopant of Ga and Mg, respectively.

3. Doping Concentration

3.1. Concentration-Dependent Conductivity. Zinc oxide, as a transparent oxide with band-gap energy of 3.37 eV [30], can satisfy the optical properties requirement of TCO without doping. However, the carrier concentration of intrinsic ZnO is roughly 10^6 cm^{-3} at room temperature [31], which is much lower than that of TCO films for practical application. In general, an introduction of dopants affords an increase in carrier concentration, that is,

$$n_0 \cdot p_0 = n_i^2, \tag{1}$$

where n_0 is the concentration of conductive electrons, p_0 is the concentration of hole, and n_i is s intrinsic carrier concentration in ZnO. Doping directly affects carrier concentration and influences conductivity in turn. Although introduced impurities are necessary, but not more is better. Its concentration must have a limitation; otherwise, very high doping levels will result in high free carrier absorption, high plasma resonance reflectivity, and low visible wavelength transparency (Figure 2). Even though it seems difficult to improve electrical conduction while maintaining the optical transmission, there is the potential to achieve both through improving the microstructure of the films and increasing the carrier mobility. Obviously, it is important to deconstruct the influence of intentionally introduced impurities on electrical properties of ZnO to realize any type of device applications.

3.2. Concentration-Dependent Optical Gap Shift. The optical-gap shift is contributed by two competing effects, Burstein-Moss (B-M) band-filling effect and band-gap narrowing (BGN) effect (Figure 4). The well-known optical band-gap ($E_{g\,\mathrm{op}}$) blue shift [32, 33] in heavily doped semiconductors occurs because the lower states in the conduction band are blocked. Conversely, band-gap narrowing is caused by exchange interactions in the free-electron gas and electrostatic interactions between free electrons and ionized impurities. The fact that BGN effect is largely compensated by B-M effect and temperature or doping are two influence factors in the $E_{g\,\mathrm{op}}$ behavior makes it difficult to separate these two effects by means of current experiments.

Lu and coworkers [34] found that $E_{g\,\mathrm{op}}$, evaluated from optical absorption spectra, was mainly related to the carrier concentrations and so intrinsic to Al content. The optical gap increased with the electron concentration when $n_e \leq 4.2 \times 10^{19}$ cm^{-3}, which could be fully interpreted by a modified Burstein-Moss effect; A sudden decrease in energy gap occurred at $5.4–8.4 \times 10^{19}$ cm^{-3}, consistent with the Mott criterion for a SMT. Above the critical values, the band gap increased again (see Figure 5). Further exploration in this issue is needed to promote energy band engineering in ZnO-based TCO films.

4. Effect of Growth Conditions

4.1. Preparation Methods. Among various preparation methods, pulsed laser deposition (PLD) is more appropriate for precise controlling of morphology and composition of the grown materials. Park et al. and Agura et al. [22, 39] prepared AZO and GZO thin films on glass substrates with a low resistivity on the order of 10^{-5} Ω·cm by PLD, respectively. Resistivity on the order of 10^{-5} Ω·cm is the best result for ZnO films ever reported and there is a general agreement on the better performances in terms of conductivity for ZnO films grown by PLD than those obtained via other techniques. However, the problems of stability and cost most probably constrained the future development of this method in manufacture on a large scale.

Magnetron sputtering is one of the deposition methods in practical use. It was found that the lowest resistivity prepared by this method is still on the order of 10^{-4} Ω·cm, higher than the resistivities obtain by PLD several years ago. Chemical-vapor-deposition is another industrially most advanced deposition techniques. How to increase growth rate and applied to continuous, in-line manufacturing is a vital issue. Illiberi et al. deposited ZnO:Al films on glass by an industrially scalable metal organic chemical-vapor-deposition (MOCVD) technique at atmospheric pressure [40, 41]. In view of an industrial up-scale, the vaporized

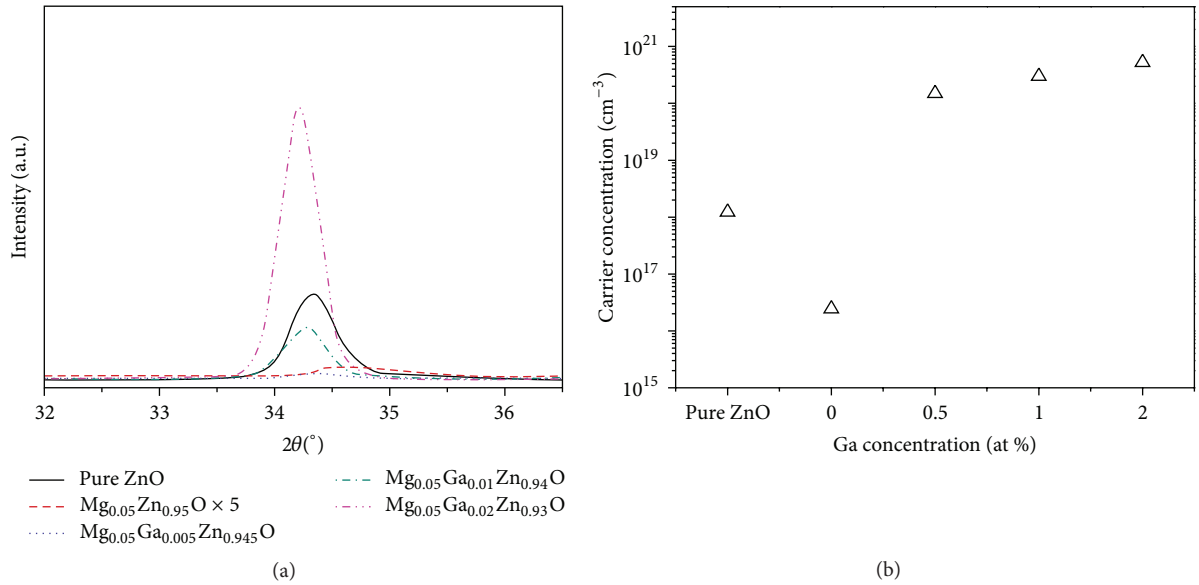

FIGURE 3: XRD patterns (a) and variation of the carrier concentration (b) of the pure ZnO, MZO, and MGZO thin films deposited at different Ga concentration [29]. Copyright 2011, American Chemistry Society.

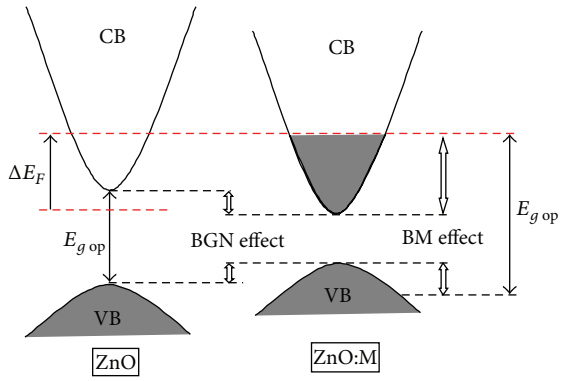

FIGURE 4: Band-gap renormalization and Burstein-Moss (B-M) band-filling effect contributions to the $E_{g\,\mathrm{op}}$.

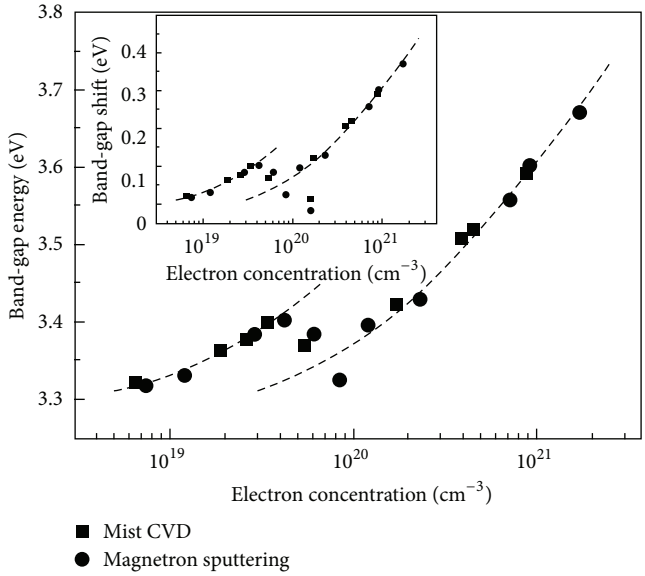

FIGURE 5: Band-gap energy as a function of electron concentration in AZO [34]. Copyright 2007, American Institute of Physics.

precursors, that is, diethylzinc (DEZ), Tertiary-butanol (t-BUT), and trimethylaluminum (TMA), can be injected in different deposition zones, where each layer is deposited. Then, each zone installed along the same production line continuous, realizing in-line manufacturing. Schematic of an industrial atmospheric-pressure MOCVD system is shown in Figure 6. A maximum growth rate was found at a deposition temperature of 480°C, for which ZnO_x:Al films show good crystalline quality, high conductivity ($R < 10\,\Omega/\square$ for film thicknesses above 1050 nm), and good transmittance (>85% in the visible range).

Sol-gel method is an attractive liquid-phase routes for obtaining thin films due to its advantages of easy control of the film composition and fabrication of a large area thin film with low cost. Luo et al. [45] developed a versatile film-deposition process combining microwave-assisted non-aqueous sol-gel process with dip-coating. The resistivity of obtained films was a little high (minimum resistivity is $2.35 \times 10^{-2}\,\Omega\cdot$cm) but their results are still promising on the way to the development of liquid-phase routes. To produce TCO films of good quality, every step of sol-gel method, including synthesis of nanoparticles, preparation of dispersions, thin-film processing, and postannealing, has to be optimized.

4.2. Substrate Type. Up to now, transparent conductive films have been prepared on plenty of different substrates, such as glass, sapphire, and polymer. Polymeric substrates,

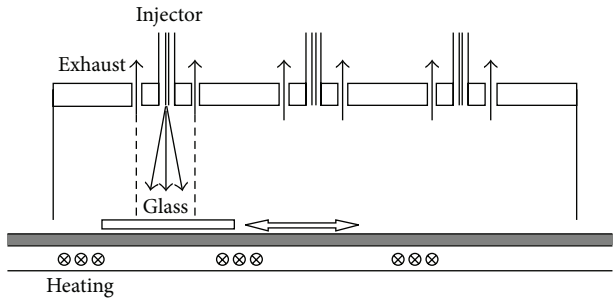

Figure 6: Schematic of an industrial atmospheric-pressure MOCVD system. Films have been deposited by using one injector. The system can be upscaled for industrial production by installing multiples injectors [40]. Copyright 2011, Elsevier.

polyethylene-terephthalate (PET) [46], polycarbonate (PC) [47], aspolyphthalamide (PPA) are drawing increasing attention due to their merits of light weight, low cost, ability to flex, curve, roll, fold small volume and promising application in organic light-emitting diodes (OLEDs) [48, 49].

Substrates nature alone may still affect microstructures (crystallization, morphology) and electrical properties of films. Esmaili-Sardari et al. have a research on conductivity type dependent on different substrates [50]. All films grown on boron doped p-Si have n-type conductivity at low Hall Effect temperatures and p-type conductivity at high Hall Effect temperatures but films grown n-type substrate show n-type behavior for the entire Hall temperatures range from 80 to 350 K, suggesting that the differences in nearly substrates surfaces could affect intrinsic defects and concentrations as well as the ZnO (0001) surface termination.

Shin et al. prepared thin films of Ga-doped ZnO (GZO) on glass and Al_2O_3 (0001) substrates by using RF magnetron sputtering under the same processing conditions and found that individual grains with columnar shape are clearly observed in the GZO film on the glass substrate, as shown in Figure 7(a). However, it is difficult to distinguish individual grains in the GZO film on the Al_2O_3 substrate (Figure 7(b)). The superior crystal quality of the epitaxially grown GZO films on Al_2O_3 substrates compared to the polycrystalline GZO films on glass substrates afforded better electrical characteristics.

Clatot et al. measured the film crystallinity and stoichiometry, resistivity, and transmittance curves of Si-doped ZnO thin films deposited both on glass and PET substrates. Their results confirmed the strong dependence of the electrical and optical properties on substrate nature [46]. As the theoretical and experimental studies of the impact of hydroxylation, vacancies, interstitials, and extrinsic doping on the electronic properties of the polar ZnO (0002) surface done by Li et al. [38], we can have a study on the influence of substrate type on growth, defects, and the electronic properties of the ZnO thin films.

4.3. Growth Temperature. At high temperature, films exhibited higher doping efficiency, higher carrier concentration, lower resistivity, and higher Hall mobility. Lee et al. [43] investigated the temperature dependence of electrical resistivity and optical band gap of GZO thin films. The resistivity of films decreases from 9.61×10^{-3} to 4.50×10^{-4} Ω·cm with the increases of deposition temperature from 100 to 500°C (Figure 8), and this can be attributed to substitutional doping increase and the grain boundary density decrease as the growth temperature rose.

Low growth temperature is required for the flexible substrates in OLEDs. However, the films always show poor properties at low growth temperature. This relationship does not mean all hope for low-temperature growth lost. In recent years, the growth of high quality films at low temperature on flexible substrates has attracted extensive attention owing to the rather low cost with many unique applications [51, 52]. Clatot et al. successfully deposited Si-doped zinc oxide (SZO, Si 3%) thin films at a relatively low temperature (≤150°C) by pulsed laser deposition (PLD). The SZO films deposited on PET substrates at 100°C exhibit a very promising resistivity of 9.0×10^{-4} Ω·cm [46]. Reference [44, 53] introduced a process combining room-temperature PLD and direct pulsed laser recrystallization (DPLR). During DPLR, the AZO thin film undergoes recrystallization and growth while the underlying flexible substrate is retained at low temperature. Schematic of DPLR technique and temperature evolution of AZO film on different substrates carried out by multiphysics EM-HT simulation is shown in Figures 9(a) and 9(b), respectively. Recrystallization and growth of films reduce internal imperfections, resulting in higher conductivity, Hall mobility (increases from 6.56 to 10.12 cm^2/Vs), and higher transmittance. It is also worthy to note that the merit of no damaging on the underlying substrates makes this technology promising in various low temperature applications.

4.4. Ambient Atmosphere. In deposit technique, ablated species will loss kinetic energy due to collisions with the background gas molecules, resulting in different film density and morphology. Gas pressure, especially oxygen partial pressure, has received a lot of attention [24, 25]. Gondoni et al. [35] found that when the background gas (O_2) pressure changed from 0.01 Pa to 10 Pa, resistivity remains the same and increases to a magnitude of 10^{-1} Ω·cm upon reaching 10 Pa abruptly (black squares in Figure 10). The increasing resistivity at higher pressures derived from a lower concentration of oxygen vacancy, which reduces the number of free electrons in turn. In addition, the annealing treatment in air was observed to cause resistivity to increase (red dots in Figure 10), diminishing residual dependence on deposition conditions because oxygen vacancies are saturated. This variation relation has been also observed in other preparation methods [5, 54].

In CVD processing, the precursor pressure in CVD processing also showed strong influence on resistivity. Kim et al. [24] prepared AZO layers on glass substrates by LP-CVD and found Al precursor, (Trimethylaluminum) showed strong influence on Al contents and resistivity of AZO.

4.5. Film Thickness. Film thickness is another factor for the electrical and optical properties in ZnO-based TCO films,

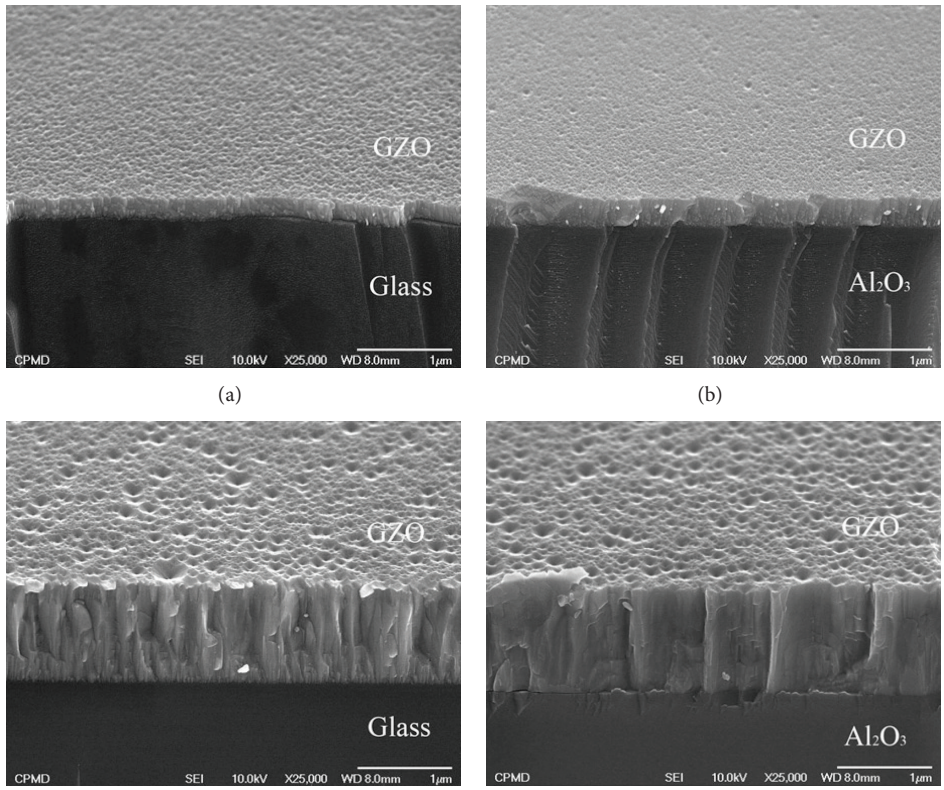

Figure 7: Cross-sectional FE-SEM images of (a) 200 nm thick GZO thin films on glass; (b) 200 nm-thick GZO thin films on Al_2O_3 (0001) substrates; (c) 1000 nm thick GZO thin films on glass; (d) 1000 nm thick GZO thin films on Al_2O_3 (0001) substrates [42]. Copyright 2009 Materials Research Society.

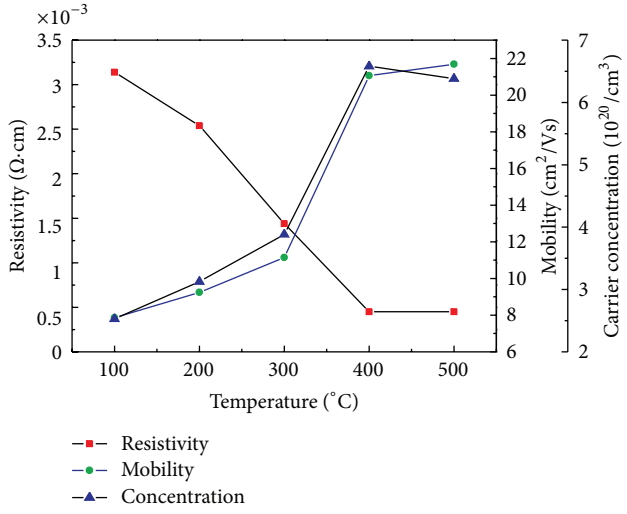

Figure 8: Resistivity, carrier concentration, and Hall mobility of GZO thin films as a function of deposition temperature in the range of RT to 500°C [43]. Copyright 2011, Elsevier.

which change from ~50 nm to ~2000 nm. In magnetron sputtering and other deposition technique, ZnO films with various thicknesses are obtained by varying the deposition time, temperature, and power [42, 55]. In sol-gel spin coating, films with various thicknesses are obtained with different repeating times of coating procedure [26, 45, 56].

As we all know that electrical conductivity becomes better while transmittance may become poorer as the film thickness increases [55]. Shin et al. [42] investigated the effect of film thickness on the structural and electrical properties of Ga-doped ZnO thin films. It was also found that the electrical resistivity difference between the films on the two substrates decreased from $9.48 \times 10^{-4}\,\Omega\cdot\text{cm}$ to $1.45 \times 10^{-4}\,\Omega\cdot\text{cm}$ with increasing the film thickness from 100 nm to 1000 nm. In Figure 7, the conductivity increases because of both the increase of grain size and the decrease of grain boundary scattering. On the other hand, more photons are adsorbed when the thickness increases according to the following:

$$I = I_0 e^{-\alpha x}. \tag{2}$$

Here I is the intensity of transmitted light, I_0 is the intensity of incident light, α is absorption coefficient, and x can be treated as the film thickness. Due to these two opposite trends, it is difficult to balance the need for high conductivity with the need for high transparency. How to get thinner films with both excellent electrical and optical property is one of the main research tasks.

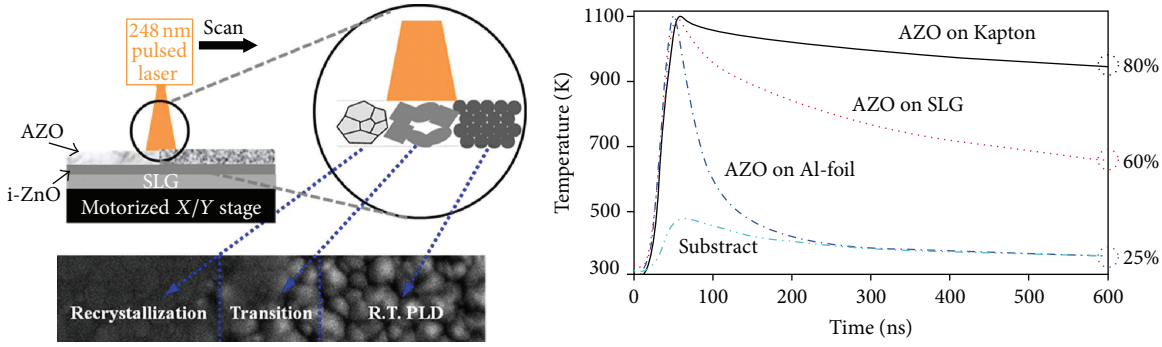

FIGURE 9: (a) Schematic of DPLR technique. (b) Temperature evolution of AZO film on different substrates carried out by multiphysics EM-HT simulation. To reach 1100 K (peak temperature), laser fluence used is 50, 60, and 65 mJ/cm^2 for AZO film on Kapton, SLG, and Al-foil substrates, respectively [44]. Copyright 2012 American Institute of Physics.

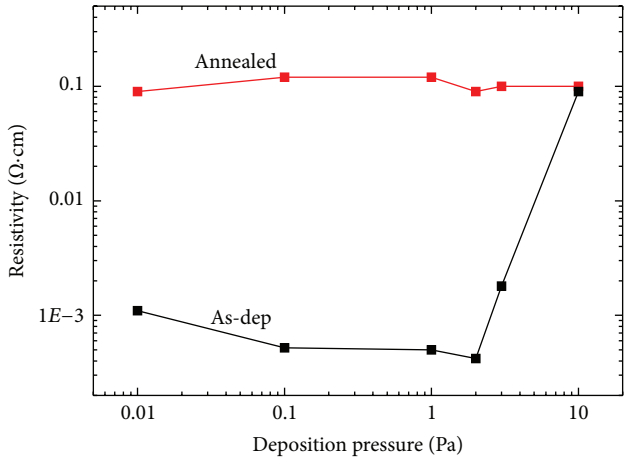

FIGURE 10: Resistivity as a function of deposition pressure for as-deposited (black squares) and annealed films (red dots) [35]. Copyright 2012, Elsevier.

5. Summary

In this paper, how dopants and growth conditions, such as substrate type, growth temperature, influence electrical and optical properties of ZnO-based TCO films were discussed in a panoramic view. we reviewed recently published work on new, cheap, low-temperature, and high-speed deposition technology, highlighting methods of producing film on flexible substrate, the most promising and rapidly emerging research areas. However, more experimental works are needed to clarify the relationship between doping, processing, and property of ZnO thin films.

Acknowledgments

This work was supported by the Natural Science Foundation of China (Nos. 61222403), the Jiangsu Introduction Program of High-Level Innovative and Pioneering Talents, the Fundamental Research Funds for the Central Universities (Nos. 4015-56XIA12004 and 4015-56YAH11047), and by the Opened Fund of the State Key Laboratory on Integrated Optoelectronics No. 20********.

References

[1] J. Song, Y. He, J. Chen et al., "Bicolor light-emitting diode based on zinc oxide nanorod arrays and poly(2-methoxy,5-octoxy)-1,4-phenylenevinylene," *Journal of Electronic Materials*, vol. 41, no. 3, pp. 431–436, 2012.

[2] D. J. Rogers, F. H. Teherani, V. E. Sandana, and M. Razeghi, "ZnO thin films and nanostructures for emerging optoelectronic applications," in *Proceedings of the 12th Optoelectronic Integrated Circuits*, L. A. Eldada and E. H. Lee, Eds., January 2010.

[3] H. Zeng, X. Xu, Y. Bando et al., "Template deformation-tailored ZnO nanorod/nanowire arrays: full growth control and optimization of field-emission," *Advanced Functional Materials*, vol. 19, no. 19, pp. 3165–3172, 2009.

[4] T. Minami, "Transparent conducting oxide semiconductors for transparent electrodes," *Semiconductor Science and Technology*, vol. 20, no. 4, pp. S35–S44, 2005.

[5] D. B. Buchholz, J. Liu, T. J. Marks, M. Zhang, and R. P. H. Chang, "Control and characterization of the structural, electrical, and optical properties of amorphous zinc-indium-tin oxide thin films," *ACS Applied Materials & Interfaces*, vol. 1, no. 10, pp. 2147–2153, 2009.

[6] C. A. Hoel, T. O. Mason, J. F. Gaillard, and K. R. Poeppelmeier, "Transparent conducting oxides in the ZnO-In2O 3-SnO2 system," *Chemistry of Materials*, vol. 22, no. 12, pp. 3569–3579, 2010.

[7] A. Stadler, "Transparent conducting oxides-an up-to-date overview," *Materials*, vol. 5, no. 4, pp. 661–683, 2012.

[8] C. G. Granqvist, "Transparent conductors as solar energy materials: a panoramic review," *Solar Energy Materials and Solar Cells*, vol. 91, no. 17, pp. 1529–1598, 2007.

[9] U.S.G. Survey, "Mineral Commodity Summaries," 2012.

[10] K. Ellmer, "Past achievements and future challenges in the development of optically transparent electrodes," *Nature Photonics*, vol. 6, no. 12, pp. 809–817, 2012.

[11] T. Minami, "Substitution of transparent conducting oxide thin films for indium tin oxide transparent electrode applications," *Thin Solid Films*, vol. 516, no. 7, pp. 1314–1321, 2008.

[12] T. W. Kim, D. C. Choo, Y. S. No, W. K. Choi, and E. H. Choi, "High work function of Al-doped zinc-oxide thin films as transparent conductive anodes in organic light-emitting devices," *Applied Surface Science*, vol. 253, no. 4, pp. 1917–1920, 2006.

[13] T. Minami, "Present status of transparent conducting oxide thin-film development for Indium-Tin-Oxide (ITO) substitutes," *Thin Solid Films*, vol. 516, no. 17, pp. 5822–5828, 2008.

[14] H. Zeng, S. Yang, and W. Cai, "Reshaping formation and luminescence evolution of ZnO quantum dots by laser-induced fragmentation in liquid," *Journal of Physical Chemistry C*, vol. 115, no. 12, pp. 5038–5043, 2011.

[15] H. B. Zeng, X.-W. Du, S. C. Singh, S. A. Kulinich, S. Yang, and J. He, "Nanomaterials via laser ablation/irradiation in liquid: a review," *Advanced Functional Materials*, vol. 22, no. 7, pp. 1333–1353, 2012.

[16] A. Favier, D. Muñoz, S. Martín De Nicolás, and P. J. Ribeyron, "Boron-doped zinc oxide layers grown by metal-organic CVD for silicon heterojunction solar cells applications," *Solar Energy Materials and Solar Cells*, vol. 95, no. 4, pp. 1057–1061, 2011.

[17] Q. Huang, Y. Wang, S. Wang, D. Zhang, Y. Zhao, and X. Zhang, "Transparent conductive ZnO:B films deposited by magnetron sputtering," *Thin Solid Films*, vol. 520, no. 18, pp. 5960–5964, 2012.

[18] J. A. Sans, J. F. Sánchez-Royo, A. Segura, G. Tobias, and E. Canadell, "Chemical effects on the optical band-gap of heavily doped ZnO: MIII (M=Al,Ga,In): an investigation by means of photoelectron spectroscopy, optical measurements under pressure, and band structure calculations," *Physical Review B*, vol. 79, no. 19, Article ID 195105, 2009.

[19] D. S. Bhachu, I. P. Parkin, and G. Sankar, "Aerosol assisted chemical vapour deposition of transparent conductive Zinc oxide films," *Chemistry of Materials*, vol. 24, no. 24, pp. 4704–4710, 2012.

[20] P. Nunes, E. Fortunato, P. Tonello, F. Braz Fernandes, P. Vilarinho, and R. Martins, "Effect of different dopant elements on the properties of ZnO thin films," *Vacuum*, vol. 64, no. 3-4, pp. 281–285, 2002.

[21] J. L. Zhao, X. W. Sun, H. Ryu, and Y. B. Moon, "Thermally stable transparent conducting and highly infrared reflective Ga-doped ZnO thin films by metal organic chemical vapor deposition," *Optical Materials*, vol. 33, no. 6, pp. 768–772, 2011.

[22] S. M. Park, T. Ikegami, and K. Ebihara, "Effects of substrate temperature on the properties of Ga-doped ZnO by pulsed laser deposition," *Thin Solid Films*, vol. 513, no. 1-2, pp. 90–94, 2006.

[23] Y. Geng, L. Guo, S. S. Xu et al., "Influence of Al doping on the properties of ZnO thin films grown by atomic layer deposition," *Journal of Physical Chemistry C*, vol. 115, no. 25, pp. 12317–12321, 2011.

[24] D. Kim, H. Kim, K. Jang, S. Park, K. Pillai, and J. Yi, "Electrical and optical properties of low pressure chemical vapor deposited Al-doped ZnO transparent conductive oxide for thin film solar cell," *Journal of the Electrochemical Society*, vol. 158, no. 4, pp. D191–D195, 2011.

[25] L. Cao, L. Zhu, J. Jiang, R. Zhao, Z. Ye, and B. Zhao, "Highly transparent and conducting fluorine-doped ZnO thin films prepared by pulsed laser deposition," *Solar Energy Materials and Solar Cells*, vol. 95, no. 3, pp. 894–898, 2011.

[26] T. Wang, Y. Liu, Q. Fang, M. Wu, X. Sun, and F. Lu, "Low temperature synthesis wide optical band gap Al and (Al, Na) co-doped ZnO thin films," *Applied Surface Science*, vol. 257, no. 6, pp. 2341–2345, 2011.

[27] D.-W. Kang, J.-Y. Kwon, D.-J. Lee, and M.-K. Han, "Boron and aluminum codoped ZnO transparent conducting films with high electrical stability," *Journal of the Electrochemical Society*, vol. 159, no. 2, p. H61, 2012.

[28] S. W. Shin, G. L. Agawane, I. Y. Kim et al., "Development of transparent conductive Mg and Ga co-doped ZnO thin films: effect of Mg concentration," *Surface and Coatings Technology*, 2012.

[29] S. W. Shin, I. Y. Kim, G. H. Lee et al., "Design and growth of quaternary Mg and Ga codoped ZnO thin films with transparent conductive characteristics," *Crystal Growth & Design*, vol. 11, no. 11, pp. 4819–4824, 2011.

[30] H. Zeng, W. Cai, P. Liu et al., "ZnO-based hollow nanoparticles by selective etching: elimination and reconstruction of metal—semiconductor interface, improvement of blue emission and photocatalysis," *ACS Nano*, vol. 2, no. 8, pp. 1661–1670, 2008.

[31] D. P. Norton, Y. W. Heo, M. P. Ivill et al., "ZnO: growth, doping & processing," *Materials Today*, vol. 7, no. 6, pp. 34–40, 2004.

[32] H. Zeng, W. Cai, J. Hu, G. Duan, P. Liu, and Y. Li, "Violet photoluminescence from shell layer of Zn/ZnO core-shell nanoparticles induced by laser ablation," *Applied Physics Letters*, vol. 88, no. 17, Article ID 171910, 2006.

[33] H. Zeng, G. Duan, Y. Li, S. Yang, X. Xu, and W. Cai, "Blue luminescence of ZnO nanoparticles based on non-equilibrium processes: defect origins and emission controls," *Advanced Functional Materials*, vol. 20, no. 4, pp. 561–572, 2010.

[34] J. G. Lu, S. Fujita, T. Kawaharamura et al., "Carrier concentration dependence of band gap shift in n -type ZnO:Al films," *Journal of Applied Physics*, vol. 101, no. 8, Article ID 083705, 2007.

[35] P. Gondoni, M. Ghidelli, F. Di Fonzo et al., "Structural and functional properties of Al:ZnO thin films grown by Pulsed Laser Deposition at room temperature," *Thin Solid Films*, vol. 520, no. 14, pp. 4707–4711, 2012.

[36] G. Socol, D. Craciun, I. N. Mihailescu et al., "High quality amorphous indium zinc oxide thin films synthesized by pulsed laser deposition," *Thin Solid Films*, vol. 520, no. 4, pp. 1274–1277, 2011.

[37] A. K. Das, P. Misra, and L. M. Kukreja, "Effect of Si doping on electrical and optical properties of ZnO thin films grown by sequential pulsed laser deposition," *Journal of Physics D*, vol. 42, no. 16, Article ID 165405, 2009.

[38] H. Li, L. K. Schirra, J. Shim et al., "Zinc oxide as a model transparent conducting oxide: a theoretical and experimental study of the impact of hydroxylation, bacancies, interstitials, and extrinsic doping on the electronic properties of the polar ZnO (0002) surface," *Chemistry of Materials*, vol. 24, no. 15, pp. 3044–3055, 2012.

[39] H. Agura, A. Suzuki, T. Matsushita, T. Aoki, and M. Okuda, "Low resistivity transparent conducting Al-doped ZnO films prepared by pulsed laser deposition," *Thin Solid Films*, vol. 445, no. 2, pp. 263–267, 2003.

[40] A. Illiberi, B. Kniknie, J. van Deelen et al., "Industrial high-rate (~14 nm/s) deposition of low resistive and transparent ZnOx:Al films on glass," *Solar Energy Materials and Solar Cells*, vol. 95, no. 7, pp. 1955–1959, 2011.

[41] A. Illiberi, P. J. P. M. Simons, B. Kniknie et al., "Growth of ZnOx:Al by high-throughput CVD at atmospheric pressure," *Journal of Crystal Growth*, vol. 347, no. 1, pp. 56–61, 2012.

[42] S. W. Shin, S. M. Pawar, T. W. Kim, J. H. Moon, and J. H. Kim, "Effect of film thickness on the structural and electrical properties of Ga-dopped ZnO thin films prepared on glass and

Al2O3 (0001) substrates by RF magnetron sputtering method," *Journal of Materials Research*, vol. 24, no. 2, pp. 441–447, 2009.

[43] D.-H. Lee, K. Kim, Y. S. Chun, S. Kim, and S. Y. Lee, "Substitution mechanism of Ga for Zn site depending on deposition temperature for transparent conducting oxides," *Current Applied Physics*, vol. 12, no. 6, pp. 1586–1590, 2012.

[44] M. Y. Zhang, Q. Nian, and G. J. Cheng, "Room temperature deposition of alumina-doped zinc oxide on flexible substrates by direct pulsed laser recrystallization," *Applied Physics Letters*, vol. 100, no. 15, 2012.

[45] L. Luo, M. D. Rossell, D. Xie, R. Erni, and M. Niederberger, "Microwave-assisted nonaqueous Sol-Gel synthesis: from Al:ZnO nanoparticles to transparent conducting films," *ACS Sustainable Chemistry & Engineering*, vol. 1, no. 1, pp. 152–160, 2013.

[46] J. Clatot, G. Campet, A. Zeinert, C. Labrugère, M. Nistor, and A. Rougier, "Low temperature Si doped ZnO thin films for transparent conducting oxides," *Solar Energy Materials and Solar Cells*, vol. 95, no. 8, pp. 2357–2362, 2011.

[47] L. Gong, J. Lu, and Z. Ye, "Transparent and conductive Ga-doped ZnO films grown by RF magnetron sputtering on polycarbonate substrates," *Solar Energy Materials and Solar Cells*, vol. 94, no. 6, pp. 937–941, 2010.

[48] L. Ficke and M. Cahay, "The bright future of organic LEDs," *IEEE Potentials*, vol. 22, no. 5, pp. 31–34, 2003.

[49] J. Z. Song, Y. He, D. Zhu, J. Chen, C. L. Pei, and J. A. Wang, "Polymer/ZnO micro-nano array composites for light-emitting layer of flexible optoelectronic devices," *Acta Physico-Chimica Sinica*, vol. 27, no. 5, pp. 1207–1213, 2011.

[50] S. Esmaili-Sardari, A. Berkovich, and A. A. Iliadis, "Observation of conductivity type conversion in undoped ZnO films grown by pulsed laser deposition on silicon (100) substrates," *Applied Physics Letters*, vol. 100, no. 5, Article ID 053505, 2012.

[51] K. Kim, S. Y. Park, K.-H. Lim, C. Shin, J.-M. Myoung, and Y. S. Kim, "Low temperature and solution-processed Na-doped zinc oxide transparent thin film transistors with reliable electrical performance using methanol developing and surface engineering," *Journal of Materials Chemistry*, vol. 22, no. 43, pp. 23120–23128, 2012.

[52] W.-J. Yang, C.-C. Tsao, C.-Y. Hsu, H.-C. Chang, C.-P. Chou, and J.-Y. Kao, "Fabrication and characterization of transparent conductive ZnO:Al thin films deposited on polyethylene terephthalate substrates," *Journal of the American Ceramic Society*, vol. 95, no. 7, pp. 2140–2147, 2012.

[53] M. Y. Zhang and G. J. Cheng, "Highly conductive and transparent alumina-doped ZnO films processed by direct pulsed laser recrystallization at room temperature," *Applied Physics Letters*, vol. 99, no. 5, 2011.

[54] T. Moon, W. Yoon, K. S. Ji et al., "Enhancement of crystallinity in ZnO:Al films using a two-step process involving the control of the oxygen pressure," in *Proceedings of the 35th IEEE Photovoltaic Specialists Conference (PVSC '10)*, pp. 3709–3712, June 2010.

[55] T. Prasada Rao and M. C. Santhoshkumar, "Effect of thickness on structural, optical and electrical properties of nanostructured ZnO thin films by spray pyrolysis," *Applied Surface Science*, vol. 255, no. 8, pp. 4579–4584, 2009.

[56] J. Z. Song, Y. He, Z. D. Pan, D. Zhu, J. Chen, and J. A. Wang, "PANI/nano-ZnO composites prepared by in-situ polymerization under magnetic field," *Acta Chimica Sinica*, vol. 69, no. 13, pp. 1582–1588, 2011.

Hindawi Publishing Corporation
Journal of Nanomaterials
Volume 2013, Article ID 263852, 7 pages
http://dx.doi.org/10.1155/2013/263852

Research Article

Methanol-Sensing Property Improvement of Mesostructured Zinc Oxide Prepared by the Nanocasting Strategy

Qian Gao,[1] Wei-Tao Zheng,[1] Cun-Di Wei,[1] and Hui-Ming Lin[2]

[1] *College of Material Science and Engineering, Jilin University, Changchun 130022, China*
[2] *Key Laboratory of Semiconductor Nanocomposite Materials of Ministry of Education, College of Chemistry and Chemical Engineering, Harbin Normal University, Harbin 150025, China*

Correspondence should be addressed to Qian Gao; gaoqian@jlu.edu.cn and Hui-Ming Lin; hiuminglin@gmail.com

Received 20 December 2012; Accepted 9 January 2013

Academic Editor: Xiang Wu

The specific structure and morphology often play a critical role in governing the excellent intrinsic properties of the compound semiconductor. Herein, mesostructured ZnO with excellent methanol-sensing properties was prepared by a structure replication procedure through the incipient wetness technique. The investigation on the crystal structure and morphology of the resultant material shows that the product consists of hexagonally arranged mesopores and crystalline walls, and its structure is an ideal replication of CMK-3 template. Consequently, mesostructured ZnO was fabricated as a gas sensor for methanol. The excellent methanol-sensing performance was achieved at a relatively low operating temperature of 120°C. In comparison with the nonporous ZnO prepared through conventional coprecipitation approach, mesostructured ZnO material shows the higher sensitivity and stability. Furthermore, it shows the discrimination between methanol and ethanol sensitivity, which makes it a good candidate in fabricating selective methanol sensor in practice.

1. Introduction

Zinc oxide has been widely investigated because of the hopes it raises for a wide range of technological applications such as catalysts [1, 2], transparent conductors [3], field-emission devices [4], optoelectronic devices [5–7], and also for its fundamental scientific significance. However, besides its excellent intrinsic properties, the structure-activity relationship plays quite an important role in most of its numerous applications [8, 9].

As one important application, semiconducting zinc oxide is a promising material for sensing various gases [10–15]. Since semiconductor gas sensors are based on surface-chemical interaction between the gas molecules and the crystalline materials [14, 16]. With large surface-to-volume ratios and well-defined pore structures, mesostructured metal oxides are particularly desired for improving sensing performance [17–19]. As we known, it is difficult to prepare mesostructured metal oxides by directing soft-template method. The hard template method makes it possible to synthesize mesostructured metal oxides with excellent gas-sensing properties [20–22]. At present, many mesostructured metal oxides have been obtained by the utilization of nanoporous silica as matrices, including In_2O_3 [18, 23], Fe_2O_3 [24], Co_3O_4 [25, 26], and Cr_2O_3 [26]. However, it is impossible to get ZnO mesostructures by nanocasting of mesoporous silica, because ZnO is an amphoteric oxide, and its structure will be destroyed in both acidic and alkali solution during the removal of the hard template. Although mesoporous carbon instead of silica could be used as structure matrix, the hydrophobic character of the carbon template is incompatible with the aqueous precursor solution. For the difficulty in obtaining ZnO with highly ordered mesostructures, the synthesis of ordered mesoporous ZnO through nanocasting was not reported until 2007 [27]. For this reason, to the best of our knowledge, few investigations on the sensing properties of ordered mesoporous ZnO have been reported [28].

In this research, the methanol-sensing properties of ordered mesoporous ZnO were investigated. As we known,

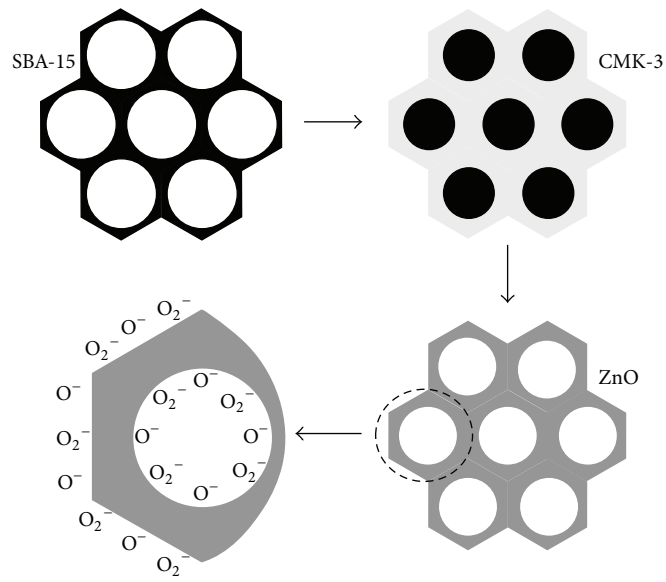

Figure 1: The nanocasting procedure for mesostructured ZnO synthesis.

methanol is a kind of widely used organic solvent with a broad application in power sources and the manufacturing of dyes, drugs, perfumes, and so forth. However, it is highly toxic and is often fatal to humans [29]. Thus, it is imperative to develop highly selective sensor for the detection of methanol. Herein, we present the synthesis of ZnO with ordered mesostructure for methanol sensor. The methanol-sensing test reveals that the sensor fabricated from mesostructured zinc oxide exhibits high sensitivity and selectivity towards methanol at a relatively low working temperature of 120°C, which is much better than that of the corresponding nonporous materials synthesized by conventional approach.

Furthermore, in contrast to the reported ZnO materials which are applied as ethanol sensors [10, 13, 30, 31], this mesostructured ZnO material with uniform mesoporous structure shows higher response to methanol than ethanol without doping any additive and promoter. The discrimination between methanol and ethanol sensitivity makes it a good candidate in fabricating highly selective sensors in practice.

2. Experiment Process

2.1. Synthesis of Mesostructured ZnO Materials. The synthesis strategy is illustrated in Figure 1. SBA-15 was synthesized following the literature procedure reported by Zhao et al. [32]. A solution with 1.2 g of Pluronic P123 triblock copolymer, 30 g distilled H_2O, and 6 mL of concentrated HCl (35%) was prepared and stirred for 2 h, and 5.4 mL of tetraethyl orthosilicate (TEOS) was added to the solution and stirred vigorously for 8 min. Then the mixture was heated at 40°C for 24 h and 100°C for 48 h as a hydrothermal treatment. The solid product was filtered, washed, dried at room temperature, and calcined at 550°C for 6 h. CMK-3 was prepared according to a literature procedure [33]; the silica matrix was removed by stirring in a 5% HF solution. Mesostructured ZnO was prepared by incipient wetness impregnation of mesoporous CMK-3 carbon with zinc nitrate. To obtain a good infusion and filling of the zinc precursor into CMK-3 mesopores, a saturated ethanol solution of zinc nitrate was chosen as the precursor instead of aqueous solution. Using ethanol as a solvent can not only improve the wettability of CMK-3 but also facilitate the uniform loading of zinc nitrate into pores. The amount of the solution used in incipient wetness impregnation equals to the pore volume of the support. In order to convert zinc nitrate to zinc oxide, the sample was heated under an atmosphere of air to 300°C at a temperature ramp rate of 2°C min^{-1}. The procedure was repeated twice, and the final product was obtained after heating in air at 700°C for 2 hrs.

For comparison, non-porous ZnO was synthesized as follows: $Zn(NO_3)_2{\cdot}6H_2O$ was dissolved in water to obtain a 0.1 M solution, and then 0.2 M urea aqueous solution was added to it. The mixture was gradually heated to 90°C with stirring until the emergence of a large amount of white precipitation. After washing and filtering, the precipitate was dried at 60°C, followed by calcination at 500°C.

2.2. Fabrication of Mesostructured ZnO Gas Sensor. For the preparation of the sensors, the as-synthesized product was mixed with deionized water to form a paste. Then the paste was coated on a ceramic tube on which a pair of Au electrodes was previously assembled. Pt wires attaching to these electrodes were used as electrodes. A Ni-Cr alloy wire was placed through the tube as a heater to provide the operating temperature. Figures 2(a) and 2(b) show a schematic image of the sensor element and a photograph of the as-fabricated sensor on a socket, respectively.

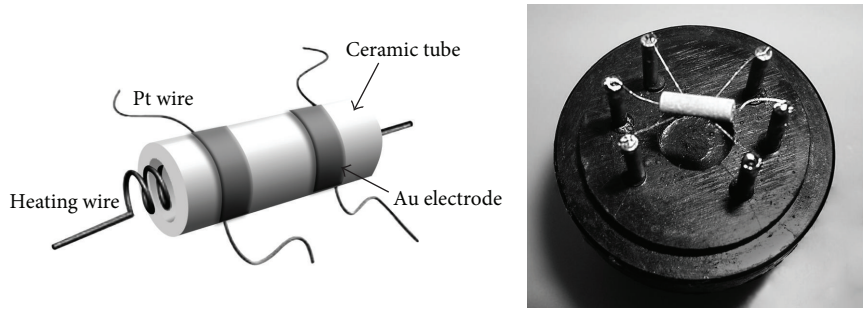

(a) (b)

Figure 2: (a) Schematic image of the sensor element and (b) photograph of the as-fabricated sensor on a socket.

2.3. Characterization of Structure and Gas-Sensing Property. The structure of the product was investigated using an X-ray diffractometer (XRD) (Siemens D5005 diffractometer) with Cu-K_α radiation at 40 kV and 30 mA. The TEM image was taken on a HITACHI H-600 transmission electron microscopic operating at an accelerating voltage of 100 kV. Nitrogen adsorption/desorption was measured with a Micromeritics ASAP 2010 M sorptometer.

Gas sensing properties were studied in a static test system. After injecting the saturated target vapour into a test chamber (about 1 L in volume), the sensor was arranged into the chamber. The resistance of the sensor was monitored by a measuring system, RQ-2 intelligent test meter (Qingdao, China). The gas sensitivity was defined as R_a/R_g, where R_a is the resistance of the sensor in air, and R_g is that in the detecting gas.

3. Results and Discussion

3.1. Characteristic of Sensing Material. In order to get the ordered mesostructured zinc oxide materials, CMK-3 and an organic solution of zinc nitrate were used as host matrix and precursor, respectively. The mesostructure of ZnO is formed by replicating the structure of CMK-3 template through the incipient wetness impregnation. As the interaction between the active precursor in solution and the CMK-3 carbon is weak, relatively high loading of precursor could be achieved by the method of incipient wetness impregnation which is more convenient, economical, and time saving than the traditional impregnation method [34]. Figure 3(a) presents the low-angle X-ray diffraction (XRD) patterns of the mesostructured ZnO sample, together with that of CMK-3 which was used as the template. The low-angle pattern of the resultant ZnO material clearly shows the characteristic diffraction, indicating that the mesoporous structure is formed. The XRD pattern of CMK-3 exhibits three characteristic peaks which are assigned to (100), (110), and (200) diffractions of the two-dimensional hexagonal p6 mm symmetry of the ordered pore system. The diffraction peak of mesostructured ZnO located at the same position as the carbon template further confirms that the hexagonal symmetry is preserved in the replication process, although a certain degree of broadening and a poorer resolution of the diffraction imply some loss in structural ordered degree.

The wide-angle powder XRD pattern of mesostructured ZnO is shown in Figure 3(b). The resultant mesostructured ZnO sample exhibits well-resolved characteristic diffraction peaks which are in accordance with the hexagonal wurtzite-type crystalline phase (JCPDS card number 79-0205). The well crystalline nature confirms the presence of crystalline framework walls in mesostructured zinc oxide.

Moreover, the structure of the resultant material is also verified by transmission electron microscopy (Figure 4). The TEM image viewed perpendicular to the direction of the hexagonal pore arrangement indicates that the structure of ZnO is an inverse replica of the carbon template. This replica is composed of a hexagonally packed nanoparticle array. Because of the confined growth in the channels of the mesoporous carbon template, the nanoparticles are rather uniform in diameter and oriented in the mesostructured framework. Upon removing the template, these nanoparticles interacted and constructed the mesoporous structure. Nitrogen physisorption reveals a mean pore diameter of 5.7 nm, a specific surface area of 47 $m^2\,g^{-1}$, and total pore volume of 0.21 $cm^3\,g^{-1}$, while the specific surface area of nonporous ZnO used for contrast is only 13 $m^2\,g^{-1}$.

3.2. Gas-Sensing Properties

3.2.1. Optimum Operating Temperature Property. Gas-sensing experiments were performed at different temperatures to find out the optimum operating condition for methanol detection. The optimum operating temperature is not only related to the intrinsic property of sensing material itself, but also related to the sensing process of the gas towards the surface of materials. The sensor fabricated from mesostructured zinc oxide was exposed to 50 ppm methanol at different working temperatures to get the optimum condition. The relationship between the sensitivity and the working temperature is shown in Figure 5. It is seen that the value of the sensitivity increased quickly with the elevated working temperature until reached the maximum at 120°C, and subsequently, it decreased rapidly with further elevated working temperature. Accordingly, a relatively low

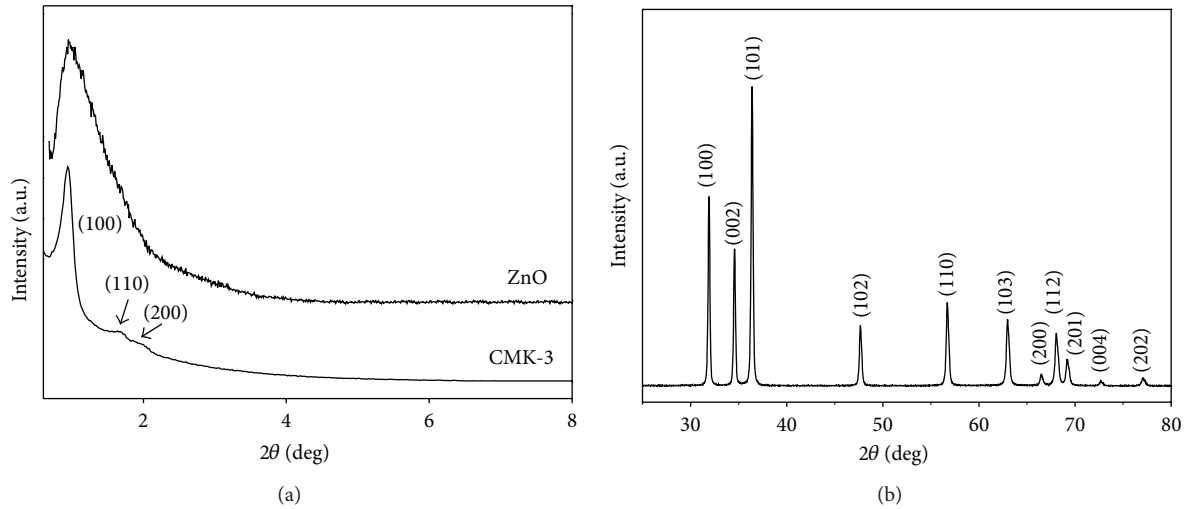

Figure 3: (a) Low-angle XRD patterns of mesostructured ZnO and CMK-3 which was used as the structure matrix and (b) wide-angle XRD pattern of mesostructured ZnO.

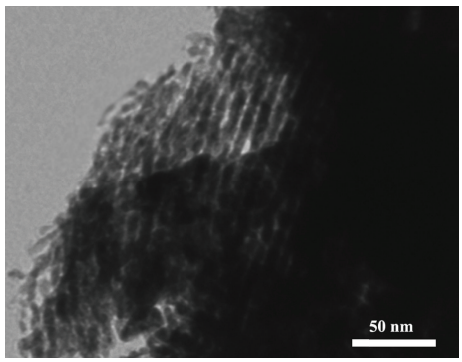

Figure 4: TEM image of the mesostructured ZnO prepared by a structure replication procedure.

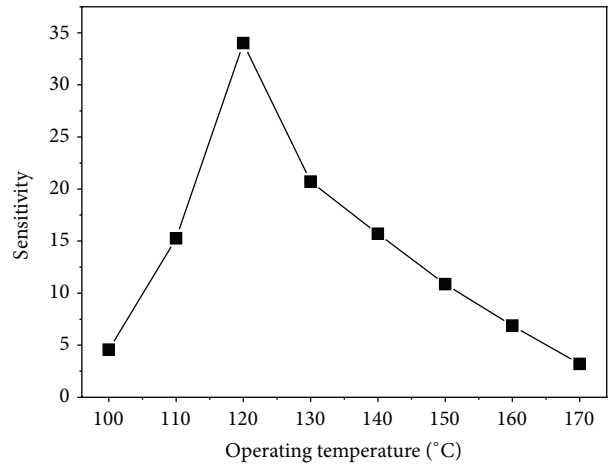

Figure 5: The operating temperature dependence of the sensitivity of mesostructured ZnO sensor to 50 ppm methanol.

operating temperature of 120°C is identified as the optimal working temperature and applied to all the gas-sensing measurements hereinafter.

3.2.2. Gas Response Property. As shown in Figure 6(a), the sensitivity of mesostructured ZnO versus methanol of different concentrations (5–1000 ppm) was measured. The sensor exhibits not only a high sensitivity to methanol, but also a good dependence on the concentration of methanol. In the low concentration range of 5–300 ppm in Figure 6(b), the sensitivity is linear and proportional to the methanol concentration. The liner equation is $S = 0.755C - 2.184$, in which S represents the gas sensitivity, and C represents the methanol concentration. It is indicated that mesostructured zinc oxide is suitable for the detection of methanol at low concentrations. When gas response of the as-prepared gas sensor presents a linear or quasilinear relationship with the concentration of the measured gas, it means that the sensor can be used in the online monitoring of target gas. Moreover, for comparison, the sensitivity of non-porous ZnO versus methanol gas of different concentrations is also recorded and shown in Figure 6. The sensitivity of non-porous ZnO to methanol is significantly lower than that of mesostructured ZnO under the same conditions. We assume that the higher methanol-sensing property of mesostructured ZnO is related to the ordered porous structure and the rigid structure matrix.

3.2.3. The Selectivity Property. The selectivity of mesostructured ZnO is investigated by exposure to 50 ppm different gases (C_2H_5OH, CH_3OH, CO, C_6H_6, HCHO, NH_3, and H_2O) (Figure 7). Obviously, mesostructured ZnO exhibits good sensitivity and high selectivity to methanol vapour compared with other gases. Remarkably, the sensitivity of mesostructured ZnO towards methanol is approximately 3.5 times higher than towards ethanol. It is presumed that

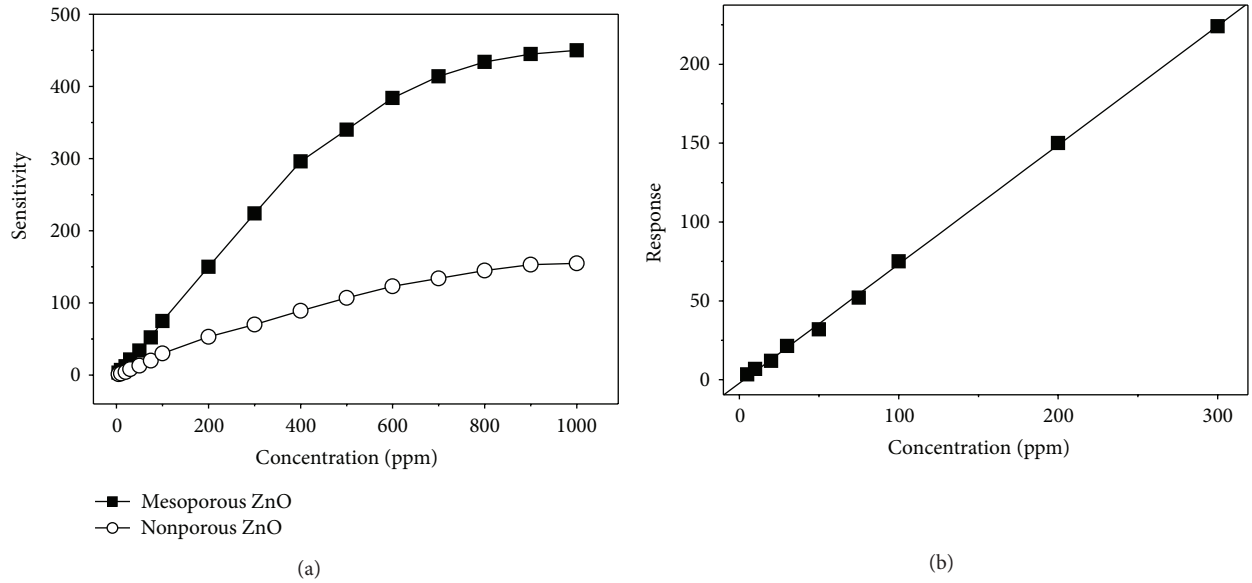

Figure 6: (a) The sensitivity of mesostructured ZnO sensor versus methanol concentration (5–1000 ppm) and (b) the calibration curve in the range of 5–300 ppm.

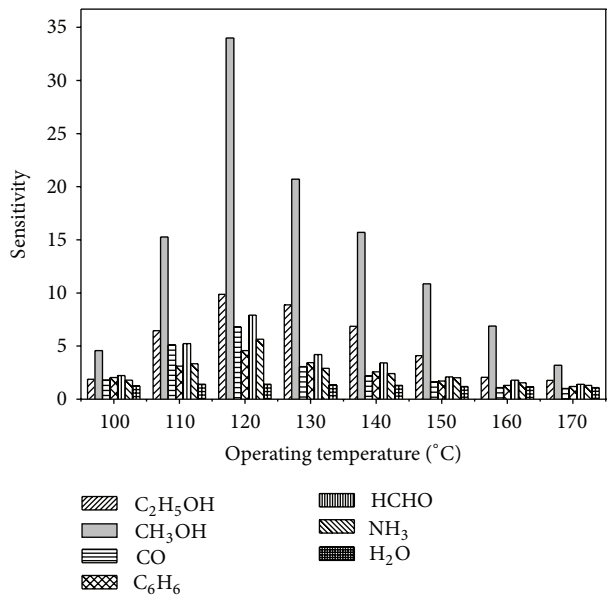

Figure 7: The sensitivity of the mesostructured ZnO sensor to 50 ppm C_2H_5OH, CH_3OH, CO, C_6H_6, HCHO, NH_3, and H_2O at different operating temperature.

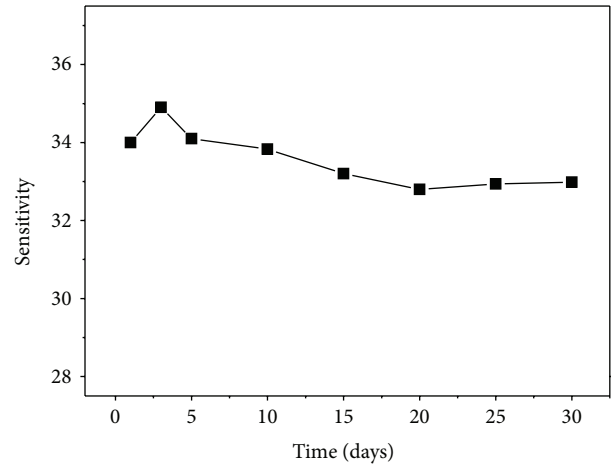

Figure 8: The long-term sensitivity values of mesostructured ZnO to 50 ppm methanol at 120°C.

the methanol molecule is more suitable for diffusion in the mesopores, as the size of methanol molecule is smaller than that of ethanol molecule. It is well known that most of the applications of zinc oxide, including many of its excellent intrinsic properties, in general, rely critically on its specific structure and morphology. So, we believed that the high selectivity of mesostructured zinc oxide without doping any additive is due to the uniform mesoporous structure.

3.2.4. Stability and Repeatability. The long-term stability of this sensor was investigated by repeating the test after aging. As shown in Figure 8, the sensor shows a nearly constant sensitivity to 50 ppm methanol during the tests, indicating that the mesostructured ZnO sensor is extremely stable for detecting methanol. The superior sensitivity and selectivity combined with the high stability render the mesoporous ZnO promising material for practical application.

3.2.5. Gas-Sensing Mechanism. For most semiconductor metal oxides, gas sensing is based on surface-chemical interaction between gas molecules and the sensing material and reflected in the variation of resistance, which is primarily caused by the adsorption and desorption of the gas molecules

on the surface of the sensor. In ambient air, the oxygen molecules are chemisorbed on the surface of ZnO to generate active oxygen species (Figure 1), such as O_2^- and O^-, which results in the formation of the surface depletion region as follows:

$$O_2\,(\text{gas}) \longleftrightarrow O_2\,(\text{ads}) \quad (1)$$

$$O_2\,(\text{ads}) + e^- \longleftrightarrow O_2^-\,(\text{ads}) \quad (2)$$

$$O_2^-\,(\text{ads}) + e^- \longleftrightarrow 2O^-\,(\text{ads}) \quad (3)$$

When the mesostructured ZnO is exposed to methanol vapour, the reaction between methanol and ionic oxygen species can take place in two possible ways [35] as follows:

$$CH_3OH + O^- \longleftrightarrow HCHO + H_2O + e^- \quad (4)$$

$$CH_3OH + O_2^- \longleftrightarrow HCOOH + H_2O + e^- \quad (5)$$

Methanol molecules are oxidized to formaldehyde or formic acid step by step, and electrons are liberated accompanying the reactions, resulting in an increase of the carrier concentration and electronic conductivity of mesostructured zinc oxide. In comparison with non-porous ZnO, mesostructured ZnO sensor exhibits superior methanol-sensing properties. The large surface-to-volume ratio and uncompacted structure are considered to facilitate the high sensitivity and favorable selectivity of the mesostructured ZnO. Owing to their well-defined structure and effective electron transport, mesostructured ZnO materials are particularly suitable for the detection of methanol.

4. Conclusions

In conclusion, uniformed mesostructured ZnO with excellent sensing performance has been synthesized through an improved structure replication technique. It is revealed that the zinc oxides exhibit uniformly crystalline pore walls which are ideal replication of the template CMK-3 carbon, while the sensing process is considered to undergo a surface-chemical interaction mechanism between the methanol molecules and ZnO surface. The ordered pore system remarkably facilitates the improvement of sensitivity and selectivity for methanol sensing in contrast to the non-porous sensing materials. And also it is worth noting that the difference of the sensitivity between methanol and ethanol makes it a good candidate in potential practice. All in all, the mesostructured ZnO is a kind of promising materials for fabricating high performance in methanol sensors.

Acknowledgments

This work was supported by the Fundamental Research Funds for the Central Universities of China, cutting-edge science and interdisciplinary innovation projects of Jilin University (201103024), the Innovation Project of Jilin University Young Teachers, Foundation of Harbin Educational Committee (12521164), and National Natural Science Foundation of China (21101046).

References

[1] M. Behrens, F. Studt, I. Kasatkin et al., "The active site of methanol synthesis over $Cu/ZnO/Al_2O_3$ industrial catalysts," *Science*, vol. 336, no. 6083, pp. 893–897, 2012.

[2] P. L. Hansen, J. B. Wagner, S. Helveg, J. R. Rostrup-Nielsen, B. S. Clausen, and H. Topsøe, "Atom-resolved imaging of dynamic shape changes in supported copper nanocrystals," *Science*, vol. 295, no. 5562, pp. 2053–2055, 2002.

[3] S. Phadke, J.-Y. Lee, J. West, and A. Salleo, "Using alignment and 2D network simulations to study charge transport through doped ZnO nanowire thin film electrodes," *Advanced Functional Materials*, vol. 21, no. 24, pp. 4691–4697, 2011.

[4] Q. Zhao, H. Z. Zhang, Y. W. Zhu et al., "Morphological effects on the field emission of ZnO nanorod arrays," *Applied Physics Letters*, vol. 86, no. 20, Article ID 203115, pp. 1–3, 2005.

[5] F.-Y. Hung, T.-S. Lui, Y.-T. Chen, and R.-S. Xiao, "Electrical crystallization mechanism and interface characteristics of nanowire ZnO/Al structures fabricated by the solution method," *Journal of Nanomaterials*, vol. 2012, Article ID 208362, 6 pages, 2012.

[6] H. Zhang, X. Wu, F. Qu, and G. Zhao, "ZnO microrod arrays grown on a curved sphere surface and their optical properties," *CrystEngComm*, vol. 13, no. 20, pp. 6114–6117, 2011.

[7] Y. Lei, F. Qu, and X. Wu, "Assembling ZnO nanorods into microflowers through a facile solution strategy: morphology control and cathodoluminescence properties," *Nano-Micro Letters*, vol. 4, no. 1, pp. 45–51, 2012.

[8] L. Yu, F. Qu, and X. Wu, "Solution synthesis and optimization of ZnO nanowindmills," *Applied Surface Science*, vol. 257, no. 17, pp. 7432–7435, 2011.

[9] L. Gong, X. Wu, C. Ye, F. Qu, and M. An, "Aqueous phase approach to ZnO microspindles at low temperature," *Journal of Alloys and Compounds*, vol. 501, no. 2, pp. 375–379, 2010.

[10] Q. Wan, Q. H. Li, Y. J. Chen et al., "Fabrication and ethanol sensing characteristics of ZnO nanowire gas sensors," *Applied Physics Letters*, vol. 84, no. 18, pp. 3654–3656, 2004.

[11] X. Wang, J. Zhang, Z. Zhu, and J. Zhu, "Humidity sensing properties of Pd^{2+}-doped ZnO nanotetrapods," *Applied Surface Science*, vol. 253, no. 6, pp. 3168–3173, 2007.

[12] N. Al-Hardan, M. J. Abdullah, and A. A. Aziz, "The gas response enhancement from ZnO film for H_2 gas detection," *Applied Surface Science*, vol. 255, no. 17, pp. 7794–7797, 2009.

[13] H. Xu, X. Liu, D. Cui, M. Li, and M. Jiang, "A novel method for improving the performance of ZnO gas sensors," *Sensors and Actuators B*, vol. 114, no. 1, pp. 301–307, 2006.

[14] J. Xu, Q. Pan, Y. Shun, and Z. Tian, "Grain size control and gas sensing properties of ZnO gas sensor," *Sensors and Actuators B*, vol. 66, no. 1, pp. 277–279, 2000.

[15] C. M. Ghimbeu, J. Schoonman, M. Lumbreras, and M. Siadat, "Electrostatic spray deposited zinc oxide films for gas sensor applications," *Applied Surface Science*, vol. 253, no. 18, pp. 7483–7489, 2007.

[16] Y. Zeng, T. Zhang, H. Yang et al., "Preparation of Cu-Zn/ZnO core-shell nanocomposite by wire electrical explosion and precipitation process in aqueous solution and CO sensing properties," *Applied Surface Science*, vol. 255, no. 7, pp. 4045–4049, 2009.

[17] M. Tiemann, "Porous metal oxides as gas sensors," *Chemistry*, vol. 13, no. 30, pp. 8376–8388, 2007.

[18] T. Waitz, T. Wagner, T. Sauerwald, C. D. Kohl, and M. Tiemann, "Ordered mesoporous In_2O_3: synthesis by structure replication

and application as a methane gas sensor," *Advanced Functional Materials*, vol. 19, no. 4, pp. 653–661, 2009.

[19] N. S. Ramgir, Y. K. Hwang, S. H. Jhung et al., "CO sensor derived from mesostructured Au-doped SnO_2 thin film," *Applied Surface Science*, vol. 252, no. 12, pp. 4298–4305, 2006.

[20] A. H. Lu and F. Schüth, "Nanocasting: a versatile strategy for creating nanostructured porous materials," *Advanced Materials*, vol. 18, no. 14, pp. 1793–1805, 2006.

[21] M. Tiemann, "Repeated templating," *Chemistry of Materials*, vol. 20, no. 3, pp. 961–971, 2008.

[22] H. Yang and D. Zhao, "Synthesis of replica mesostructures by the nanocasting strategy," *Journal of Materials Chemistry*, vol. 15, no. 12, pp. 1217–1231, 2005.

[23] H. Yang, Q. Shi, B. Tian et al., "One-step nanocasting synthesis of highly ordered single crystalline indium oxide nanowire arrays from mesostructured frameworks," *Journal of the American Chemical Society*, vol. 125, no. 16, pp. 4724–4725, 2003.

[24] F. Jiao, A. Harrison, J. C. Jumas, A. V. Chadwick, W. Kockelmann, and P. G. Bruce, "Ordered mesoporous Fe_2O_3 with crystalline walls," *Journal of the American Chemical Society*, vol. 128, no. 16, pp. 5468–5474, 2006.

[25] Y. Wang, C. M. Yang, W. Schmidt, B. Spliethoff, E. Bill, and F. Schüth, "Weakly ferromagnetic ordered mesoporous Co_3O_4 synthesized by nanocasting from vinyl-functionalized cubic Ia3d mesoporous silica," *Advanced Materials*, vol. 17, no. 1, pp. 53–56, 2005.

[26] C. Dickinson, W. Zhou, R. P. Hodgkins, Y. Shi, D. Zhao, and H. He, "Formation mechanism of porous single-crystal Cr_2O_3 and Co_3O_4 templated by mesoporous silica," *Chemistry of Materials*, vol. 18, no. 13, pp. 3088–3095, 2006.

[27] T. Waitz, M. Tiemann, P. J. Klar, J. Sann, J. Stehr, and B. K. Meyer, "Crystalline ZnO with an enhanced surface area obtained by nanocasting," *Applied Physics Letters*, vol. 90, no. 12, Article ID 123108, 2007.

[28] T. Wagner, T. Waitz, J. Roggenbuck, M. Fröba, C. D. Kohl, and M. Tiemann, "Ordered mesoporous ZnO for gas sensing," *Thin Solid Films*, vol. 515, no. 23, pp. 8360–8363, 2007.

[29] P. Siciliano, "Preparation, characterisation and applications of thin films for gas sensors prepared by cheap chemical method," *Sensors and Actuators B*, vol. 70, no. 1–3, pp. 153–164, 2000.

[30] S. Choopun, A. Tubtimtae, T. Santhaveesuk, S. Nilphai, E. Wongrat, and N. Hongsith, "Zinc oxide nanostructures for applications as ethanol sensors and dye-sensitized solar cells," *Applied Surface Science*, vol. 256, no. 4, pp. 998–1002, 2009.

[31] C. S. Rout, S. Hari Krishna, S. R. C. Vivekchand, A. Govindaraj, and C. N. R. Rao, "Hydrogen and ethanol sensors based on ZnO nanorods, nanowires and nanotubes," *Chemical Physics Letters*, vol. 418, no. 4-6, pp. 586–590, 2006.

[32] D. Zhao, Q. Huo, J. Feng, B. F. Chmelka, and G. D. Stucky, "Nonionic triblock and star diblock copolymer and oligomeric sufactant syntheses of highly ordered, hydrothermally stable, mesoporous silica structures," *Journal of the American Chemical Society*, vol. 120, no. 24, pp. 6024–6036, 1998.

[33] S. Jun, S. H. Joo, R. Ryoo et al., "Synthesis of new, nanoporous carbon with hexagonally ordered mesostructure," *Journal of the American Chemical Society*, vol. 122, no. 43, pp. 10712–10713, 2000.

[34] J. A. Schwarz, C. Contescu, and A. Contescu, "Methods for preparation of catalytic materials," *Chemical Reviews*, vol. 95, no. 3, pp. 477–510, 1995.

[35] N. G. Patel, P. D. Patel, and V. S. Vaishnav, "Indium tin oxide (ITO) thin film gas sensor for detection of methanol at room temperature," *Sensors and Actuators B*, vol. 96, no. 1-2, pp. 180–189, 2003.

Hindawi Publishing Corporation
Journal of Nanomaterials
Volume 2013, Article ID 596313, 4 pages
http://dx.doi.org/10.1155/2013/596313

Review Article

Gas Phase Growth of Wurtzite ZnS Nanobelts on a Large Scale

Jing Wang, Yang Jiao, Yang Liu, Zhenglin Zhang, Fengyu Qu, and Xiang Wu

Key Laboratory for Photonic and Electronic Bandgap Materials, Ministry of Education and College of Chemistry and Chemical Engineering, Harbin Normal University, Harbin 150025, China

Correspondence should be addressed to Xiang Wu; wuxiang05@gmail.com

Received 15 December 2012; Accepted 26 December 2012

Academic Editor: Xijin Xu

We showed large-scale synthesis of ZnS nanobelts by simply thermal evaporation of ZnS powder in the presence of Au catalysts at 1020°C. Scanning electron microscope (SEM), transmission electron microscope (TEM), and X-ray diffraction (XRD) analyses demonstrated that the as-obtained ZnS nanobelts possess hexagonal wurtzite structures. The nanobelts have lengths ranging from tens to hundreds of micrometers, thicknesses of tens of nanometers, and widths ranging from hundreds of nanometers to the order of micrometers. The growth process was proposed on the basis of known vapor-liquid-solid (VLS) mechanism. Room temperature photoluminescence measurements showed that the as-synthesized ZnS nanostructures had a strong green emission bands at a wavelength of 427 nm, which can be attributed to deep-level emissions induced by defects or impurities.

1. Introduction

Semiconductor materials have been extensively researched due to their potential applications in optical, photocatalytic, and optoelectronic fields [1–7]. Among them, wide band gap II–VI semiconductors are efficient emitters from blue to UV spectra range and are likely candidates to replace materials like GaN in light emitting laser diodes [8]. In particular, Zinc sulfide, a direct wide band gap semiconductor (3.7 eV) with exciton binding energy of 40 meV [9], has a high refractive index [10] and a high transmittance in the visible range [11]. ZnS exhibits not only photoluminescence [12–14], but also acoustic luminescence [15], triboluminescence [16], electroluminescence [17, 18], and thermoluminescence [19]. One-dimensional ZnS nanostructures possess some novel properties different from their block counterpart. So far, a various of ZnS nanostructures including belts [20, 21], saws [22], combs and windmills [23], and fishbones [24], have been synthesized. In this paper, we reported large-scale synthesis of ZnS nanobelts. Au catalyst's effect on the as-obtained ZnS nanostructures morphologies was discussed. Photoluminescence properties of the as-product are also investigated.

2. Experimental Details

ZnS nanobelts were synthesized through a thermal evaporation process in a horizontal tube furnace. 1 g commercial-grade ZnS powder (Alfa Aesar, 99.99% purity) was placed in the center of a single-zone tube furnace and evacuated for 3 hours to purge oxygen from the chamber, then the furnace was heated 1020°C at a rate of 20°C/min and keep at this temperature for 1 h. A carrier gas of high-purity Ar premixed with 5% H_2 was kept flowing at a rate 50 sccm. The pressure inside the tube was maintained at 300 Torr during the whole experiment. After the furnace was cooled to room temperature, a white-yellow wool-like product was deposited on Si substrate. The collected products were characterized by a scanning electron microscope (SEM, Hitachi S-4800) equipped with an energy-dispersive X-ray detector (EDX, INCA300) and a transmission electron microscope (JEOL

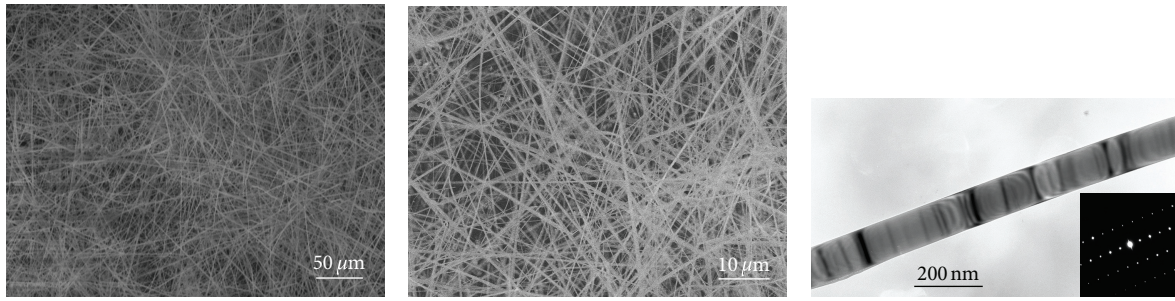

Figure 1: Morphology of the as-grown ZnS nanobelts (a) low magnification SEM image (b) high magnification SEM image (c) low magnification TEM image, the inset is the corresponding SAED pattern.

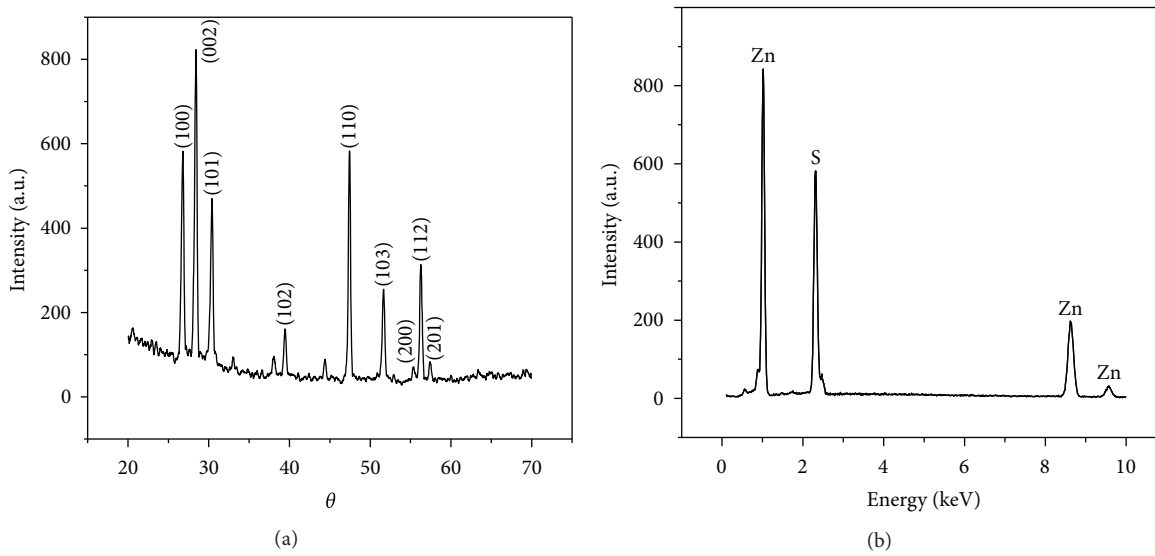

Figure 2: (a) XRD pattern of the as-synthesized ZnS nanobelts (b) EDS spectrum of the as-synthesized ZnS nanobelts.

JEM-2010). Photoluminescence (PL) spectra were recorded at room temperature using a He-Cd laser with a wavelength of 325 nm as the excitation light source.

3. Results and Discussion

The general morphologies of the as-made products were examined using SEM, which were showed in Figure 1. Figure 1(a) is low magnification SEM images of ZnS nanobelts, one can find large quantities of wire-like structures covered on Si substrate. Figure 1(b) is the high magnification SEM images. Further observation found that the wirelike product present belt-like cross sections with an width of about 100 nm to 300 nm and a length of several tens of micrometers. Figure 1(c) and the insert show a typical of low magnified TEM image of the as-grown single ZnS nanobelt and the corresponding SAED pattern, revealing that the as-synthesized ZnS nanobelt possesses single crystalline structure through the entire length. ZnS nanobelt grows along [0001] direction.

Figure 2(a) shows XRD pattern of the as-grown products. All peaks of spectrum can be indexed to hexagonal wurtzite structure of ZnS, with the lattice constants $a = 0.382$ nm and $c = 0.626$ nm, which match well to the PDF card (no. 36-1450), without any impurities detected. Figure 2(b) is an EDS spectrum of the product, only Zn and S element are detected and Zn/S is about 1 : 1 within experimental errors. This showed again the as-grown product of ZnS possess high purity.

Because Au catalyst was introduced during reaction, it is obvious that the growth mechanism of the as-grown product of ZnS was controlled by well-known VLS mechanism. At first, ZnS powder evaporated to ZnS vapor at high temperature, then ZnS vapor react with H_2 to produce Zn and H_2S vapor, after that Zn vapor and H_2S vapor were carried to low temperature zone by Ar gas carrier and deposited on Si substrate. Zn and Au formed ZnAu solid solution as nuclei to absorb Zn vapors and H_2S vapor, where Zn reacts with H_2S and form ZnS, during the whole growth process, Zn and H_2S continuously separated from ZnAu solid solution and from

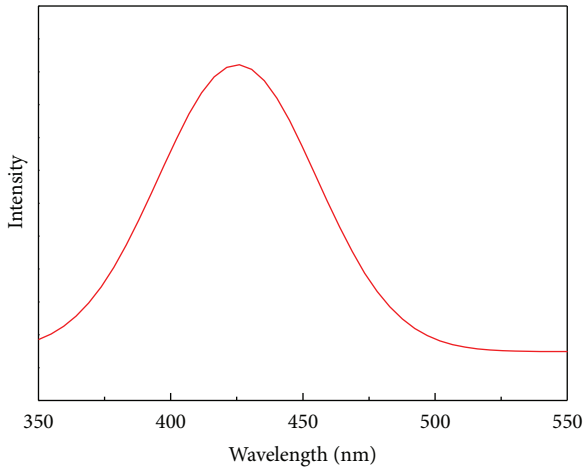

Figure 3: Room temperature photoluminescence spectrum of the as-synthesized ZnS nanobelts.

the ZnS nanobelts. However, No gold nanoparticles were found on the surface of the as-synthesized ZnS nanobelts, it is possible that Au particle catalysts have been evaporated when the growth of ZnS nanobelts finishes, which is consistent with the explanation to the growth of ZnO and $ZnGa_2O_4$ nanohelices [25, 26].

Figure 3 showed room temperature photoluminescence spectrum of the ZnS nanobelts. One can see only a stable and strong blue emission peak at 427 nm. As known, near band edge (NBE) emission of ZnS should position at 337 nm due to combination of free excitons. Thus, the emission bands centered at 427 nm should be assigned to the stoichiometric vacancies or interstitial impurities in the ZnS nanoribbons, which has been reported by some literature [27, 28].

4. Conclusion

In summary, we have successfully synthesized wurtzite ZnS nanobelts in the presence of Au catalysts by thermal evaporation of ZnS powder at 1020°C. The single crystalline ZnS nanobelts ranged from tens to hundreds of micrometers in length and hundreds of nanometers in width. Growth process may be explained by conventional VLS mechanism. Strong green emission of ZnS nanobelts may be attributed Au purity and high density of defects. The as-grown ZnS nanobelts here may be used as building blocks to fabricate various functionalized nanodevices.

Acknowledgments

This work was supported by Program for New Century Excellent Talents in Heilongjiang Provincial University (1252-NCET-018).

References

[1] X. Wu, P. Jiang, Y. Ding, W. Cai, S. S. Xie, and Z. L. Wang, "Mismatch strain induced formation of ZnO/ZnS heterostructured rings," *Advanced Materials*, vol. 19, pp. 2319–2323, 2007.

[2] M. Y. Lu, M. P. Lu, Y. A. Chung, M. J. Chen, Z. L. Wang, and L. J. Chen, "Intercrossed sheet-like Ga-doped ZnS nanostructures with superb photocatalytic activity and photoresponse," *The Journal of Physical Chemistry C*, vol. 113, pp. 12878–12882, 2009.

[3] H. Zeng, W. Cai, P. Liu et al., "ZnO-based hollow nanoparticles by selective etching: elimination and reconstruction of metal-semiconductor interface, improvement of blue emission and photocatalysis," *ACS Nano*, vol. 2, no. 8, pp. 1661–1670, 2008.

[4] X. Wu, W. Cai, and F. Y. Qu, "Tailoring morphologies and wettability property of ZnO 1D nanostructures," *Acta Physica Sinica*, vol. 58, pp. 8044–8049, 2009.

[5] H. B. Zeng, G. T. Duan, Y. Li, S. K. Yang, X. X. Xu, and W. P. Cai, "Blue luminescence of ZnO nanoparticles based on nonequilibrium process: defect origins and emission controls," *Advanced Functional Materials*, vol. 20, pp. 561–572, 2010.

[6] L. J. Yu, F. Y. Qu, and X. Wu, "Facile hydrothermal synthesis of novel ZnO nanocubes," *Journal of Alloys and Compounds*, vol. 504, pp. L1–L4, 2010.

[7] H. B. Chen, X. Wu, L. H. Gong, C. Ye, F. Y. Qu, and G. Z. Shen, "Hydrothermally-grown ZnO micro/nanotube arrays and their properties," *Nanoscale Research Letters*, vol. 5, pp. 570–575, 2010.

[8] J. Gutowski, P. Michler, H. I. Rückmann et al., "Excitons in wide-gap semiconductors: coherence, dynamics, and lasing," *Physica Status Solidi B*, vol. 234, pp. 70–83, 2002.

[9] H. C. Ong and R. P. Chang, "Optical constants of wurtzite ZnS thin films determined by spectroscopic ellipsometry," *Applied Physics Letters*, vol. 79, article 3612, 2001.

[10] X. C. Jiang, Y. Xie, J. Liu, L. Y. Zhu, W. He, and Y. T. Qian, "Simultaneous in situ formation of ZnS nanowires in a liquid crystal template by γ-irradiation," *Chemistry of Materials*, vol. 13, pp. 1213–1218, 2001.

[11] S. Yamaga, A. Yoshikawa, and H. Kasai, "Electrical and optical properties of donor doped ZnS films grown by low-pressure MOCVD," *Journal of Crystal Growth*, vol. 86, no. 1–4, pp. 252–256, 1990.

[12] X. Wu, J. H. Sui, W. Cai, and P. Jiang, "Temperature-Controllable Preparation of ZnS Nanosaws on Si Substrate," *Chinese Physics Letters*, vol. 25, pp. 737–739, 2008.

[13] W. N. Jia, B. X. Jia, X. Wu, and F. Y. Qu, "Self assembly of shape-controlled ZnS nanostructures with novel yellow light photoluminescence and excellent hydrophobic properties," *CrystEngCommunity*, vol. 14, pp. 7759–7763, 2012.

[14] S. Biswas, T. Ghoshal, S. Kar, S. Chakrabarti, and S. Chaudhuri, "ZnS nanowire arrays: synthesis, optical and field emission properties," *Crystal Growth and Design*, vol. 8, no. 7, pp. 2171–2176, 2008.

[15] T. V. Prevenslik, "Acoustoluminescence and sonoluminescence," *Journal of Luminescence*, vol. 87–89, pp. 1210–1212, 2000.

[16] C. N. Xu, T. Watannbe, M. Akiyama, and X. G. Zheng, "Preparation and characteristics of highly triboluminescent ZnS film," *Materials Research Bulletin*, vol. 34, pp. 1491–1500, 1999.

[17] X. Wu, Y. lei, Y. Zheng, and F. Qu, "Controlled growth and cathodoluminescence property of ZnS nanobelts with large aspect ratio," *Nano-Micro Letters*, vol. 2, pp. 272–276, 2010.

[18] J. Yan, X. Fang, L. Zhang et al., "Structure and cathodoluminescence of individual ZnS/ZnO biaxial nanobelt heterostructures," *Nano Letters*, vol. 8, no. 9, pp. 2794–2799, 2008.

[19] W. Chen, Z. G. Wang, Z. J. Lin, and L. Y. Lin, "Thermoluminescence of ZnS nanoparticles," *Applied Physics Letters*, vol. 70, article 1465, 3 pages, 1997.

[20] X. Fan, X. M. Meng, X. H. Zhang et al., "Dart-shaped tricrystal ZnS nanoribbons," *Angewandte Chemie*, vol. 45, no. 16, pp. 2568–2571, 2006.

[21] Y. Jiang, X. M. Meng, J. Liu, Z. Y. Xie, C. S. Lee, and S. T. Lee, "Hydrogen-assisted thermal evaporation synthesis of ZnS nanoribbons on a large scale," *Advanced Materials*, vol. 15, pp. 323–327, 2003.

[22] D. F. Moore, C. Ronning, C. Ma, and Z. L. Wang, "Wurtzite ZnS nanosaws produced by polar surfaces," *Chemical Physics Letters*, vol. 385, pp. 8–11, 2004.

[23] C. Ma, D. Moore, J. Li, and Z. L. Wang, "Nanobelts, nanocombs, and nanowindmills of wurtzite ZnS," *Advanced Materials*, vol. 15, pp. 228–231, 2003.

[24] X. Wu, F. Y. Qu, G. Z. Shen, and W. Cai, "Large scale synthesis of fishbone-like ZnS nanostructures using ITO glass as the substrate," *Journal of Alloys and Compounds*, vol. 482, pp. L32–L35, 2009.

[25] X. Wu, W. Cai, and F. Y. Qu, "Spontaneous formation of single crystal ZnO nanohelices," *Chinese Physics B*, vol. 18, pp. 1669–1773, 2009.

[26] S. Y. Bae, J. Lee, H. Jung, J. Park, and J. P. Ahn, "Helical structure of single-crystalline $ZnGa_2O_4$ nanowires," *Journal of the American Chemical Society*, vol. 127, no. 31, pp. 10802–10803, 2005.

[27] S. Kar and S. Chaudhuri, "Controlled synthesis and photoluminescence properties of ZnS nanowires and nanoribbons," *Journal of Physical Chemistry B*, vol. 109, no. 8, pp. 3298–3302, 2005.

[28] P. A. Hu, Y. Q. Liu, L. Fu, L. C. Cao, and D. B. Zhu, "Self-assembled growth of ZnS nanobelt networks," *Journal of Physical Chemistry B*, vol. 108, pp. 936–938, 2004.

Hindawi Publishing Corporation
Journal of Nanomaterials
Volume 2012, Article ID 909473, 6 pages
doi:10.1155/2012/909473

Research Article

Gas-Supported High-Photoactivity TiO_2 Nanotubes

Sheng Wang, Tao Wang, Yuanwei Ding, Youfeng Xu, Qiying Su, Yanlong Gao, Guohua Jiang, and Wenxing Chen

Key Laboratory of Advanced Textile Materials and Manufacturing Technology of Ministry of Education, Zhejiang Sci-Tech University, Hangzhou 310018, China

Correspondence should be addressed to Sheng Wang, wangsheng571@hotmail.com

Received 18 October 2012; Accepted 28 November 2012

Academic Editor: Xijin Xu

By changing hydrothermal condition and post-heat-treatment temperature, silica-coated TiO_2 nanotubes are obtained successfully. The effects of gas-supported process on tubular morphology, crystallinity, and photocatalytic activity are discussed. It is found that the sample prepared at hydrothermal treatment (180°C/9 h) and calcination (650°C/2 h) shows perfect open-ended tubular morphology and increased crystallinity. The photoactivity of the sample is proved to be 5 times higher than that of TiO_2 nanoparticles.

1. Introduction

TiO_2-based nanomaterials have been intensely investigated due to its applications in air purification, water disinfection, hazardous water remediation, and other fields since Honda and Fujishima discovered the photocatalytic splitting of water on the TiO_2 electrodes in 1972 [1–5]. In particular, TiO_2 nanotubes (TiO_2-NTs) with high surface area, porosity, low cost, and chemical stability are attracting considerable attention, as compared with other nanostructures, and would be good candidates for potential applications in photocatalysis, gas sensing, pigments, photovoltaic applications, solar cells, and water detoxification applications [6–10].

On the other hand, as we know, photocatalytic activity is a comprehensive parameter, which is affected by many factors such as morphology, crystallinity, surface area, doping elements, and so on. However, it is very difficult to adjust each factor alone during the preparation process of nanomaterials. For instance, high-quality hydrogen titanate nanotubes (Titanate-NTs) can be obtained by a simple hydrothermal treatment of crystalline TiO_2 particles with NaOH aqueous solutions. But the as-prepared products are predominately in amorphous phase, shows low photocatalytic activity. Therefore, since their photocatalytic performance is closely related to crystallinity, additional crystallization is always required for those products. Unfortunately, such materials are also prone to collapse during the calcination process. As a result, the tubular morphology is destroyed, with a significant decrease in specific surface area (S_{BET}), pore volume, and photocatalytic activity [11–13].

How to adjust both morphology and crystallinity to improve photocatalytic activity of TiO_2-NTs is a challenging subject for us. In our previous work, we presented a simple chemical morphology-freezing method, at post-heat-treatment process by combustion of filled carbon in titanate nanotubes to obtain gas-phase support of CO_2, and after calcination at 500°C we obtained high photoactivity TiO_2/SiO_2 nanotubes (TiO_2-NT_S@@SiO_2) with perfect one-dimensional tubular morphology and fine crystal form for photocatalysis, which is 4 times higher than TiO_2 nanoparticles (P-25) [14].

In this work, we find, during the gas-supported process, that phase transfer temperature of TiO_2 from anatase to rutile is delayed by combustion of carbon to CO_2. By using this phenomenon, we improve the preparation method and obtain TiO_2 nanotubes with perfect open-ended tubular morphology and increased crystallinity at much higher temperature. The photoactivity of sample is proved 5 times higher than TiO_2 nanoparticles.

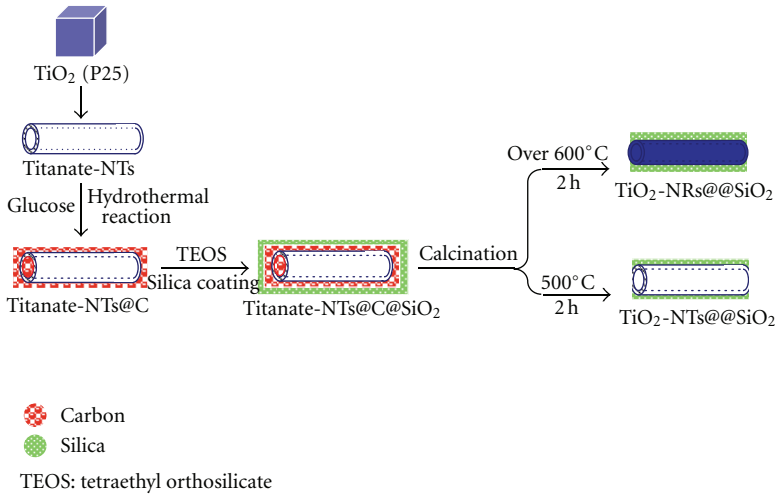

Scheme 1: Formation process of TiO_2-NTs@@SiO_2 (500°C, 2 h) and TiO_2-NRs@@SiO_2 (Over 600°C, 2 h).

2. Experimental Details

2.1. Synthesis of TiO_2-NTs@SiO_2 Tubular Nanocomposites. TiO_2-NTS@@SiO_2 nanocomposites were prepared by using chemical morphology freezing method that was described in our previous work [14]. First, hydrogen titanate nanotubes (Titanate-NTs) were prepared, and a carbon layer was coated on Titanate-NTs by hydrothermal treatment to prepare carbon-coated Titanate-NTs (Titanate-NTs@C). Then a second silica layer was followed to coat onto Titanate-NTs@C via a conventional alkoxide sol-gel method (Titanate-NTs@C@SiO_2). Finally the sample was calcined and the carbon layer was combusted to yield TiO_2-NTs@@SiO_2 tubular nanocomposites.

2.2. Characterization. Transmission electron microscopy (TEM) samples were prepared by suspending the nanoparticles in ethanol and then casting on a holey, carbon-coated Cu grid. High-resolution TEM images were obtained with a JEM-2010(HR) instrument operating at 200 kV. Energy dispersive X-ray analysis (EDS, Inca Energy-200) was used to investigate the sample compositions. X Ray diffraction (XRD) patterns were obtained on a D/MAX-RB X-ray diffractometer (D/Max-2550pc), using Cu-Kα radiation at a scan rate (2θ) of 0.05° s^{-1}, and were used to determine the phase structure of the obtained samples. The accelerating voltage and the applied current were 15 kV and 20 mA, respectively. Specific surface area (S_{BET}) was determined using a Micromeritics Tristar 3000.

2.3. Measurement of Photocatalytic Activity. The photocatalytic activity of TiO_2-NTs@@SiO_2 was defined as the amount of CO_2 that resulted from the photocatalytic decomposition of methanol/water solution (5%, volume ratio). 40 mg sample was suspended in a solution of methanol (4 mL). The methanol vapor was allowed to reach adsorption-desorption equilibrium with catalysts in the reactor prior to UV light irradiation. Then the suspension was irradiated with UV light (500 W) at 25°C. After irradiation, the generated CO_2 gas was collected with a syringe and analyzed by gas chromatography (6890N, Agilent) [13, 14].

3. Result and Discussion

3.1. CO_2 Gas-Supported TiO_2-NTs@SiO_2. Open-ended Titanate-NTs, which with diameters of 4 to 7 nm and lengths of several hundred nanometers, were obtained by a hydrothermal reaction using Degussa P25 and 10 M NaOH aqueous solution at 150°C for 48 h (Scheme 1, Figure 1(a)). In order to obtain high photoactivity TiO_2 nanotubes, with perfect open-ended tubular morphology and fine anatase phase, Titanate-NTs were filled with LaMer-model carbon and then coated with a silica layer. This filling and coating process "isolates" microthermal deformation from the system and consequently prevents the destruction of the tubular morphology during the calcination process. After calcination at 500°C for 2 hours, TiO_2-NTs@@SiO_2 were obtained by CO_2 gas supporting and showed the higher photoactivity of all the samples, which is 4 times higher than TiO_2 nanoparticles (Figure 1(b)) [14].

On the other hand, it is generally accepted that crystallization is always an aggregation process from amorphous state, and crystals grow by attachment of ions to inorganic surfaces or organic templates [15]. Numerous researches describe the similar crystallization process of TiO_2 crystallites. With increasing calcination temperature from 400°C to 600°C, the crystallization of anatase phase improves, indicating that at high temperature amorphous Ti atoms move into anatase crystal location. Usually, the anatase phase starts to transform to rutile phase when the calcination temperature exceeds 600°C. Since anatase phase of TiO_2 is beneficial to photoactivity, it is believed that the phase transform temperature is the most optimal temperature to achieve prefect anatase phase of TiO_2 and best photoactivity as well.

However, in the CO_2 gas-supported process, it is observed that TiO_2-NTs@@SiO_2 nanocomposites keep as pure anatase phase even at 700°C, which indicates that phase

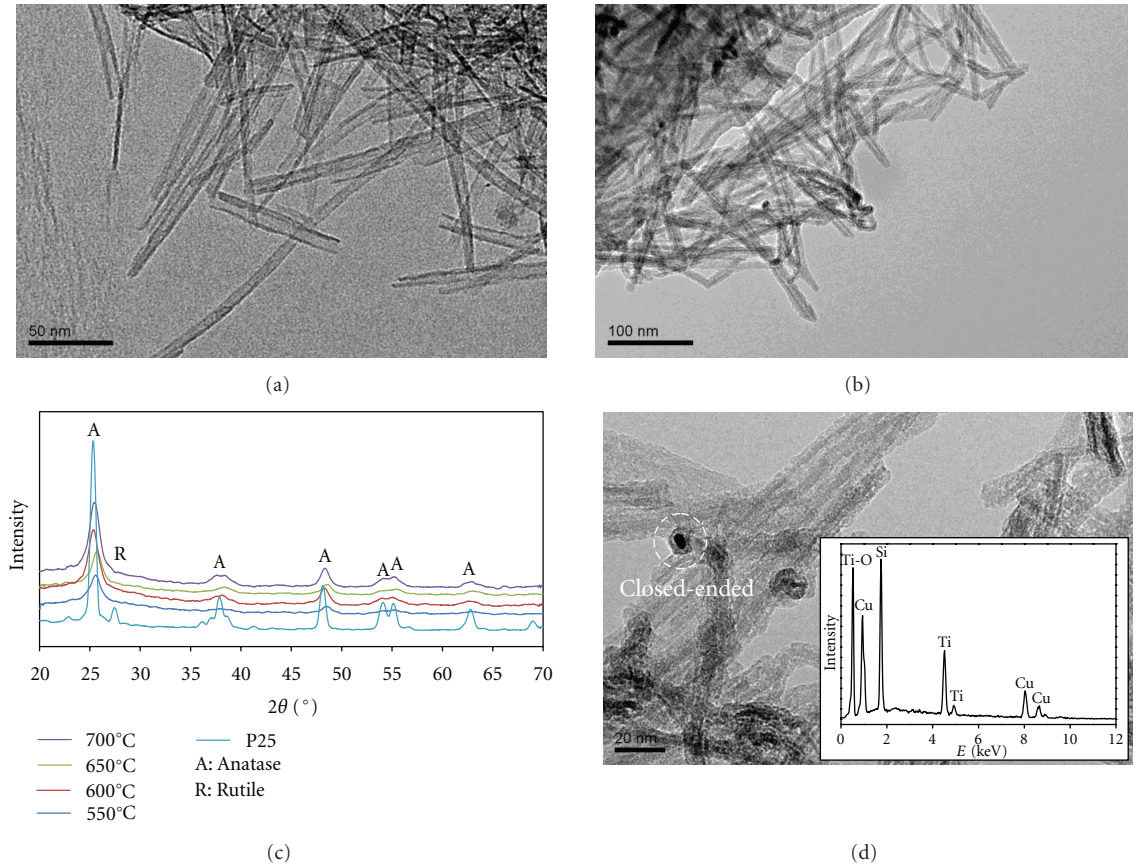

FIGURE 1: TEM images of (a) titanate nanotubes, (b) TiO_2-NTs@@SiO_2 with "open-ended" structure (500°C, 2 h). (c) XRD pattern of TiO_2-NTs@@SiO_2 calcined at various temperatures. (d) TiO_2-NRs@@SiO_2 with "close-ended" structure (over 600°C, 2 h) and EDS spectra of the sample (inset).

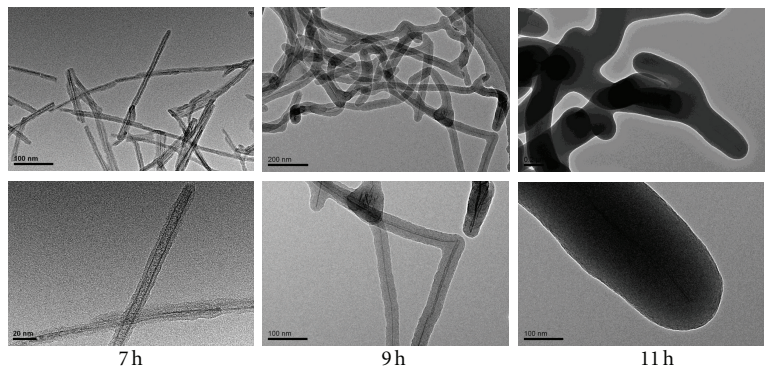

FIGURE 2: TEM images of Titanate-NTs@C under different carbon-treated hydrothermal reaction condition.

transfer temperature is delayed (Figure 1(c)). It is well known that the delay of phase transfer temperature is common in calcination process of nanoparticles doped with different elements, because doping with different types of elements will undoubtedly prevent migration of atom of host materials to the crystal location. However, it should be noted that EDS spectra of TiO_2-NTs@@SiO_2 show that after the calcination, evidence of Ti, Si, and O is found in sample and no carbon peak is observed, indicating the complete combustion of carbon in calcination process (Figure 1(d)). Moreover, XRD pattern of TiO_2-NTs@@SiO_2 exhibits that no characteristic peaks of C are observed, indicating that C element has not been doped in crystal lattice of TiO_2 (Figure 1(c)). Therefore, the experiment results suggest that in gas-supported process,

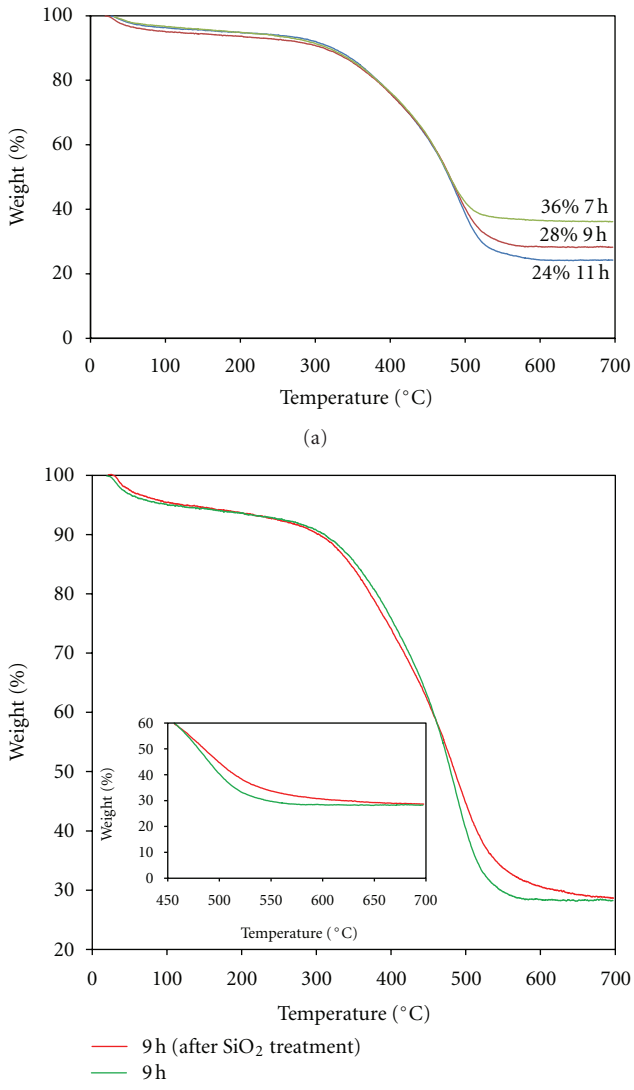

Figure 3: TG curves of (a) Titanate-NTs@C under different hydrothermal reaction time and (b) Titanate-NTs@C and Titanate-NTs@C@SiO_2 at 9 h hydrothermal reaction time.

the microcosmic migration of Ti atoms to the crystal location is prevented by CO_2 evolution, leading to the macroscopical delay of phase transfer temperature finally.

From our previous work, even after calcination at 500°C for 2 hours, some hydrogen titanate nanotubes may still have not been crystallized completely. If the remaining amorphous phase hydrogen titanate can be transformed into anatase phase completely, this will undoubtedly enhance the photoactivity of TiO_2-NTs. However, when the calcination temperature is increased to 600°C, the tubular morphology is significantly destroyed. As shown in Figure 1(d), only "close-ended" structure is observed, indicating that TiO_2-NTs has been collapsed and fused to TiO_2 nanorods (TiO_2-NRs@@SiO_2). As mentioned above, photoactivity is a comprehensive factor that is related to temperature, crystallinity, specific surface area, and so on, so it is a challenge to obtain

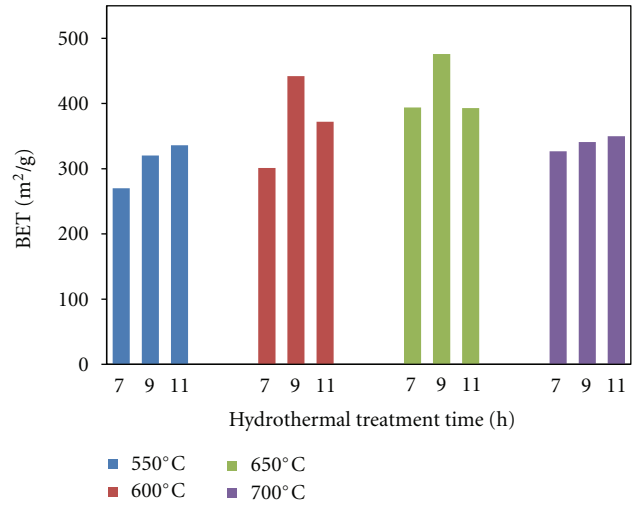

Figure 4: Specific surface area (S_{BET}) of Titanate-NTs@C@SiO_2 under different hydrothermal reaction condition and calcination temperature.

TiO_2-NTs with perfect tubular morphology at much higher temperature.

3.2. Improved Carbon-Treated Titanate Nanotubes. In order to keep the tubular morphology and large surface areas simultaneously at much higher calcination temperature, our strategy is to extend combustion time of carbon to support nanotubular morphology in gas-supported process. There are two options to select: one is to increase thickness of the silica coated layer to cut off air and retard combustion. However, experiment results showed such treatment always bring aggregation problem of silica itself and disadvantages in photocatalytic activity due to the excessively thick coating, which impeded mass transfer channel.

Therefore, it is a reasonable strategy to extend the combustion time by increasing the amount of carbon. The effects of the amount of carbon on the morphology and crystal structure of the nanotubes are studied at 180°C by changing the reaction time of carbon-treated hydrothermal reaction. As shown in Figure 2, after being carbon-treated for 7 h, titanate nanotubes with a diameter of 4 to 7 nm are covered with a carbon layer uniformly, and the thickness of carbon layer is about 3 nm. Extending the time of hydrothermal reaction, the thickness of carbon layer is increased effectively. The thickness of carbon layer is increased to about 20 nm for 9 h and over 120 nm for 11 h, respectively.

3.3. Thermogravimetric Analysis. The TG curves of the samples obtained at different hydrothermal reaction time (7 h, 9 h, 11 h) are shown in Figure 3(a). The curves are similar apparently except that each curve has a large weight loss at high temperature stage, which is considered as the combustion of carbon. It is observed that with increasing hydrothermal reaction time, weight loss of sample gradually increases, suggesting that the thickness and density of carbon layer increases linearly with the increase of hydrothermal

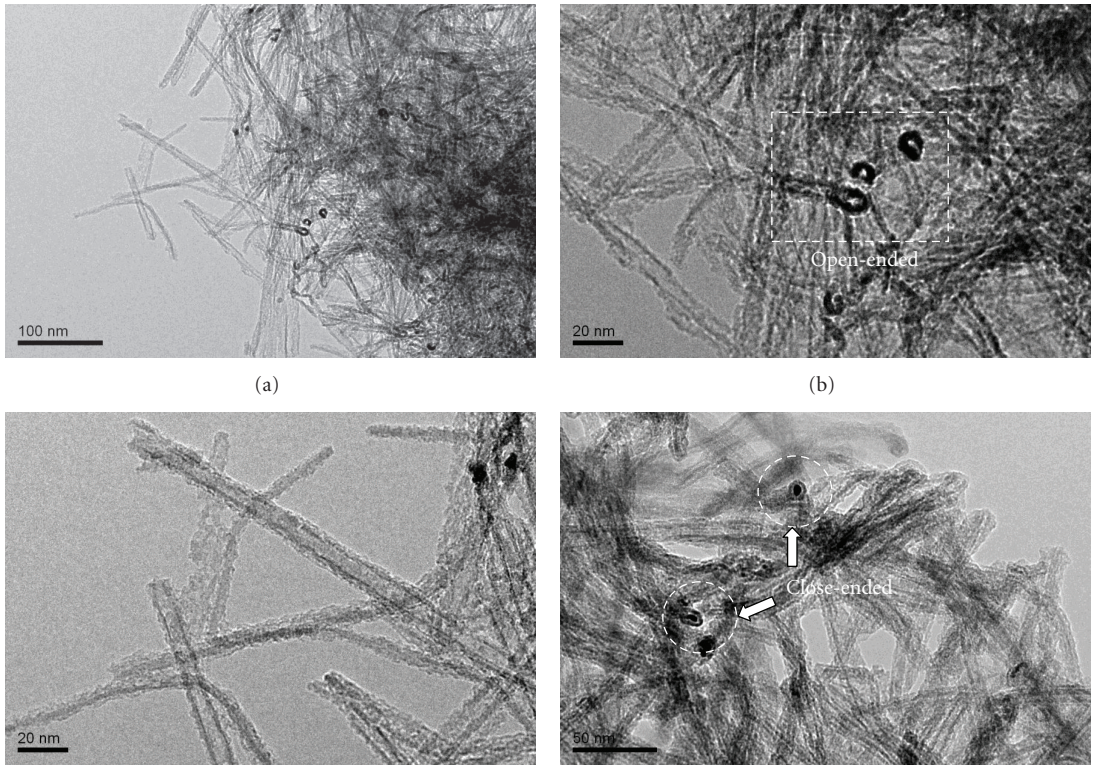

Figure 5: TEM images of (a), (b), and (c) TiO_2-NTs@@SiO_2 with "open-ended" structure (650°C, 2 h). (d) TiO_2-NRs@@SiO_2 with "close-ended" structure (700°C, 2 h).

reaction time, which is in good agreement with the SEM results.

As described in our previous work, we noted that a second silica layer, which is coated on carbon-treated sample, can significantly delay the combustion rate of carbon in the following calcination process. This delay is also confirmed by the TG analysis. For example, as shown in Figure 3(b), in case of sample of 9 h, it is found that after 600°C the weight loss of sample is almost constant. However, after SiO_2 treatment the weight loss of the sample increases continuously and finally comes to a constant until 700°C. The result strongly suggests that the carbon combustion rate of the silica-coated sample has been effectively decreased, which indicates that the tubular morphology is gas-supported by CO_2 evolution until 700°C.

3.4. S_{BET} of TiO_2-NTs@@SiO_2. Based on TG data, it can be calculated that the final stage of combustion occurred at about 550–700°C, so the silica-coated samples are calcined at this temperature range and S_{BET} of the samples is measured. As shown in Figure 4, it is clear that at different hydrothermal treatment time, the obtained S_{BET} is different even under the same calcination condition, which indicates that the different amount of carbon in a gas-supported process has obvious effects on the S_{BET} of the nanocomposites. Moreover, even under the same hydrothermal reaction condition, the obtained S_{BET} of samples is different at different calcination temperature, which strongly suggests that the carbon combustion rate affects the S_{BET} of the nanocomposites too. After all, the results of S_{BET} indicate that the sample prepared at 9 h hydrothermal treatment and 650°C calcination (9 h/650°C) exhibits the highest S_{BET}.

Figures 5(a)–5(c) are TEM images of the TiO_2-NTs@@SiO_2 (9 h/650°C), which show fine one-dimensional structure and open-ended tubular morphology. However, 700°C calcination temperature will cause TiO_2-NTs lose their tubular morphology and become the "close-ended" structure (Figure 5(d)).

3.5. Photocatalysis of TiO_2-NTs@@SiO_2. The photocatalytic activity of the TiO_2-NTs@@SiO_2 nanocomposites, which are prepared at various hydrothermal temperature and calcination temperature, are evaluated by photodecomposition of methanol. As shown in Figure 6, all of the TiO_2-NTs@@SiO_2 nanocomposites samples show higher photocatalytic activity than P25. The sample especially (9 h/650°C) shows the highest photoactivity of all the samples, which is about 5 times higher than that of P-25.

4. Conclusion

In summary, by changing carbon-treated hydrothermal reaction condition and post-heat-treatment temperature, the effects of gas-supported process on tubular morphology,

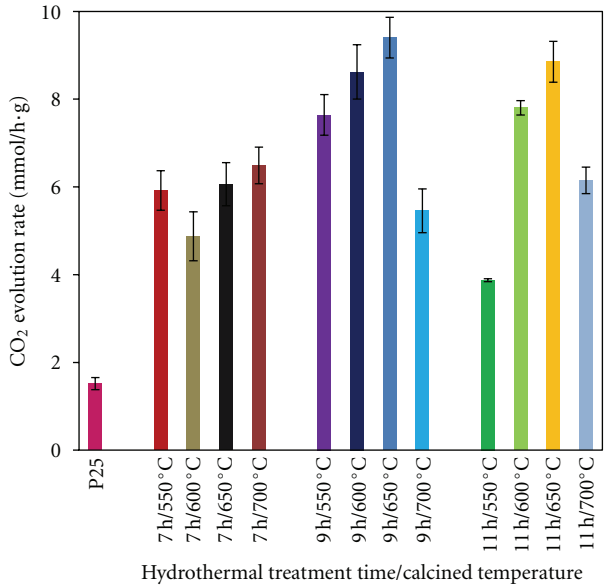

FIGURE 6: Relationship between the amount of CO_2 evolved and photocatalysts with different condition (hydrothermal reaction condition and calcination temperature).

crystallinity and photocatalytic activity of TiO_2-NTs@@SiO_2 nanocomposites are investigated. It is found that the sample prepared using hydrothermal treatment (180°C/9 h) and calcination (650°C/2 h) has high-crystallinity and prefect tubular morphology. The sample shows the highest photoactivity of all the samples, which is about 5 times higher than that of P-25.

Acknowledgments

This work was supported by NSFC (50802088, 31070888, 21103152, and 51133006), ZJNSF (R2101054, Y4080392, and Y4100045), Zhejiang Welfare Technology Applied Research Project (2012C23050), and ZJQJSF (2010R10023).

References

[1] R. Wang, K. Hashimoto, A. Fujishima et al., "Light-induced amphiphilic surfaces," *Nature*, vol. 388, no. 6641, pp. 431–432, 1997.

[2] G. Palmisano, V. Augugliaro, M. Pagliaro, and L. Palmisano, "Photocatalysis: a promising route for 21st century organic chemistry," *Chemical Communications*, no. 33, pp. 3425–3437, 2007.

[3] D. Ravelli, D. Dondi, M. Fagnoni, and A. Albini, "Photocatalysis. A multi-faceted concept for green chemistry," *Chemical Society Reviews*, vol. 38, no. 7, pp. 1999–2011, 2009.

[4] M. N. Chong, B. Jin, C. W. K. Chow, and C. Saint, "Recent developments in photocatalytic water treatment technology: a review," *Water Research*, vol. 44, no. 10, pp. 2997–3027, 2010.

[5] H. Tong, S. Ouyang, Y. Bi, N. Umezawa, M. Oshikiri, and J. Ye, "Nano-photocatalytic materials: possibilities and challenges," *Advanced Materials*, vol. 24, pp. 229–251, 2012.

[6] O. Beckstein, P. C. Biggin, and M. S. P. Sansom, "A hydrophobic gating mechanism for nanopores," *Journal of Physical Chemistry B*, vol. 105, no. 51, pp. 12902–12905, 2001.

[7] J. Lee, H. Kim, S. J. Kahng et al., "Bandgap modulation of carbon nanotubes by encapsulated metallofullerenes," *Nature*, vol. 415, no. 6875, pp. 1005–1008, 2002.

[8] L. Yang, T. A. Harroun, T. M. Weiss, L. Ding, and H. W. Huang, "Barrel-stave model or toroidal model? A case study on melittin pores," *Biophysical Journal*, vol. 81, no. 3, pp. 1475–1485, 2001.

[9] J. K. Holt, A. Noy, T. Huser, D. Eaglesham, and O. Bakajin, "Fabrication of a carbon nanotube-embedded silicon nitride membrane for studies of nanometer-scale mass transport," *Nano Letters*, vol. 4, no. 11, pp. 2245–2250, 2004.

[10] J. Zhang, X. Liu, R. Blume, A. Zhang, R. Schlögl, and D. S. Su, "Surface-modified carbon nanotubes catalyze oxidative dehydrogenation of n-butane," *Science*, vol. 322, pp. 73–77, 2008.

[11] M. Zhang, Z. Jin, J. Zhang et al., "Effect of annealing temperature on morphology, structure and photocatalytic behavior of nanotubed $H_2Ti_2O_4(OH)_2$," *Journal of Molecular Catalysis A*, vol. 217, pp. 203–210, 2004.

[12] G. H. Du, Q. Chen, R. C. Che, Z. Y. Yuan, and L. P. Peng, "Preparation and structure analysis of titanium oxide nanotubes," *Applied Physics Letters*, vol. 79, no. 22, p. 3702, 2001.

[13] T. Wang, S. Wang, W. Chen et al., "Chemical morphology freezing: chemical protection of the physical morphology of high photoactivity anatase TiO_2 nanotubes," *Journal of Materials Chemistry*, vol. 19, no. 27, pp. 4692–4694, 2009.

[14] S. Wang, T. Wang, Y. L. Gao, Y. W. Ding, G. H. Jiang, and W. X. Chen, "Wet photochemical filling: a new low-diameter tube-filling method based on differentiated nanotube surfaces," *Journal of Materials Chemistry*, vol. 21, no. 48, pp. 19337–19343, 2011.

[15] J. F. Banfield, S. A. Welch, H. Zhang, T. T. Ebert, and R. L. Penn, "Aggregation-based crystal growth and microstructure development in natural iron oxyhydroxide biomineralization products," *Science*, vol. 289, no. 5480, pp. 751–754, 2000.

Hindawi Publishing Corporation
Journal of Nanomaterials
Volume 2012, Article ID 269064, 5 pages
doi:10.1155/2012/269064

Research Article

Effect of Alumina Dopant on Transparency of Tetragonal Zirconia

Haibin Zhang,[1] Zhipeng Li,[2] Byung-Nam Kim,[1] Koji Morita,[1] Hidehiro Yoshida,[1] Keijiro Hiraga,[1] and Yoshio Sakka[1]

[1] *Advanced Materials Processing Unit, National Institute for Materials Science, 1-2-1 Sengen, Tsukuba, Ibaraki 305-0047, Japan*
[2] *Global Research Center for Environment and Energy based on Nanomaterials Science (GREEN), National Institute for Materials Science, 1-1 Namiki, Tsukuba, Ibaraki 305-0044, Japan*

Correspondence should be addressed to Haibin Zhang, hbzhang1978@gmail.com

Received 28 October 2012; Accepted 15 December 2012

Academic Editor: Xijin Xu

Aiming to characterize the effect of alumina dopant on transparency, powders of yttria stabilized tetragonal zirconia doped with alumina (TZ-3Y-E) are used as starting material to fabricate transparent tetragonal ZrO_2 by high-pressure spark plasma sintering (HP-SPS). However, low transparency of the resultant TZ-3Y-E specimens does not suggest a beneficial effect of alumina dopant although nanometric grains and high density have been achieved. The mechanism is analyzed by comparing with the results of as-sintered yttria stabilized tetragonal zirconia without alumina dopant.

1. Introduction

Yttria stabilized tetragonal zirconia polycrystal (Y-TZP) possesses many salient properties, such as high strength, toughness, wear resistance, chemical resistance, and biocompatibility, which make it as a promising candidate for various structural and biomedical applications [1]. As a hard-to-sinter ceramic, polycrystalline Y-TZP usually is opaque even after high-temperature sintering mainly because of the existence of residual pores. Such pores can significantly scatter incident light and deteriorate optical properties. In addition, nanometric microstructure is crucial to achieve good transparency for Y-TZP since this material has serious birefringent scattering (one order of magnitude higher than that of alumina) [2].

Very recently, Krell and coworkers propose a model based on Mie theory to quantitatively describe the scattering behavior in Y-TZP [2]. This model points out that the in-line transmittance of 50% at the visible wavelength range is expected as the grain size <40 nm for a pore-free Y-TZP with 1 mm thickness [2]. This can account for the previous experimental results of the low transparency of Y-TZP [2–5], since such fine grains are not attained. On the other hand, this model reveals the weak birefringent scattering in the infrared (IR) range as grain sizes less than 200 nm. This prediction is verified by the experimental results [2, 6]. Nanometric (115 nm) and dense tetragonal ZrO_2 was fabricated by Klimke et al. [2] using hot isotropic pressing (HIP). The 0.5 mm thickness specimen exhibited the maximum theoretical value of in-line transmittance (77%) in the IR region of 4-5 μm. The present authors [6] prepared nanograined (80 nm) and dense tetragonal zirconia using high-pressure spark plasma sintering (HP-SPS). In-line transmittance of a 1.5 mm thick sample approached 81–87% of the theoretical value in the wavelength of 3–5 μm. Meanwhile, tetragonal ZrO_2 showed the longest cutoff wavelength for high-strength transparent ceramics. These results highlight the great potential of this ceramic applied for durable infrared windows [2, 6].

It has been well established the beneficial effect of alumina dopant for sintering Y-TZP. The densification behavior and microstructural evolution during sintering of Y-TZP doped with alumina have been investigated by several researchers [7–13]. For example, Matsui et al. [7] found that the increase of alumina concentration could enhance the densification rate of Y-TZP, which was due to the improvement of apparent frequency-factor term in rate constant. Consequently, Y-TZP doped with alumina is highly expected as a superior raw material for fabricating transparent tetragonal zirconia.

This speculation was tested in the present study. Nanopowders of Y-TZP doped with alumina were used to prepare transparent tetragonal zirconia by high-pressure spark plasma sintering (HP-SPS). The effect of alumina dopant on transparency was analyzed with the comparison of that in pure Y-TZP nanopowders.

2. Experimental Procedure

2.1. Sample Preparation. The starting materials were commercial 3 mol% Y_2O_3 stabilized ZrO_2 powders with 0.3 mol% Al_2O_3 dopant (TZ-3Y-E, Tosoh Corporation, Tokyo, Japan) and 3 mol% Y_2O_3 doped ZrO_2 powders (TZ-3Y, Tosoh Corporation, Tokyo, Japan). These two commercial powders were consolidated directly using a spark plasma sintering machine (SPS-1050, SPS Syntex Inc., Kawasaki, Japan) in vacuum (10^{-3} Torr) to obtain dense bulk specimens. The applied pressure was 400 MPa [6] and the heating rate was 10°C/min. Sintering resulted in disk samples of 10 mm diameter and 1.3 mm thickness. The as-sintered samples were annealed at 900°C for 4 hours in air.

2.2. Optical Characterization. For measuring optical properties, both surfaces of the as-prepared disks were mirror-polished using diamond slurry. The total forward transmittance, in-line transmittance, and reflection were measured with a double-beam spectrophotometer (SolidSpec-3700DUV, Shimazu Co. Ltd., Kyoto, Japan) equipped with an integrating sphere. The distance between the sample and the detector was about 55 cm. For in-line transmittance measurements, a 3 mm pinhole was placed in front of the detector selecting only the in-line transmitted portion of the incident light (5 mm diameter). This setup allowed us to measure the "real in-line transmittance" [14].

The measured total forward transmittance (T) and in-line transmittance (I) could be expressed as the following formulas [15, 16]:

$$T = (1 - R)\exp(-\alpha t), \tag{1}$$

$$I = (1 - R)\exp[-(\alpha + \beta)t] = T\exp(-\beta t), \tag{2}$$

where R is the measured reflection, α is the absorption coefficient, t is the sample thickness, and β is the scattering coefficient. The absorption coefficient and scattering coefficient could be calculated from (1) and (2), respectively.

2.3. Microstructure Observation. For transmission electron microscope (TEM) observations, a 500 μm thick slab was cut by a low-speed diamond cutter, mechanically polished down to 100 μm, and further thinned with an Ar ion-milling machine. The TEM observations were performed using a JEOL-2010F microscope (JEOL Ltd., Akishima, Tokyo, Japan) operated at 200 kV. The grain size was measured by evaluating the average cross-sectional area per grain under the assumption of spherical grains. Because the samples had small pores and low porosity, grain boundary grooving caused by etching would distort the SEM images. Therefore, the porosity was measured by TEM, as an average value over five images.

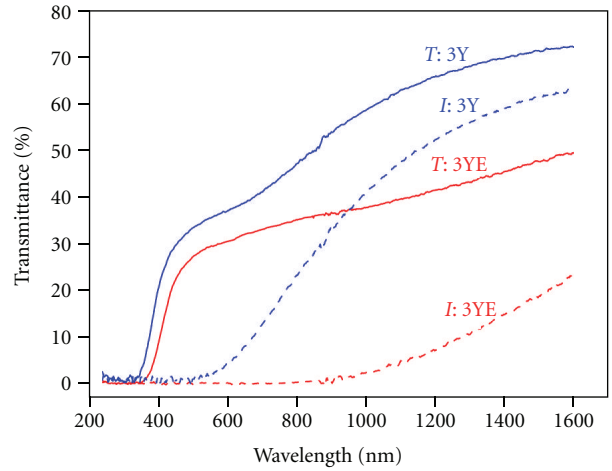

FIGURE 1: Typical total forward transmittance and in-line transmittance spectra of the yttria stabilized tetragonal zirconia without (3Y) and with alumina dopant (3YE). These two specimens were sintered for 10 min at 1050°C under the pressure of 400 MPa by means of SPS. The post-SPS annealing was conducted at 900°C for 4 hours in air. The samples analyzed in Figures 2 to 5 were fabricated at the same conditions. The thickness of these two samples was 1 mm.

3. Results and Discussion

It is possible to fabricate low translucent tetragonal zirconias using the TZ-3Y-E powders by means of high-pressure spark plasma sintering (HP-SPS) under the pressure of 400 MPa. The study of high pressure SPS of transparent TZ-3Y can be found elsewhere [6]. The optimum sintering temperature presents at 1050°C for TZ-3Y-E specimens fabricated at 1000 to 1200°C, thus we restrict our measurements and discussion to this sample in the following. The appearance of this sample is dark (not shown here). The dark appearance is usually attributed to color centers (oxygen vacancies with trapped electrons) [4–6, 16, 17], which are easily produced in zirconia under thermal reduction or electroreduction conditions [4–6, 16, 17]. The SPS process actually provides both conditions because high-temperatures vacuum and graphite dies yield thermal reduction, and electric current may result in electroreduction. We have observed the similar phenomenon in the study of transparent TZ-3Y [6]. After SPS processing, annealing is conducted at 900°C for 4 hours in air to reduce color centers of the TZ-3Y-E and TZ-3Y samples.

Figure 1 shows typical in-line transmittance and total forward transmittance spectra of TZ-3Y-E and TZ-3Y specimens. It can be observed that, in contrast to the expectation, the addition of alumina dopant actually results in worse optical properties of total forward transmittance and in-line transmittance. In addition, since the total forward transmittance contains the in-line transmittance and the

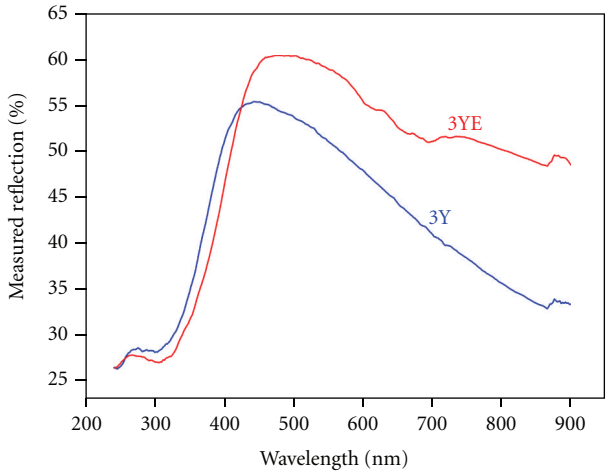

Figure 2: Dependence of the measured reflection of the yttria stabilized tetragonal zirconia without (3Y) and with alumina dopant (3YE). The thickness of these two samples was 1 mm.

forward scattering light, the increase of the total forward transmittance implies the existence of light scattering in the present samples. This scattering effect originates from residual pores and birefringence due to a tetragonal structure.

The dependence of light reflection on wavelength is represented in Figure 2. The reflection becomes more pronounced by the addition of alumina dopant. Here, the measured value consists of the intrinsic reflection losses at the front and back surfaces of the sample and back scattering from residual pores and birefringence. The intrinsic reflection should be independent of adding extremely low concentration of alumina dopant; therefore, only the increase of back scattering enhances the reflection of the TZ-3Y-E sample. It should be noted that grain boundary reflection, that is contribution from birefringence to back scattering, cannot be neglected in tetragonal zirconia because of its high birefringence. The maximum reflectivity $R_{\max}$ by m grain boundaries is given by [18]

$$R_{\max} \approx 1 - (1 - R_{\perp})^{m}, \tag{3}$$

where $R_{\perp}$ is the reflectivity for perpendicular incidence. $R_{\perp}$ can be calculated using

$$R_{\perp} = \frac{\Delta n^2}{(n_1 + n_2)^2}, \tag{4}$$

where n_1 and n_2 are the refractive indexes of two neighboring grains, and Δn is the refractive index difference [18]. For a 1 mm thick zirconia sample with grain size of 80 nm (see Figure 3), a light beam passes 1250 grain boundaries assuming that 10% grain boundaries are perpendicular to this beam. From (3), the reflectivity can be approximately estimated as 6% using $\Delta n = 0.03$, $n_1 = 2.16$, and $n_2 = 2.19$ [19]. Therefore, the contribution from the reflection at grain boundaries to back scattering of incident light cannot be omitted in tetragonal zirconia.

Figure 3 represents typical bright field TEM images for the microstructure of annealed TZ-3Y-E and TZ-3Y

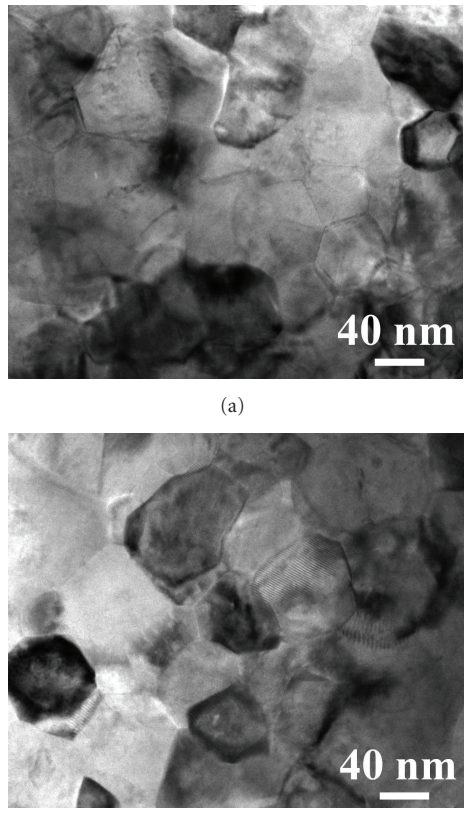

Figure 3: Bright-field TEM images of the yttria stabilized tetragonal zirconia without (a) and with alumina dopant (b).

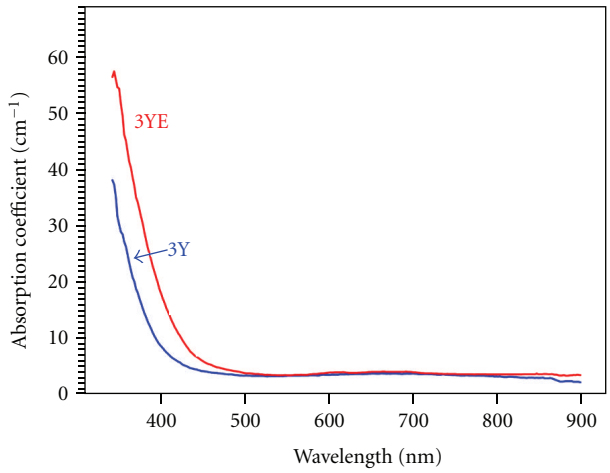

Figure 4: Absorption coefficients of the yttria stabilized tetragonal zirconia without (3Y) and with alumina dopant (3YE).

specimens. Fine intergranular pores are very rarely observed in TEM, indicating the extremely high density of the resultant specimens. It is hard to distinguish the difference of porosity between these two samples, and the porosity is estimated to be less than 0.05%. Meanwhile, similar mean grain size of about 80 nm is achieved for both specimens.

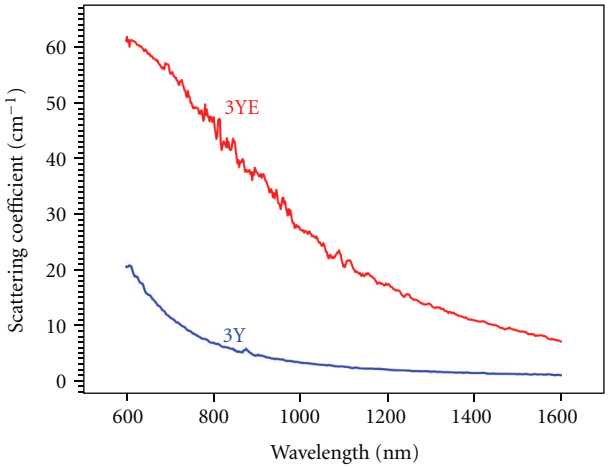

Figure 5: Scattering coefficients of the yttria stabilized tetragonal zirconia without (3Y) and with alumina dopant (3YE).

Figure 4 is the variation of the absorption coefficient on wavelength. It can be seen that the absorption coefficient of the TZ-3Y-E sample is slightly stronger than that of the TZ-3Y sample. This result indicates that more color centers are produced in the TZ-3Y-E sample. In fact, the dissolution of alumina dopant in zirconia promotes the production of color centers, and the defect reaction is written as the following [7]:

$$Al_2O_3 + 2Zr_{Zr}^{X} + O_O^{X} \xrightarrow{ZrO_2} 2Al'_{Zr} + V_O^{\bullet\bullet} + 2ZrO_2. \quad (5)$$

Meanwhile, alumina dopant just promotes the limited formation of color centers because of its low dissolution in zirconia [7]. Nevertheless, color centers cannot account for the low transmittance of the TZ-3Y-E sample because difference of absorption coefficients only occurs in short wavelength.

Figure 5 shows the dependence of the scattering coefficient on wavelength. Much higher scattering coefficient presented in the TZ-3Y-E sample obviously deteriorates the transparency. In the present zirconia samples, light scattering is induced by residual pores and birefringence. The similar porosity (Figure 3) implies that the difference in scattering coefficient only results from the different birefringence of these two samples. On the other hand, the similar grain size (Figure 3) cannot cause different birefringence of these two samples.

In fact, it is well known that most of alumina dopants distribute along grain boundaries of zirconia because of the very limited solubility, which has been clearly observed by Matsui et al. using STEM combined with nanoprobe electron dispersive X-ray spectroscopy [20]. This distribution results in the tremendous difference (0.43) of refractive index between alumina (1.76) and zirconia (2.19). Based on the theoretical calculation [2], only the difference of 0.09 in refractive index will lead to significant light scattering and seriously deteriorate the transparency of tetragonal zirconia. Therefore, we conclude that the strong birefringent scattering induced by the distribution of alumina dopant along grain boundaries causes the low transparency of the TZ-3Y-E sample.

4. Conclusions

The effect of alumina dopant on the transparency of tetragonal zirconia has been investigated in this work. Powders of 3% mol yttria stabilized tetragonal zirconia doped with alumina (TZ-3Y-E) are used as starting material to prepare transparent tetragonal ZrO_2 by high-pressure spark plasma sintering (HP-SPS). The result shows that the addition of alumina dopant deteriorates the transparency although nanometric grains and high density have been achieved in TZ-3Y-E samples. By comparing with the results of tetragonal zirconia without alumina dopant, the low transparency of the TZ-3Y-E samples is induced by the strong birefringent scattering, which is attributed to the distribution of alumina dopant along the grain boundaries of zirconia.

Acknowledgments

This work was partly supported by the Grant-in-Aid for Scientific Research (B-21360328 and C-22560674) from the Ministry of Education, Culture, Sports, Science and Technology, Japan, and by the Grant-in-Aid for Scientific Research on Priority Areas 474 from the JSPS and the Ministry of Education, Culture, Sports, Science and Technology (MEXT).

References

[1] J. Chevalier, L. Gremillard, A. V. Virkar, and D. R. Clarke, "The tetragonal-monoclinic transformation in zirconia: lessons learned and future trends," *Journal of the American Ceramic Society*, vol. 92, no. 9, pp. 1901–1920, 2009.

[2] J. Klimke, M. Trunec, and A. Krell, "Transparent tetragonal yttria-stabilized zirconia ceramics: influence of scattering caused by birefringence," *Journal of the American Ceramic Society*, vol. 94, no. 6, pp. 1850–1858, 2011.

[3] P. Duran, P. Recio, J. R. Jurado, C. Pascual, and C. Moure, "Preparation, sintering, and properties of translucent Er2O3-doped tetragonal zirconia," *Journal of the American Ceramic Society*, vol. 72, no. 11, pp. 2088–2093, 1989.

[4] S. R. Casolco, J. Xu, and J. E. Garay, "Transparent/translucent polycrystalline nanostructured yttria stabilized zirconia with varying colors," *Scripta Materialia*, vol. 58, no. 6, pp. 516–519, 2008.

[5] U. Anselmi-Tamburini, J. N. Woolman, and Z. A. Munir, "Transparent nanometric cubic and tetragonal zirconia obtained by high-pressure pulsed electric current sintering," *Advanced Functional Materials*, vol. 17, no. 16, pp. 3267–3273, 2007.

[6] H. B. Zhang, Z. P. Li, B. N. Kim et al., "Highly infrared transparent nanometric tetragonal zirconia prepared by high-pressure spark plasma sintering," *Journal of the American Ceramic Society*, vol. 94, no. 9, pp. 2739–2741, 2011.

[7] K. Matsui, T. Yamakawa, M. Uehara, N. Enomoto, and J. Hojo, "Mechanism of alumina-enhanced sintering of fine zirconia powder: influence of alumina concentration on the initial stage sintering," *Journal of the American Ceramic Society*, vol. 91, no. 6, pp. 1888–1897, 2008.

[8] Y. Sakka, T. Ishii, T. S. Suzuki, K. Morita, and K. Hiraga, "Fabrication of high-strain rate superplastic yttria-doped zirconia polycrystals by adding manganese and aluminum oxides," *Journal of the European Ceramic Society*, vol. 24, no. 2, pp. 449–453, 2004.

[9] X. Guo and R. Waser, "Electrical properties of the grain boundaries of oxygen ion conductors: acceptor-doped zirconia and ceria," *Progress in Materials Science*, vol. 151, no. 2, pp. 151–210, 2006.

[10] K. Matsui, N. Ohmichi, M. Ogai, H. Yoshida, and Y. Ikuhara, "Effect of alumina-doping on grain boundary segregation-induced phase transformation in yttria-stabilized tetragonal zirconia polycrystal," *Journal of Materials Research*, vol. 21, no. 9, pp. 2278–2289, 2006.

[11] H. Tsubakino, R. Nozato, and M. Hamamoto, "Effect of alumina addition on the tetragonal-to-monoclinic phase transformation in zirconia-3 mol% yttria," *Journal of the American Ceramic Society*, vol. 74, no. 2, pp. 440–443, 1991.

[12] S. N. B. Hodgson, J. Cawley, and M. Clubley, "Role of Al2O3 impurities on the microstructure and properties of Y-TZP," *Journal of Materials Processing Technology*, vol. 92-93, pp. 85–90, 1999.

[13] I. M. Ross, W. M. Rainforth, D. W. McComb, A. J. Scott, and R. Brydson, "The role of trace additions of alumina to yttria-tetragonal zirconia polycrystals (Y-TZP)," *Scripta Materialia*, vol. 45, no. 6, pp. 653–660, 2001.

[14] A. Krell, T. Hutzler, and J. Klimke, "Transmission physics and consequences for materials selection, manufacturing, and applications," *Journal of the European Ceramic Society*, vol. 29, no. 2, pp. 207–221, 2009.

[15] B. N. Kim, K. Hiraga, K. Morita, H. Yoshida, T. Miyazaki, and Y. Kagawa, "Microstructure and optical properties of transparent alumina," *Acta Materialia*, vol. 57, no. 5, pp. 1319–1326, 2009.

[16] H. B. Zhang, B. N. Kim, K. Morita, H. Yoshida, J. H. Lim, and K. Hiraga, "Optical properties and microstructure of nanocrystalline cubic zirconia prepared by high-pressure spark plasma sintering," *Journal of the American Ceramic Society*, vol. 94, no. 9, pp. 2981–2986, 2011.

[17] H. B. Zhang, B. N. Kim, K. Morita, H. Yoshida, J. H. Lim, and K. Hiraga, "Optimization of high-pressure sintering of transparent zirconia with nano-sized grains," *Journal of Alloys and Compounds*, vol. 508, no. 1, pp. 196–199, 2010.

[18] R. Apeta and M. P. B. van Bruggen, "Transparent alumina: a light-scattering model," *Journal of the American Ceramic Society*, vol. 83, no. 3, pp. 480–486, 2003.

[19] R. H. French, S. J. Glass, F. S. Ohuchi, Y. N. Xu, and W. Y. Ching, "Experimental and theoretical determination of the electronic structure and optical properties of three phases of ZrO2," *Physical Review B*, vol. 49, no. 8, pp. 5133–5142, 1994.

[20] K. Matsui, H. Yoshida, and Y. Ikuhara, "Phase-transformation and grain-growth kinetics in yttria-stabilized tetragonal zirconia polycrystal doped with a small amount of alumina," *Journal of the European Ceramic Society*, vol. 30, no. 7, pp. 1679–1690, 2010.

Hindawi Publishing Corporation
Journal of Nanomaterials
Volume 2012, Article ID 796815, 5 pages
doi:10.1155/2012/796815

Review Article

Growth of Thin Sheet Assembled Hierarchical ZnO Nanostructures

Boxiang Jia,[1] Weina Jia,[1] Jing Wang,[1] Fengyu Qu,[1] and Xiang Wu[1,2]

[1] *Key Laboratory for Photonic and Electronic Bandgap Materials, Ministry of Education and College of Chemistry and Chemical Engineering, Harbin Normal University, Harbin 150025, China*
[2] *Key Laboratory of Colloid and Interface Chemistry, Ministry of Education and Department of Chemistry, Shandong University, Jinan, Shandong 250100, China*

Correspondence should be addressed to Xiang Wu, wuxiang05@gmail.com

Received 21 November 2012; Accepted 4 December 2012

Academic Editor: Xijin Xu

Hierarchical ZnO nanostructures assembled from nanosheets are obtained through a facile hydrothermal route. The structure and morphology of the resultant products were characterized by X-ray diffraction (XRD), scanning electron microscope (SEM), and transmission electron microscope (TEM). The experimental results indicated that the as-synthesized ZnO nanosheets have an average thickness of approximately 50 nm. The possible mechanism for hierarchical ZnO nanostructures has been discussed in detail, and it was found that sulfur powder plays a critical role in the morphology of the products. Room temperature photoluminescence property of the hierarchical ZnO nanostructures shows an ultraviolet emission peak at 385 nm.

1. Introduction

In the past decades, enormous attention has been paid to synthesize semiconductor metal oxides due to their wide application potentials in gas sensors [1–4], photocatalysts [5–8], luminescent materials [9–12], and solar cells [13]. As one of the important semiconducting metal oxides, ZnO with a wide bandgap energy of 3.37 eV has been extensively studied and applied. In these applications, it is well-known that the performance is greatly influenced by the structure and morphology of ZnO materials.

Therefore, various morphologies of ZnO materials have been synthesized, including porous nanobelts [14], flower-like nanostructure [15, 16], nanotubes [17], nanowindmills [18], and hierarchical nanostructures [19–21]. However, hierarchical nanostructures have gained a great of research interest because they possess potential predominant performance. There are many reports about hierarchical ZnO nanostructures in the literature. Wang et al. prepared hollow ZnO hierarchical superstructures through a simple approach and investigated the optical properties of the ZnO superstructures [22]. Zhou's group synthesized hierarchically porous ZnO nanosheets from a hydrothermal approach [23]. Wang and his coworkers synthesized ZnO hierarchically porous structures with the assistance of glycine, Na_2SO_4, and polyvinyl pyrrolidone (PVP) [24]. But the above-mentioned methods need either complicated operation or the assistance of organic reagents.

In this work, we utilize a facile one-step hydrothermal route to synthesize hierarchical ZnO nanostructures without using any surfactants or templates. A possible growth mechanism of the as-prepared hierarchical ZnO products is proposed. Room temperature photoluminescence properties of the as-prepared ZnO products were investigated. The spectrum presents an ultraviolet emission peak at 385 nm, revealing an excellent optical quality.

2. Experimental Details

The chemical reagents used in our experiment are of analytical grade without any further purification. The experiment procedures are as follows: 5 mmol NaOH and 2.5 mmol $ZnSO_4$ were dissolved in 5 mL deionized water. A little sulfur powder was dispersed into the above mixture under stirring for 15 min at room temperature. Then the mixed solution was transferred into autoclave and kept at 120°C for 10 h.

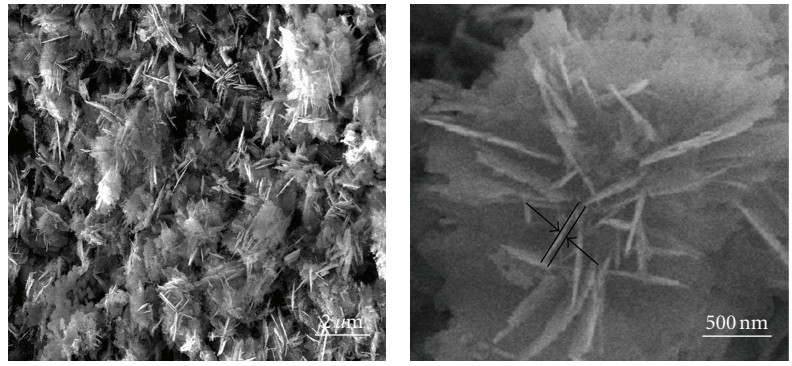

(a) (b)

Figure 1: SEM images of the as-synthesized products: (a) low magnification SEM image, (b) high magnification SEM image.

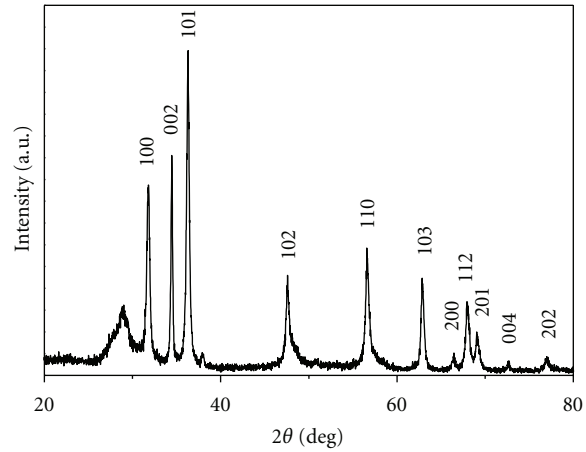

Figure 2: XRD pattern of the as-synthesized samples.

After the desired time, the autoclave was cooled naturally. The as-products were washed by deionized water several times and dried at 60°C for 5 h.

The phase of the as-obtained products was characterized using X-ray powder diffraction (XRD, Rigaku Dmax-rB, CuKα radiation, $\lambda = 0.1542$ nm, 40 KV, 100 mA). The morphology and microstructure of the samples were characterized by scanning electron microscope (SEM, Hitachi-4800), transmission electron microscope (TEM, JEOL-2010). Optical property of the as-synthesized hierarchical ZnO nanostructures was investigated by photoluminescence spectroscopy (PL SPEX FL-2T2).

3. Results and Discussion

Low-magnification SEM image (Figure 1(a)) presents the overall morphology of the as-synthesized samples, clearly observing that as-prepared samples consisted of many nanosheets. Further observation indicates that the thickness of nanosheets is approximately 50 nm as showed in Figure 1(b), indicating that numerous nanosheets assemble into the hierarchical nanostructures.

The phase and purity of the products were investigated by X-ray diffraction pattern. A representative XRD pattern of the product is shown in Figure 2. All diffraction peaks can be well indexed to the pure wurtzite (hexagonal) structured ZnO (space group $P6_3mc$) with lattice constants $a = 0.3250$ nm and $c = 0.5206$ nm, consistent with the standard values reported previously for bulk ZnO (JCPDS Card file no. 36-1451). No other impurity peaks are detected in the as-synthesized samples, revealing the high purity of the prepared ZnO nanostructures. The strong and sharp diffraction peaks imply that the samples have good crystallinity.

Further morphology and structure information about the hierarchical ZnO nanostructures was obtained from TEM images. Figure 3(a) shows a TEM image of the hierarchical ZnO nanostructures obtained by ultrasonic dispersion of the as-prepared ZnO sample in ethanol. It is apparent that the hierarchical ZnO nanostructures were shattered into ZnO nanosheets and the nanosheets were very thin. The selected area electron diffraction (SAED) pattern (Figure 3(b)) demonstrates that the hierarchical ZnO nanostructures are polycrystalline in nature and the diffraction rings are indexed to (100), (002), (101) planes of ZnO, respectively.

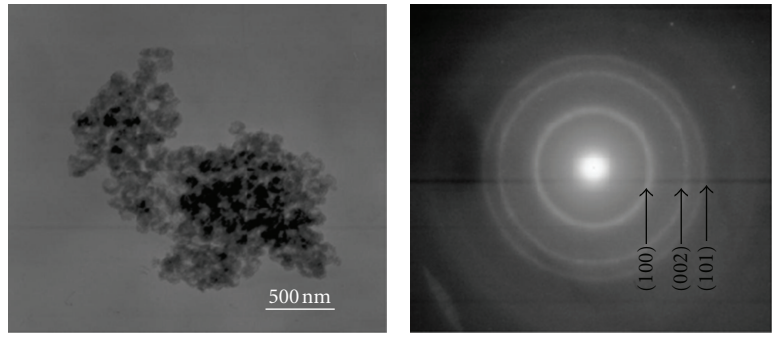

(a) (b)

Figure 3: (a) TEM images and (b) SAED pattern of the as-synthesized products.

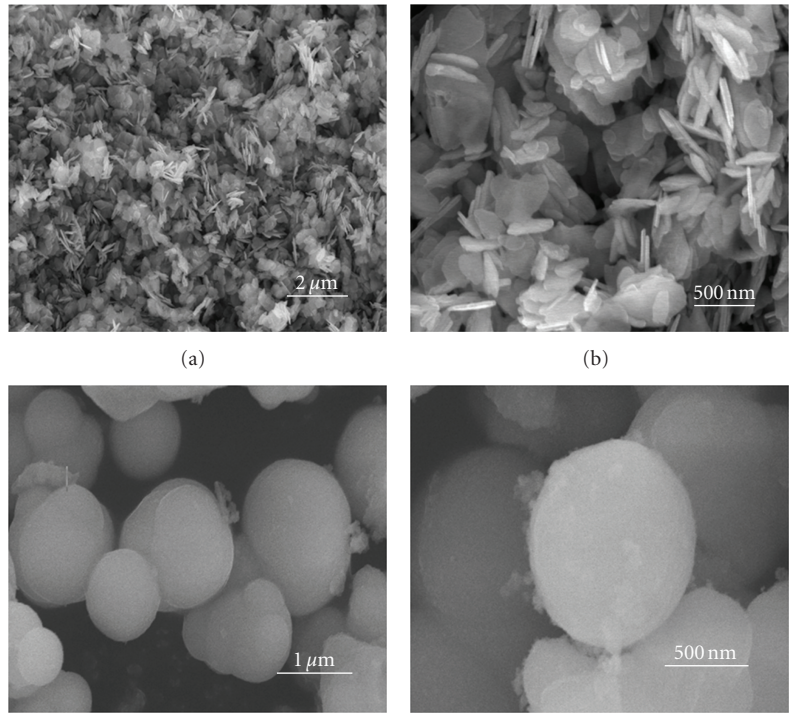

(a) (b)

(c) (d)

Figure 4: Growth control of the product morphology. SEM images of the products at different experiment parameters. (a-b) without the addition of sulfur powder, (c-d) the addition of ammonia water instead of sulfur powders.

To investigate effect of growth parameters on the morphology of hierarchical ZnO nanostructures, we conducted a series of comparison experiments. First, we performed the controlled experiment in the absence of sulfur powder, whereas the other experimental parameters were kept. Results showed that only the distribution of irregular thick ZnO nanosheets was obtained (see Figures 4(a) and 4(b)). Subsequently, we also investigated the effect of ammonia water on the morphology of the products. When 5 mL ammonia water instead of sulfur powder was added, hierarchical ZnO nanostructures did not be found (see Figures 4(c) and 4(d)), only plentiful of microspheres with a diameter of 1 μm were produced. The experimental results indicate that sulfur powder plays an important role in the final morphologies of the as-synthesized product.

Based on the above experimental results, a possible growth mechanism can be proposed as follows. At first, Zn^{2+} reacts with OH^- to form $Zn(OH)_2$, then $Zn(OH)_2$ can transform into ZnO nanosheets [25]. At the same time, sulfur powder induces ZnO nanosheets into self-assembly of hierarchical ZnO nanostructures. The overall reaction for the formation of hierarchical ZnO nanostructures may be simplified as follows:

$$\begin{aligned} Zn^{2+} + 2OH^- &\longrightarrow Zn(OH)_2 \\ Zn(OH)_2 &\longrightarrow ZnO + H_2O \end{aligned} \quad (1)$$

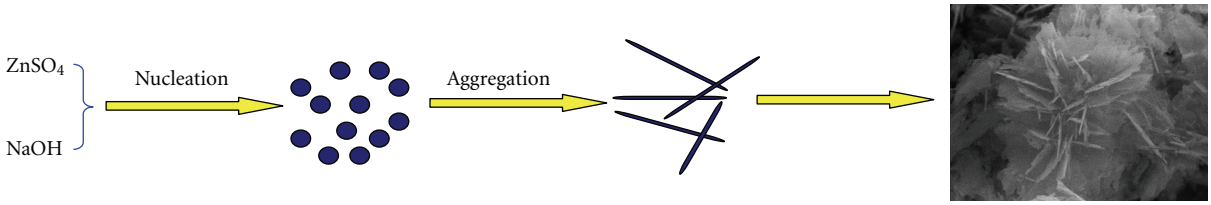

Figure 5: Schematic illustration of the possible growth mechanism of the as-synthesized hierarchical ZnO nanostructures.

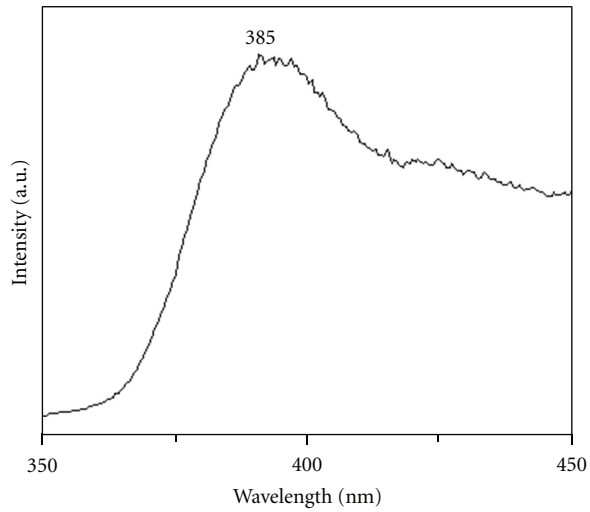

Figure 6: Room temperature photoluminescence spectrum of the as-synthesized hierarchical ZnO nanostructures.

Figure 5 shows the possible growth mechanism of the as-synthesized hierarchical ZnO nanostructures.

Finally, room-temperature photoluminescence property of the as-synthesized hierarchical ZnO nanostructures was investigated. The experiments were conducted by 325 nm He-Cd laser source. Figure 6 presents a PL spectrum of the as-synthesized hierarchical ZnO nanostructures. The spectrum reveals an emission band located at 385 nm, which can be commonly assigned as the near band gap exciton emission in ZnO [26, 27]. However, broad band with humps may be attributed to crystal disorder and the intrinsic defects such as oxygen vacancies, Zn interstitials, or impurities [28].

4. Conclusion

In summary, a simple hydrothermal route is developed for the fabrication of hierarchical ZnO nanostructures with the help of sulfur powder. The as-obtained hierarchical ZnO nanostructures are built up by nanosheets with the thickness of approximately 50 nm. The TEM result indicated that the as-synthesized products possess good crystallinity. Room temperature photoluminescence spectrum demonstrates that hierarchical ZnO nanostructures show a broaden UV band edge emission peak at 385 nm.

Acknowledgments

This work was sponsored by China Postdoctoral Foundation (2012M511016), Special Fund of Postdoctoral Innovation Projects in Shandong Province (201201007), Postdoctoral Initiation Foundation of Shandong University, and the Foundation for Key Project of Ministry of Education, China (no. 211046).

References

[1] F. Song, H. L. Su, J. Han, D. Zhang, and Z. X. Chen, "Fabrication and good ethanol sensing of biomorphic SnO_2 with architecture hierarchy of butterfly wings," *Nanotechnology*, vol. 20, no. 49, Article ID 495502, 2009.

[2] L. Ge, X. Jing, J. Wang et al., "Trisodium citrate assisted synthesis of ZnO hollow spheres via a facile precipitation route and their application as gas sensor," *Journal of Materials Chemistry*, vol. 21, no. 29, pp. 10750–10754, 2011.

[3] J. Zhang, S. Wang, Y. Wang et al., "ZnO hollow spheres: preparation, characterization, and gas sensing properties," *Sensors and Actuators B*, vol. 139, pp. 411–417, 2009.

[4] Z. Li, Q. Zhao, W. Fan, and J. Zhan, "Porous SnO_2 nanospheres as sensitive gas sensors for volatile organic compounds detection," *Nanoscale*, vol. 3, no. 4, pp. 1646–1652, 2011.

[5] L. L. Zhao, X. H. Ji, X. J. Sun, J. Li, W. S. Yang, and X. G. Peng, "Formation and stability of gold nanoflowers by the seeding

approach: the effect of intraparticle ripening," *The Journal of Physical Chemistry C*, vol. 113, pp. 16645–16651, 2009.

[6] B. X. Jia, W. N. Jia, Y. L. Ma, X. Wu, and F. Y. Qu, "SnO_2 core-shell microspheres with excellent photocatalytic properties ," *Science of Advanced Materials*, vol. 4, pp. 702–707, 2012.

[7] B. X. Jia, W. N. Jia, X. Wu, and F. Y. Qu, "Hierarchical porous SnO_2 microflowers photocatalyst," *Science of Advanced Materials*, vol. 4, pp. 1127–1233, 2012.

[8] Y. Han, X. Wu, Y. Ma, L. Gong, F. Qu, and H. Fan, "Porous SnO_2 nanowire bundles for photocatalyst and Li ion battery applications," *CrystEngCommunity*, vol. 13, no. 10, pp. 3506–3510, 2011.

[9] Y. H. Ni, S. Yang, J. M. Hong, L. Zhang, W. L. Wu, and Z. S. Yang, "Fabrication, characterization and properties of flowerlike ZnS-ZnO heterogeneous microstructures built up by ZnS-particle-strewn ZnO microrods," *The Journal of Physical Chemistry C*, vol. 112, no. 22, pp. 8200–8205, 2008.

[10] L. H. Gong, X. Wu, C. Ye, F. Y. Qu, and M. Z. An, "Aqueous phase approach to ZnO microspindles at low temperature," *Journal of Alloys and Compounds*, vol. 501, pp. 375–379, 2010.

[11] L. J. Yu, F. Y. Qu, and X. Wu, "Facile hydrothermal synthesis of novel ZnO nanocubes," *Journal of Alloys and Compounds*, vol. 504, pp. L1–L4, 2010.

[12] Z. Gu, M. P. Paranthaman, J. Xu, and Z. W. Pan, "Aligned ZnO nanorod arrays grown directly on zinc foils and zinc spheres by a low-temperature oxidization method," *ACS Nano*, vol. 3, no. 2, pp. 273–278, 2009.

[13] J. H. Qiu, M. Guo, and X. D. Wang, "Electrodeposition of hierarchical ZnO nanorod-nanosheet structures and their applications in dye-sensitized solar cells," *ACS Applied Materials & Interfaces*, vol. 3, pp. 2358–2367, 2011.

[14] X. Cao, N. Wang, L. Wang, and L. Guo, "Porous ZnO nanobelts: synthesis, mechanism, and morphological evolutions," *Journal of Nanoparticle Research*, vol. 12, no. 1, pp. 143–150, 2010.

[15] J. R. Huang, Y. J. Wu, C. P. Gu et al., "Preparation of porous flower-shaped SnO_2nanostructures and their gas-sensing property," *Sensors and Actuators B*, vol. 147, pp. 467–474, 2010.

[16] X. Y. Xue, Z. H. Chen, L. L. Xing, C. H. Ma, Y. J. Chen, and T. H. Wang, "Enhanced optical and sensing properties of one-step synthesized Pt−ZnO nanoflowers," *The Journal of Physical Chemistry C*, vol. 114, pp. 18607–18611, 2010.

[17] H. B. Chen, X. Wu, L. H. Gong, C. Ye, F. Y. Qu, and G. Z. Shen, "Hydrothermally-grown ZnO micro/nanotube arrays and their properties," *Nanoscale Research Letters*, vol. 5, pp. 570–575, 2010.

[18] L. J. Yu, F. Y. Qu, and X. Wu, "Solution synthesis and optimization of ZnO nanowindmills," *Applied Surface Science*, vol. 257, pp. 7432–7435, 2011.

[19] X. Wu, W. Cai, and F. Y. Qu, "Tailoring morphologies and wettability property of ZnO 1D nanostructures," *Acta Physica Sinica*, vol. 58, pp. 8044–8049, 2009.

[20] X. Y. Zeng, J. L. Yuan, and L. D. Zhang, "Synthesis and photoluminescent properties of rare earth doped ZnO hierarchical microspheres," *The Journal of Physical Chemistry C*, vol. 112, pp. 3503–3508, 2008.

[21] Y. Lei, F. Qu, and X. Wu, "Assembling ZnO nanorods into microflowers through a facile solution strategy: morphology control and cathodoluminescence properties," *Nano-Micro Letters*, vol. 4, no. 1, pp. 45–51, 2012.

[22] A. J. Wang, Q. C. Liao, J. J. Feng, P. P. Zhang, A. Q. Lia, and J. J. Wang, "Apple pectin-mediated green synthesis of hollow double-caged peanut-like ZnO hierarchical superstructures and photocatalytic applications," *CrystEngComm*, vol. 14, pp. 256–263.

[23] X. F. Zhou, Z. H. Hu, Y. Q. Fan, S. Chen, W. P. Ding, and N. P. Xu, "Microspheric organization of multilayered ZnO nanosheets with hierarchically porous structures," *The Journal of Physical Chemistry C*, vol. 112, pp. 11722–11728, 2008.

[24] X. Z. Wang, W. Liu, J. R. Liu et al., *ACS Applied Materials & Interfaces*, vol. 4, no. 2, pp. 817–825, 2012.

[25] Y. Lei, J. Wang, F. Y. Qu, H. Li, and X. Wu, "Facile approach to ZnO nanorods by directly etching zinc substrate," *Micro & Nano Letters*, vol. 5, pp. 485–488, 2011.

[26] M. D. Lourdes Ruiz Peralta, U. Pal, and R. Sanchez Zeferino, "Photoluminescence (PL) quenching and enhanced photocatalytic activity of Au-decorated ZnO nanorods fabricated through microwave-assisted chemical synthesis," *ACS Applied Materials & Interfaces*, vol. 4, pp. 4807–4816, 2012.

[27] J. Song, J. Zhou, W. Wang et al., "Growth mechanism and photoluminescent properties of AlN/ZnO heterostructures," *Journal of Physical Chemistry C*, vol. 114, no. 24, pp. 10761–10767, 2010.

[28] U. Pal, C. W. Kim, N. A. Jadhav, and Y. S. Kang, "Ultrasound-assisted synthesis of mesoporous ZnO nanostructures of different porosities," *Journal of Physical Chemistry C*, vol. 113, no. 33, pp. 14676–14680, 2009.

Hindawi Publishing Corporation
Journal of Nanomaterials
Volume 2012, Article ID 938495, 5 pages
doi:10.1155/2012/938495

Research Article

Simple Method for Surface Selective Adsorption of Semiconductor Nanocrystals with Nanometric Resolution

O. Koslovsky,[1] S. Yochelis,[1] N. Livneh,[1] M. G. Harats,[2] R. Rapaport,[1,2] and Y. Paltiel[1]

[1] *Applied Physics Department and Center for Nanoscience and Nanotechnology, Hebrew University of Jerusalem, 91904 Jerusalem, Israel*
[2] *Racah Institute of Physics, Hebrew University of Jerusalem, 91904 Jerusalem, Israel*

Correspondence should be addressed to O. Koslovsky, okjerusalem@gmail.com

Received 14 October 2012; Accepted 26 November 2012

Academic Editor: Chuanfei Guo

Self-assembly methods play a major role in many modern fabrication techniques for various nanotechnology applications. In this paper we demonstrate two alternatives for self-assembled patterning within the nanoscale resolution of optically active semiconductor nanocrystals. The first is substrate selective and uses any high resolution surface patterning to achieve localized self-assembly. The second method uses a surface with poly(methyl methacrylate) (PMMA) resist patterning adsorption of the nanocrystal with covalent bonds and liftoff.

1. Introduction

In recent years a major progress was achieved in fabrication and characterization techniques, down to nanometer scale resolution. This approach brings many opportunities and may open a way for developing new quantum engineered features as well as other important aspects. For example, in transport base devices, dense nanometric packaging of electrical devices increases the speed of operation, enhances the capacitance of a single chip, and reduces heating.

One promising approach is the use of self-assembled organic molecules as the major building blocks of these devices [1–3]. These devices usually relay on an assembly of 2D organic monolayers [4, 5]. The combination of self-assembled organic molecules and semiconducting nanocrystals (NCs) is frequently employed as building blocks of such nanoscale electronics devices [6]. Optoelectronic properties of NCs can be controlled by their size, shape, composition, and doping which makes them attractive components in nanoelectronics devices [7]. In all these devices the distance between subsequent layers is nanometric, and the layers are self-ordered perpendicular to the substrate. However, the arrangement of the self-assembled layers in a controlled way is not fully developed yet and new methods that will help selective nanometric patterning are needed. Large efforts have been directed to achieve selective processes and several techniques were developed to answer the demand. In general the leading techniques can be divided into several classes: self-organization, nanoprinting, nanostamping, and photolithography patterning.

An example of nano printing is using surface patterning by microcontact chemistry, [8, 9] when a reactive "ink" molecule from a microstructured, elastomeric stamp is transferred onto surfaces modified with complementary reactive groups, leading to a chemical reaction in the area of contact. This process usually leads to micron-size resolution. By using solvent free microcontact printing with molded poly(dimethylsiloxane) (PDMS) as a nanostructure stamp template, Lee et al. showed deposition of patterned and unpatterned colloidal quantum dot thin films as the electroluminescent layers within hybrid organic-QD light-emitting devices. The result was a nanometric pattern of nanocrystal on a substrate. Self-organized systems can be based on templates of block copolymer films and include the fabrication of two-dimensionally organized nanoparticle assemblies on the patterning films as a simple and straight forward assembly mechanism [10]. The resolution in this case is nanometric but hard to control.

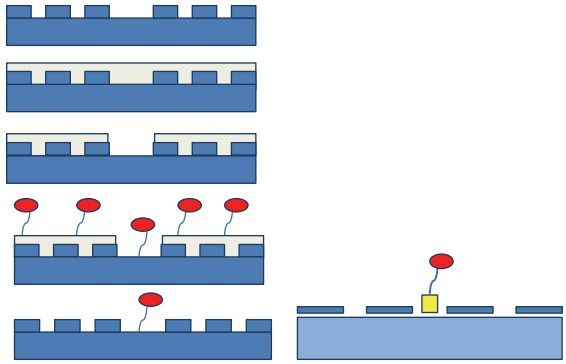

Figure 1: (a) Illustration of the selective adsorption process using resist and e-beam lithography to open a hole for molecules adsorption on a patterned metallic structure. (b) Illustration of selectively adsorbed nanoparticles by chemical specific recognition to gold surface.

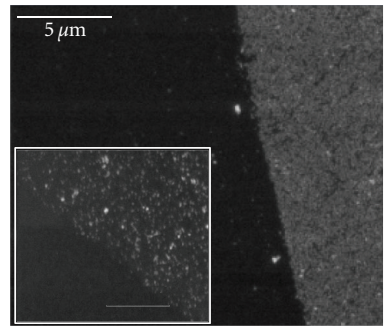

Figure 2: InAs/CdSe/ZnSe nanoparticles on top of a GaAs substrate. The sharp boarder is determined by the resolution of the e-beam lithography. The nanocrystals are chemically adsorbed to the surface using covalent bonds and therefore stay on the substrate after washing the sample in acetone and toluene. The inset shows the edge line at higher resolution.

New developed methods to the nano scale fabrication are based on the recently well-established lithography techniques. A significant work by Palma et al. demonstrated a selective self-assembly of biomolecules on nanopatterned surfaces together with minimizing nonspecific adsorption [11]. Another example is a study describing oleate-capped PbSe nanocrystals that were found to adhere preferentially to H-terminated Si surfaces over oxide and alkyl-terminated Si surfaces [12]. Scanning probe lithography was used to oxidize locally a dodecyl monolayer on the Si surface. Aqueous HF was then used to remove the oxide and expose H-terminated Si areas. After exposure to a nanocrystals solution, local patterns of PbSe nanocrystals are created on the Si surface. The last patterning technique gives the highest resolution of selective adsorption; however, it requires the use of slow and expensive scanning probe microscopy writing and therefore is hard to adjust for industrial day to day use. Our approach uses two different methods to selectively adsorb nanocrystals with organic molecules. In both cases the patterned monolayers of the nanocrystals are realized using simple self-assembly methods. The high resolution surface patterning can be achieved on different substrate types due to molecules self-assembly. In our case we are utilizing e-beam lithography or evaporation method to prenanopattern the desired adsorbed area; however, any prepatterning options can be used to achieve selectivity based on the presented methods.

2. Materials and Methods

In the first method we cover a surface with poly(methyl methacrylate) (PMMA) 950 A2 resist. Using e-beam lithography we achieve nanometric resolution patterning as illustrated in Figure 1(a) for a patterned center of a round metallic lens surface. Next, self-assembly of organic molecules followed by nanoparticles adsorption is performed over the whole surface. With the removing of the resist the remaining nanocrystals are located only within the desired pattern (see illustration in Figure 1(a)). The covalent bonds holding the nanocrystals are strong enough to be compatible with repeatable process and therefore can be used to pattern layers.

In the second method we present a selective chemical recognition of different surfaces type by specific organic molecules groups. When evaporating gold nanopattern (5 nm of Ti then 20 nm Au) onto oxidized surfaces the formed surfaces are chemically distinct. The adsorption of specific molecules like dithiol moieties takes place only onto the gold surfaces; therefore readsorption of nanoparticles to the tail end of the molecule results in specific regions with nanoparticles (see the illustration in Figure 1(b)).

The PMMA is usually patterned on a GaAs substrate. The substrate is washed with acetone and iso-propanol before oxygen-plasma asher cleaning. Then a PMMA is spin coated (5000 rpm for 45 sec) on the cleaned substrate to have approximately 60 nm thick layer followed by prebaking at 180°C for 2 min (reflectometer measurement shows thickness of 78 nm). The desired pattern is achieved by opening lines in the PMMA with e-beam lithography. The sample is then developed in 5°C methyl isobutyl ketone (MIBK): IPA for 120 sec. The PMMA liftoff after NCs adsorption is performed in a hot acetone for 2 min then sonicated in heated acetone for 1 min and finally washed with isopropanol (IPA) and dried with N_2.

Both of the above procedures use self-assembly organization on the Au, GaAs, or Si substrates. All the substrates are rinsed with acetone then ethanol and treated with 50% plasma asher power (Diener PICO UHP 40 kHz/200 W) for 10 min, prior to molecule adsorption. When using GaAs the substrate is also etched with 2% HF for 5 sec followed by 25% NH_3OH for 30 sec prior to the molecule self-assembly. It is then incubated in ethanol solution for 20 minutes, followed by incubation in 1 mM 1,9-nonanedithiol in anhydrous ethanol solution overnight and finally the substrate is dipped in InAs/CdSe/ZnSe nanocrystals suspended in Toluene for 4 hours. The sample is then washed in Toluene for several times.

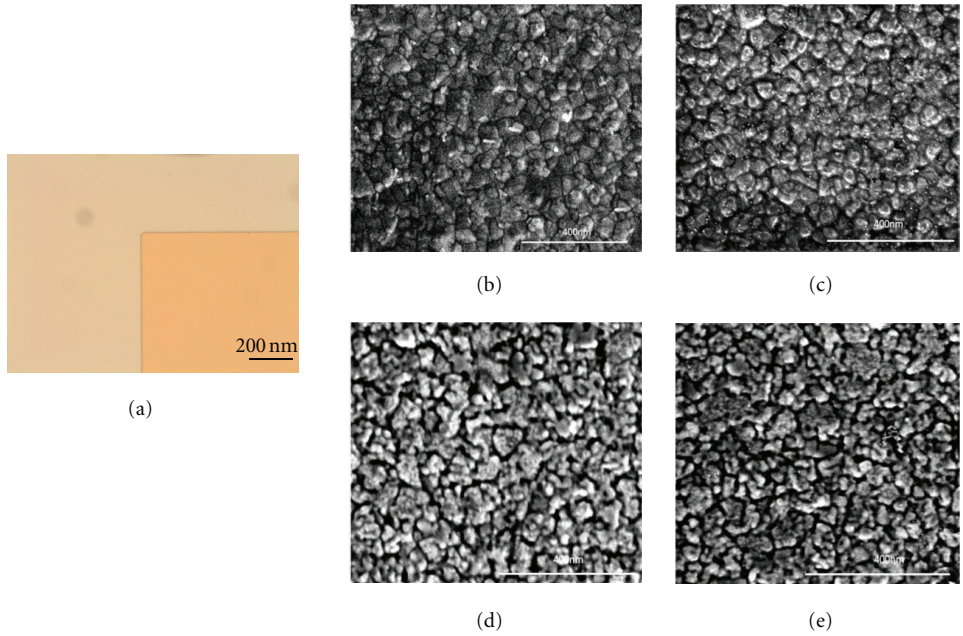

Figure 3: Specific adsorption demonstrated on an array of gold squares on an aluminum surface. The sample is shown in (a). The smaller square is the gold surface and at the background is the aluminum substrate. In (b and d) the gold and aluminum substrates, respectively, are shown with molecules adsorption only. In (b) It is possible to observe the gold grains but the surface is clean from NCs. (c) shows the gold area of the sample after dipping the sample in the NCs solution. The surface is covered with NCs at a density of about 7×10^{10} NCs/cm^2. By comparing these results to the adsorption of NCs on the Al_2O_3 surface (d) with molecules only and (e) after dipping in NCs solution, we can see the selectivity.

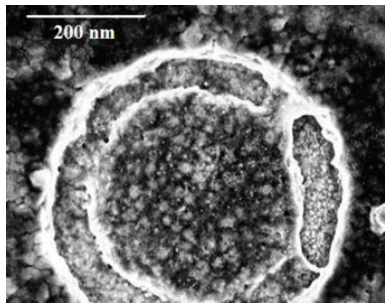

Figure 4: High resolution SEM images of aluminum and gold lens structure. Nanometric resolution of specific adsorption is demonstrated on the 300 nm diameter gold surface in the center of the aluminum sample. The gold center part is brighter than the aluminum part. NCs are seen only on the gold.

The InAs/CdSe/ZnSe nanocrystals (from Prof. Uri Banin's group) were synthesized in tri-octyl phosphine using $InCl_3$ and TMS_3As as precursors according to the procedure described elsewhere [13] and underwent subsequently a size-selection process. For the purposes of the experiment we have used InAs NCs 6.5 nm in diameter. For the shell growth an ionic layer adsorption and reaction process has been used. The shell consisted of 1 monolayer (ML) of CdSe, followed by 4 MLs of ZnSe. As a result, the emission efficiency from the NCs at 0.96 eV has increased by more than 2 orders of magnitude.

3. Main Results

Specific adsorption using PMMA resist patterning on a GaAs substrate is presented in Figure 2. In this figure a clear line is seen between the area of dense InAs/CdSe/ZnSe NCs adsorption (10^{12} NCs/cm^2) on the right where the resist was developed and the places where the liftoff occurred. This high selectivity line is presented at larger scale at the inset.

In this method the adsorption is performed all over the sample and after removing the resist, in our case a PMMA, the desired nanocrystal pattern emerges. It is then possible to have very high resolution patterns depending on the e-beam lithography resolution limits. This procedure is not limited to the surface type and also it is possible to repeat the process several times on the same sample in order to get multilayers.

Another option we present to selectively pattern self-assembled layers is demonstrated by molecular specific chemical recognition. We show before a clear border between nanoparticles adsorbed on one surface and a different surface that shows no adsorption. In Figure 3(a) we show an array of gold squares on an aluminum surface. The figure presents a selective adsorption of InAs/CdSe/ZnSe nanocrystals to the gold parts of the sample. The selectivity here occurs due to a specific chemical recognition between thiol (SH) head group to a gold surface but not to the oxide surfaces of the sample. In Figures 3(b), 3(c), 3(d), and 3(e) the specific adsorption is demonstrated. Here again a thiol group was adsorbed to a gold surface but not to aluminum. In this process, in order to prevent NCs to physically adsorb to the aluminum surface,

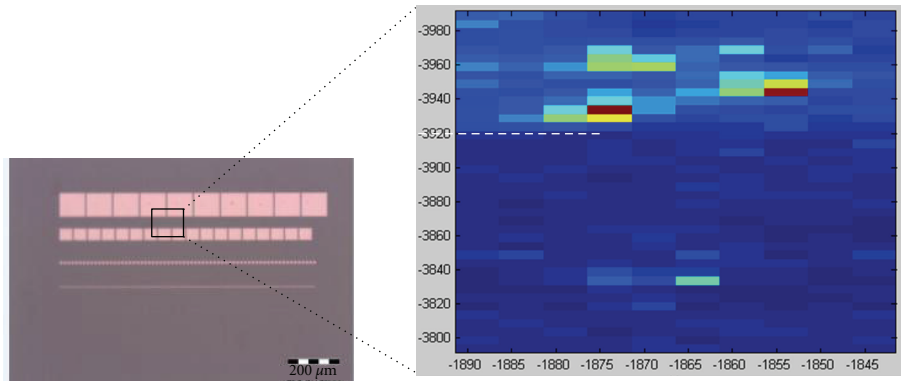

(a) (b)

Figure 5: On the left, the patterned gold on Si sample, on the right optical mapping of the emission from the NCs. The dashed line shows the gold (top)/Si (bottom) border.

we adsorbed also octadecyl trichlorosilane (OTS) molecules that attach to the aluminum surface. This monolayer does not have a tail group to bind to the NCs. Figure 3(b) represents gold substrate with 1,9-nonane dithiol molecules adsorbed only. It is possible to observe the gold grains but the surface is clean from NCs. On the contrary, in Figure 3(c) we show the same sample after dipping it in the NCs solution where we observe the surface which is covered with NCs. The NCs density on the surface is about 7×10^{10} NCs/cm^2. Comparing these results to the adsorption of NCs on the Al_2O_3 surface in Figures 3(d) and 3(e) it is possible to see that the surface is almost clean from NCs also after dipping (Figure 3(e)) in the NCs solution. XPS measurements on the gold and aluminum surfaces confirmed the selectivity of the adsorption: on the gold surface the signal from the NCs was much higher. The presented chemical specific recognition of molecules to a certain surface together with photoresist patterning opens the opportunity of creating complicated nanoresolution patterns.

To realize selective adsorption to structures with nanometric resolution, we prepared a 300 nm diameter gold surface in the center of concentric aluminum ring. This is important, for example, for applications where the emission of photons from the NCs should be directional [14–16]. In this case it is important to adsorb the NCs at the center of the lens only. By fabricating a nanometric gold surface at the center of the lens one can use selective adsorption to guarantee that the NCs will be located at the center of the lens only. Figure 4(a) is showing high resolution SEM images of the concentric gold circle surrounded by such an aluminum circle. The NCs are adsorbed only onto the gold area and not on the surrounding aluminum part.

Finally in order to check that the NCs adsorb to gold selectively, with organic linkers that are long enough to decrease the nonradiative coupling to the metal substrate and prevent significant optical quenching, we have performed spatially resolved optical measurements with a high resolution confocal detection setup. The InAs/CdSe/ZnSe NCs were excited by a 780 nm laser and their emission was around 1200 nm. The dots were highly concentrated on the gold part with density higher than 10^{11} dot/cm^2. We have achieved the same selectivity using both micrometric and nanometric patterns. Down to the 100 nm size the selectivity is not size dependent, and therefore the same procedure can be used with any high resolution nanopatterning. Figure 5(b) displays optical mapping of the NCs emission of the sample that is presented in Figure 5(a). The dashed white line presents the gold/Si border. The top part of the sample map is the gold substrate where a clear emission from the NCs is observed, while on bottom of the Si part almost no NCs are recognized. The exact patterning border seems to be smaller than 40 nm and is related to our fabrication quality.

4. Summary

In summary we demonstrate self-assembled patterning with nanoscale resolution using two methods: e-beam lithography and selective chemical recognition of surfaces. The pre-nanopatterning employs e-beam lithography or evaporation in our case; however, any prepatterning process could be used in order to achieve the needed selectivity. The high resolution patterning achieved utilizing both known methods as e-beam lithography and evaporation, and self-assembly of organic molecules. The processes are simple and compatible with many substrates. Moreover, it is possible to repeat the processes several times to achieve multilayers on the selected surfaces.

References

[1] N. J. Tao, "Electron transport in molecular junctions," *Nature Nanotechnology*, vol. 1, no. 3, pp. 173–181, 2006.

[2] P. E. Burrows, S. R. Forrest, and M. E. Thompson, "Prospects and applications for organic light-emitting devices," *Current Opinion in Solid State and Materials Science*, vol. 2, no. 2, pp. 236–243, 1997.

[3] H. E. Katz and Z. Bao, "The physical chemistry of organic field-effect transistors," *Journal of Physical Chemistry B*, vol. 104, no. 4, pp. 671–678, 2000.

[4] H. B. Akkerman, P. W. M. Blom, D. M. De Leeuw, and B. De Boer, "Towards molecular electronics with large-area molecular junctions," *Nature*, vol. 441, no. 1, pp. 69–72, 2006.

[5] O. Seitz, A. Vilan, H. Cohen et al., "Doping molecular monolayers: effects on electrical transport through alkyl chains on silicon," *Advanced Functional Materials*, vol. 18, no. 14, pp. 2102–2113, 2008.

[6] Y. Paltiel, A. Aharoni, U. Banin, O. Neuman, and R. Naaman, "Self-assembling of InAs nanocrystals on GaAs: the effect of electronic coupling and embedded gold nanoparticles on the photoluminescence," *Applied Physics Letters*, vol. 89, no. 3, Article ID 033108, 3 pages, 2006.

[7] X. Peng, L. Manna, W. Yang et al., "Shape control of CdSe nanocrystals," *Nature*, vol. 404, no. 6773, pp. 59–61, 2000.

[8] C. Wendeln and B. J. Ravoo, "Surface patterning by microcontact chemistry," *Langmuir*, vol. 28, no. 13, pp. 5527–5538, 2012.

[9] A. Lee, P. O. Anikeeva, S. A. Coe-Sullivan, J. S. Steckel, M. G. Bawendi, and V. Bulović, "Contact printing of quantum dot light-emitting devices," *Nano Letters*, vol. 8, no. 12, pp. 4513–4517, 2008.

[10] M. J. Pavan and R. Shenhar, "Two-dimensional nanoparticle organization using block copolymer thin films as templates," *Journal of Materials Chemistry*, vol. 21, no. 7, pp. 2028–2040, 2011.

[11] M. Palma, J. J. Abramson, A. A. Gorodetsky et al., "Selective biomolecular nanoarrays for parallel single-molecule investigations," *Journal of the American Chemical Society*, vol. 133, no. 20, pp. 7656–7659, 2011.

[12] G. P.-A. Andras, H. Qiao, J. Shan et al., "Site-selective optical coupling of pbse nanocrystals to si-based photonic crystal microcavities," *Nano Letters*, vol. 9, no. 8, pp. 2849–2854, 2009.

[13] A. A. Guzelian, U. Banin, A. V. Kadavanich, X. Peng, and A. P. Alivisatos, "Colloidal chemical synthesis and characterization of InAs nanocrystal quantum dots," *Applied Physics Letters*, vol. 69, no. 10, pp. 1432–1434, 1996.

[14] H. J. Lezec, A. Degiron, E. Devaux et al., "Beaming light from a subwavelength aperture," *Science*, vol. 297, no. 5582, pp. 820–822, 2002.

[15] A. G. Curto, G. Volpe, T. H. Taminiau, M. P. Kreuzer, R. Quidant, and N. F. Van Hulst, "Unidirectional emission of a quantum dot coupled to a nanoantenna," *Science*, vol. 329, no. 5994, pp. 930–933, 2010.

[16] N. Livneh, A. Strauss, I. Schwarz et al., "Highly directional emission and photon beaming from nanocrystal quantum dots embedded in metallic nanoslit arrays," *Nano Letters*, vol. 11, no. 4, pp. 1630–1635, 2011.